Fall 2021

Fabrication and Characterization of Micro/Nanostructured Ceramic Device for Energy Conversion

Yun Gan

FABRICATION AND CHARACTERIZATION OF MICRO/NANOSTRUCTURED CERAMIC DEVICE FOR ENERGY CONVERSION

by

Yun Gan

Bachelor of Engineering
Hefei University of Technology, 2012

Submitted in Partial Fulfillment of the Requirements

For the Degree of Doctor of Philosophy in

Mechanical Engineering

College of Engineering and Computing

University of South Carolina

2021

Accepted by:

Xingjian Xue, Major Professor

Jamil A. khan, Committee Member

Guiren Wang, Committee Member

Hui Wang, Committee Member

Tracey L. Weldon, Interim Vice Provost and Dean of the Graduate School

ACKNOWLEDGEMENTS

I would like to express my deepest appreciation to my advisor Dr. Xingjian Xue. His invaluable insight and meticulous attitude towards research highly affect me in my academic career. The completion of my dissertation cannot be done without his extraordinary guidance and tremendous help. It has been a great pleasure working with Dr. Xue over the past six years.

I am extremely grateful to Dr. Jamil A. Khan, Dr. Guiren Wang and Dr. Hui Wang for serving as my committee members. I very much appreciate the valuable advice.

My sincere thanks also go to my group members, Dr. Chunlei Ren, Dr. Chunyang Yang and Myongjin Lee. Whenever I encounter difficulties in my research, they are always there helping me and providing me with inspiring suggestions.

I would like to express my special thanks to my parents and my parents in law. They have provided me endless support and encouragement throughout this entire process. I'm deeply indebted to my wife and my daughter who give me unconditional love and accompany me with happiness and confidence during this long journey.

ABSTRACT

The deteriorating climate is threatening our living habitat and arousing public awareness. To achieve the carbon neutral goal by the middle of 21st century, developing novel technologies to reduce CO_2 emission or promote its capture become urgent. Among them, oxygen permeation membrane (OPM) and solid oxide cell (SOC) are two promising devices for clean energy conversion.

In chapter 1, the background of OPM and SOC are briefly introduced. Fundamental mechanism and application of phase inversion, the key process involved in fabrication of hollow fiber OPM and microtubular SOC are emphatically described. Mixed ionic and electronic conducting (MIEC) perovskites demonstrate advantages over Ni-cermet as fuel electrode for SOCs. However, SOCs are primarily electrolyte-supported planar designs in literature when MIEC perovskite fuel electrodes are employed, which are relatively easy to fabricate but usually have high electrolyte ohmic resistance. Perovskite fuel electrode-supported designs are rarely studied particularly for microtubular SOCs. In Chapter 2, $(La_{0.3}Sr_{0.7})_{0.9}Ti_{0.9}Ni_{0.1}O_{3-\delta}$-$Sm_{0.2}Ce_{0.8}O_{1.9}$ (LSTN-SDC) electrode-supported microtubular cell LSTN-SDC/YSZ/$(La_{0.8}Sr_{0.2})_{0.95}MnO_{3-\delta}$ (LSM) is fabricated and characterized. The LSTN-SDC microtubular substrate is prepared using an spinneret spinning in combination with modified phase inversion method, featuring radially well-aligned microchannels open at the inner surface. A thin YSZ electrolyte and LSM electrode are then fabricated on the substrate. Upon reducing treatment, nickel nanoparticles are exsolved from LSTN grains and uniformly decorated onto grain surface. With CO/CO_2 gas mixture as the fuel, the

complicated electro-/chemical reactions are identified in the substrate electrode. The electrolysis process combines with surface catalytic process of nanostructured electrode substrate leads to highly efficient CO production with conversion efficiencies above 100%. The electrolysis also facilitates to regenerate surface catalytic functionality of electrode substrate. The redox stability advantages of the cell are demonstrated in both alternative reduction (CO)/oxidation (air) atmospheric conditions and reversible operating mode.

Due to high surface area to volume ratio, hollow fiber membranes have been extensively investigated for oxygen separation applications. The widely studied hollow fiber membranes are fabricated using spinneret process in combination with phase inversion method, followed by one-step high temperature sintering. The resultant membrane demonstrates multiple layers, where a relatively thick sponge-like layer is sandwiched by the radially aligned closed finger-liked pore layers on either side, and the shell and lumen sides are covered by relatively dense thin skin layers. To take advantage of finger-like pores for facile gas diffusion, hollow fibers with open finger-like pores are created using spinneret process with modified phase inversion method, built upon which thin film dense separation layer and porous catalyst layer are fabricated to form an asymmetric membrane. The asymmetric design can reduce sintering temperature for membrane fabrication and enhance conductivity for bulk charge transport. However, the mechanical strength of the hollow fiber membranes is usually not sufficient and high-cost material is used for the substrate. In Chapter 3, LSCF-ZnO composite hollow fiber is developed and optimized so that radially-aligned open microchannels are produced. Built upon the composite hollow fiber, thin film dense LSCF separation layer and porous LSCF catalyst layer are successfully fabricated. The performance and long-term stability of the

membrane are systematically measured and characterized. Results indicate that ZnO addition to the hollow fiber substrate can not only decrease the sintering temperature for membrane fabrication but also significantly enhance the mechanical strength, robustness, durability, and stability. By replacing a considerable amount of high cost LSCF with low cost ZnO in the substrate, the capital cost of the membrane can also be significantly reduced.

Surface oxygen exchange is a critical reaction step for energy conversion and storage in OPM and SOC. Oxygen reduction reaction (ORR) and oxygen evolution reaction (OER) are typical operating modes of surface exchange process. To enhance ORR/OER properties, nanostructures are introduced into surface porous layer/electrode. Due to high operating temperatures, the synthesis routes for nanostructured devices at low temperatures are rarely suitable, and infiltration could be the only widely used technique. Recently, hydrothermal synthesis route was employed. Nevertheless, the ORR/OER mechanisms associated with such a surface is not clear and the stability is still a concern. In Chapter4, built upon oxygen separation membrane and symmetric cells, Co_3O_4 nanocluster-structured surfaces are directly fabricated using hydrothermal route. Electrochemical tests are conducted using the membrane and symmetric cells with two-electrode and three-electrode configurations. The ORR/OER surface exchange mechanisms are analyzed, and the effects of nanostructured surface are identified. A short-term stability (~ 100 h) is also conducted using a symmetric cell at 900 °C. While a slight degradation occurs over the course, both performance and surface microstructures are stabilized after a certain time of the stability test. This dissertation contributes to the fabrication and characterization of micro/nano-structured OPM and SOCs with decent stability.

TABLE OF CONTENTS

LIST OF FIGURES

CHAPTER 1

INTRODUCTION

1.1 Background Introduction

With blooming of science and economy in the last two decades, the energy demand of human is also increasing perpetually. Consequently, this led to a growing consumption of fossil fuels and has caused a serious environmental issue-global warming.[1] The large amount of greenhouse gases, CO_2 in particular, emitted from the combustion of coals and petroleum contributes to this climate change. And it is reported that the global atmospheric CO_2 concentration has already increased by 19%, which is only about 315 ppm in 1958 while rise to 375 ppm at the end of 2005. What's worse, the hydrocarbon resources will still supply more than 60% of the world's energy requirements over the next 20 years.[2] The deteriorating climate has threatened our living habitat and aroused the public awareness. Policies are proposed across international countries to reduce the emission of greenhouse gases, such as Kyoto protocol and the Paris Agreement.[3] Moreover, lots of investments and researches have been performed in developing novel technologies to promote CO_2 capture as well as reducing its emission. Two potential technologies are described below briefly.

1.1.1 Oxygen Permeation Membrane

Oxyfuel technology, which burn the hydrocarbon fuels in a CO_2/O_2 mixer, has been widely used in power plants due to its easy CO_2 recovery, low NO_x emissions and high

desulfurization efficiency.[4] There are various oxyfuel cycle concepts including the Advanced zero-emission power plant (AZEP); Graz and water cycle; MATIANT and Feher supercritical CO_2 cycles; the zero-emission power plant and the zero-emissions ITM oxyfuel plant etc.[5] In all the above process, pure oxygen is used for fuel combustion instead of conventional air. Therefore, nitrogen is avoided in the flue gas which contains CO_2 with a purity up to 96-99% after the processing cycles. The carbon dioxide is later compressed and condensed into liquid CO_2 so it could be sequestered or used to synthesize other chemical products. As large amount of oxygen will be consumed in the above process, how to produce oxygen efficiently and economically in large scale becomes very important.

Nowadays, commercial oxygen is usually produced by cryogenic distillation or pressure swing adsorption. However, both technologies require large capital investment and energy consumption throughout the production cycles.[6] Dense ceramic oxygen permeable membrane (OPM) has attracted considerable attentions during the past decades for its unique selectivity and intrinsic high tolerance to the harsh operation environments. It has become one of the key technologies within clean energy field and grow rapidly since Teraoka et al. found that oxygen ions could permeate through dense disk ceramic membranes based on $La_{1-x}Sr_xCo_{1-y}Fe_yO_{3-\delta}$ perovskites in 1980s.[7] It is evaluated that capital saves up to 48% and power saves up to 69% after using the OPM technology to replace the cryogenic process. What's more, OPM can be integrated into oxyfuel process, which combines oxygen production and fuel oxidation at the same time (Figure 1.1) reduced auxiliary power equipment thus further increasing the efficiency at less cost and energy usage.[8, 9]

There are two main air separation systems based on the conducting ceramic membranes are pure ionic conductors or mixed ionic and electronic conductors (MIEC).[10] As oxygen transport as ions, an electron flux must transport in the opposite direction to compensate for oxygen flux thus keeping electrical charge being neutral. In Figure 1.2(a) which membrane material could only conduct ions, electrodes are provided as pathways for electrons. In this scenario, the generated oxygen could be controlled by adjusting the applied current which leads to devices named as oxygen pumps. While in Figure 1.2(b), no electrodes are required to operate the membrane due to the conduction of electrons in the membrane itself. The oxygen permeation membrane could be categorized as two types based on the conducting phase. Like perovskite material which possess both ionic and electronic conduction, the membrane only consists of single phase. While in dual phase membrane, ions and electrons are transported in related conducting phases independently.

For a MIEC, at air feeding side, gaseous oxygen transfer and adsorbs on the membrane surface. The oxygen absorbed at oxygen vacancy sites reduced and combined with vacancies to form lattice oxygen. The process could be described in Kroger-Vink notation:

$$O_2 + 2V_{\ddot{O}} \rightarrow 2O_O^X + 4h^{\cdot} \qquad (1-1)$$

where $V_{\ddot{O}}$ means oxygen vacancies which hold two relative positive charge; O_O^X means lattice oxygen atoms which show electrical neutrality and $h^{\cdot}$ means electron hole which has one relative positive charge.

Then the lattice oxygen migrates to the other side through neighboring vacancies or interstitial sites of atoms under the driving force of oxygen partial pressure gradient

across the membrane at elevated temperatures. Meanwhile, electrons conduct in the opposite direction to compensate the ion flux.

$$O_O^X\left(P'_{O_2}\right) \rightarrow O_O^X\left(P''_{O_2}\right) \quad (1-2)$$

$$h^{\cdot}\left(P'_{O_2}\right) \rightarrow h^{\cdot}\left(P''_{O_2}\right) \quad (1-3)$$

Here, P'_{O_2} means oxygen partial pressure at higher air side while P''_{O_2} is the one at lower permeate side. Subsequently the lattice oxygen evolves into molecular oxygen, desorbs from the membrane surface, and oxidized to its gaseous form in a reverse reaction of the first step.

$$2O_O^X + 4h^{\cdot} \rightarrow O_2 + 2V_{\ddot{O}} \quad (1-4)$$

In general, the whole process is controlled by two main steps, i.e., the oxygen surface exchange in the first and last steps, bulk diffusion in the middle one. If oxygen transportation is assumed as the only rate controlling step, Wagner Equation is used to evaluate the oxygen permeation flux and related affecting parameters.[11]

$$J_{O_2} = -\frac{1}{16F^2} \cdot \frac{\sigma_i \cdot \sigma_e}{\sigma_i + \sigma_e} \cdot \nabla\mu_{O_2} \quad (1-5)$$

F is Faraday constant, σ_i, σ_e means conductivity of oxygen ions and electrons respectively. Actually, $\frac{\sigma_i \cdot \sigma_e}{\sigma_i + \sigma_e}$ in total is called the ambipolar conductivity. $\nabla\mu_{O_2}$ represents the chemical potential gradient of oxygen which could be expressed as below.

$$\nabla\mu_{O_2} = RT \cdot \frac{\partial lnP_{O_2}}{\partial x} \quad (1-6)$$

R and T stand for the gas constant and temperature respectively, *x* denote the distance along the direction of membrane thickness.

Based on Wagner Equation, we can tell the oxygen permeation flux is determined by the properties of materials (such as ambipolar conductivity) and operating conditions

(like temperature, gas partial pressure difference across the membrane). It is clear to see the reciprocal relationship between the thickness of membrane and permeation flux which means thinner membrane permeate more oxygen under the same operating environments. However, the Wagner Equation is only applicable when the bulk diffusion process dominates. So, when the oxygen surface exchange becomes rate limiting, there is a characteristic membrane thickness *Lc*, of which the exchange rate and diffusion rate are comparable.[12] Therefore, exploit novel materials with high ambipolar conductivity, decrease the dense membrane thickness, improve the surface exchange rates are the three main directions in developing high performance oxygen permeation membranes.

1.1.2 Solid Oxide Cell

Solid oxide cell generally stands for a combination of solid oxide fuel cell and solid oxide electrolyzer. Solid oxide fuel cell (SOFC) is one type of fuel cells which is able to convert chemical energy in fuels into electrical energy directly in a highly efficient and environmentally friendly manner.[13, 14] The fuels applicable for SOFCs may include not only hydrogen but also various hydrocarbon fuels and even carbon.[15, 16] The reverse operation of SOFCs leads to solid oxide electrolysis cells (SOECs), where hydrogen and/or carbon monoxide rich syngas are generated using electricity, water and/or carbon dioxide.[17] Hydrocarbon fuels can be further produced when combining syngas from SOECs with Fischer-Tropsch process.[18] Therefore, the combination of SOFCs and SOECs would create a carbon-neutral technology for clean energy conversions.

NASA is also interested in SOFC/SOEC technologies for the mission to Mars.[19-22] The study has shown that the atmosphere on Mars consists primarily of carbon dioxide. The SOEC technology may directly convert carbon dioxide into carbon monoxide and

oxygen in-situ. The generated oxygen could be used for life support system or oxidizer propellant for the return trip, and the carbon monoxide could be further processed to make methane as a fuel propellant or directly employed for SOFCs to generate electrical power.

The working principle of SOC based on oxygen-ion conducting electrolyte is shown in Figure 1.3. It is clear to see SOEC are actually the reverse process of SOFC. A typical SOC usually consists of three main components: an electrolyte, an air electrode and a fuel electrode.[23-25] Complex physiochemical reactions took place in each part of SOC and in total to complete reactions in providing power or electrolyzing target chemicals based on working mode. Take SOFC with CO as fuel input as an example.

At air electrode, oxygen diffuse and adsorbed to the surface. The oxygen molecules will be reduced into the oxygen ions, combining with electrons from external circuit, once they reach the TPB area (an area where triple phases, i.e., gas phase, electronic conducting phase, and ionic conducting phase meet) in the anode surface.

$$\frac{1}{2}O_2 + 2e^- = O^{2-} \qquad (1-7)$$

The obtained oxygen ions transport through the dense electrolyte via oxygen vacancies due to the chemical potential gradient. Because the diffusion energy barrier of oxygen ions is pretty high in current ceramic ionic conductors, high operating temperature is necessary for cells nowadays. At fuel electrode, fuel will be oxidized with oxygen ions and release electrons simultaneously which flow through an external circuit to the air side, thus fulfilling a complete reaction.

$$CO + O^{2-} = CO_2 + 2e^- \qquad (1-8)$$

In fact, it is only the oxidization reaction of a carbon monoxide which was divided into two parts and let them take place independently within their own domains. An ideal

SOFC could supply any amount of current as long as fuel is sufficiently provided, and a proportional relationship is shown based on the above reaction (i.e., each mole of provides *n* moles of electrons). However, the real output voltage is always less than the ideal output voltage. Moreover, the more current is drawn, the lower output voltage will supply. This is attributed to irreversible polarization (also called losses) during the operation of cells in practical and the losses can be categorized into three major types that each of them is associated with one basic step discussed above.

a) Activation losses due to electrochemical reaction which relates to the intrinsic properties of materials.

b) Ohmic losses due to the electrical resistance, including electrodes, electrolyte and etc.

c) Concentration due to because of the mass transport mainly comes from insufficient source supply.

Therefore, the real output voltage of a SOFC is described as:

$$V = E_0 - \eta_{act} - \eta_{ohm} - \eta_{conc} \qquad (1-9)$$

E_0 represents the ideal voltage output of a SOFC which can be calculated and predicted by Nernst Equation.[26, 27] η_{act}, η_{ohm}, η_{conc} corresponds to polarization due to activation, ohmic and concentration respectively. The performance of SOC is usually summarized and demonstrated in a *V*-*I* graph, which *I* stands for the current density ($A \cdot cm^{-2}$) and *V* represents the voltage (output voltage in SOFC mode and applied voltage in SOEC mode). The voltage at no current output is called open circuit voltage (OCV). As shown in Figure 1.4, the characteristic shape of graph exhibits the corresponding polarization stage clearly.[28]

1.2 Preparation of ceramic hollow fiber membranes

1.2.1 Ceramic hollow fiber membranes

In last decades, oxygen permeation membrane and solid oxide cell have made impressive progress with the emerged of novel materials in large numbers. People are taking steps in expanding these technologies and commercializing them. While the traditional design, either tubular or disk configuration, has shown disadvantage in usage efficiency because of low area/volume ratio (30-250 m^2/m^3) thus limiting their industrial scale application.[29, 30] Ceramic hollow fibers are hence introduced as alternate solution for their higher packing density, higher area/volume ratio (~3000 m^2/m^3) and more flexible operation mode (inside-out or outside-in). It has a configuration of microtubule with outer diameter less than 2 mm and usually shown as a membrane coated on the outside of a porous fiber support. Subsequently, these fibers will be bundled together and cement the ends before placing in a shell just as shown in Figure 1.5. [31, 32]

Hollow fiber membranes are first developed in the 1960s for reverse osmosis applications [33] and they are commonly produced using various polymers. The critical production process is referred as "spinning" which can be divided into four general types: [34]

(1) Melt Spinning, in which a thermoplastic polymer is melted and extruded through a spinneret into air and subsequently cooled.[35]

(2) Dry Spinning, in which a polymer is dissolved in an appropriate solvent and extruded through a spinneret into air.[36]

(3) Dry-Jet Wet Spinning, in which a polymer is dissolved in an appropriate solvent and extruded into air and a subsequent coagulant (usually water). [36]

(4) Wet spinning, in which a polymer is dissolved in an appropriate solvent and extruded directly into a coagulant (usually water). [36]

Unlike polymeric hollow fibers, the ceramic hollow fiber membranes demonstrate excellent performance even operated under harsh conditions: high temperature, high pressure or in organic solvents, acidic/basic solutions, oxidative/ reductive conditions. As a result, they have since become prevalent in many fields such as water treatment, desalination, cell culture, medicine etc. [37-40]

1.2.2 Phase inversion

People nowadays mostly use phase inversion technique to fabricate hollow fiber membranes because it requires just simple equipment and operation compared to traditional extrusion process. Phase inversion is a demixing process in which initially homogeneous polymer solution is transformed from a liquid state to a solid state in a controlled manner.[41] The transformation can be achieved by several ways[42]:

(1) TIPS (Thermally Induced Phase Separation): This method uses specific solvent which can dissolve polymers at high temperature while precipitates them at room temperature. As hot solution is casted onto the supports, demix occurs when the temperature cools down. TIPS is easy to process and create membrane has high porosity, less defect, and microstructures with narrow pore size distribution (PSD).[43]

(2) EIPS (Evaporation Induced Phase Separation): This method dissolves polymers in a mixture of solvents and nonsolvent. After casting the solution on the porous support with a doctor blade method, the solvent is evaporated thus inducing demix to happen and forming a thin and porous membrane on the support. It is also referred as the solution casting method.

(3) VIPS (Vapor Induced Phase Separation): Whenever a polymer solution is placed in an environment contains a nonsolvent (e.g. expose in air that contains water vapor), demix took place as nonsolvent is absorbed by the solution.[44]

(4) IP (Immersion precipitation): This is the most commonly used method and the total process can be described by a ternary phase diagram (Figure 1.6). Specifically speaking, after immersing the polymer solution in coagulation bath (nonsolvent, usually water), like point A in the graph, the exchange of solvent and nonsolvent makes the solution composition changes dramatically. The homogeneous solution moves from stable one phase region into two phase metastable region and starts to precipitate when reach the miscibility gap (Point B). Subsequently, the solution separates into a polymer-rich phase and a polymer-poor phase. The polymer-rich phase begins to solidify at point C and finish solidification at point D in the end. Different separation rates, either instantaneous or delayed demix, contributes to the final asymmetric structure. [45, 46] Instantaneous demix which indicates fast solvent-nonsolvent exchange prefer forming a porous skin layer with a finger-like sublayer. While delayed demix which means slow exchange rate favoring form a dense skin layer with a sponge like sublayer.

1.2.3 Phase inversion-sintering process

Unlike polymeric hollow fiber counterparts, ceramic hollow fiber membranes usually employ a combined phase inversion-sintering technique. Besides high temperature sintering, polymers serve as a binder to only hold ceramic particles together instead of acting as the membrane materials in ceramic hollow fiber membranes. As a result, the formation of ceramic hollow fiber membranes is more complicated, and their

microstructures are controlled by more factors.[47] As the technique includes only three major steps, membrane structure can be tailored by adjusting the related parameters.[48]

(1) Preparation of spinning suspension: Ceramic powders, polymer binders, and other additives are dissolved in solvents to prepare the spinning suspension. The controlling elements are listed below. (a) Ceramic powder particle size and distribution: the movement of particles with different sizes varies in the solution. Provided small particles move towards interface faster than bigger ones, a layered structure will be formed as shown in Figure 1.7.[49] In addition, smaller particles are easy to sinter and densify at high temperature then bigger particles. So, nano particles synthesized by combustion method or Penchini method is always used to fabricate dense membrane. (b) Concentration of ceramic powders in the solvent: the concentration directly affects the viscosity of the solution. The higher concentration of ceramic powders (solid content), the more viscous of the solution which lead to slower exchange rate, thus thicker and denser membrane. In contrary, higher concentration of solvent makes the solution less viscous which is good for the formation of finger-like channels in the membranes. Sometimes, nonsolvent (like ethanol or PEG) may be added into the starting solution to promote the growth of finger channel due to increased thermodynamic instability of the solution.[50] (c) Additives: additives could be used to adjust the viscosity of the solution. Moreover, some organic additives could help ceramic powders disperse well in the solution hence improve its uniformity and some mineral additives could promote the following sintering behavior of membranes.

(2) Spinning of hollow fiber precursors: The Suspension is added into a reservoir and pressurized into the coagulating bath to form hollow fiber precursors through a tube-in-orifice spinneret where inner coagulant flows simultaneously (Figure 1.8). Tuning the

exchange rate of solvent-nonsolvent by adjusting the parameters below could affect the microstructures of nascent hollow fibers directly. (a) Extrusion rates of suspension: slow extrusion rate can reduce the formation of finger-like voids while is good for dense membrane fabrication. So faster extrusion rate is applied when finger-like channels are expected. (b) Internal coagulant type and its flow rate: when water is using as internal coagulant, the influence of flow rates is similar to those of spinning rates of suspension; when NMP or NMP/H_2O mixer is used, either delay the coagulation of polymers thus promoting the extension of finger-like channels from outside or delay the demix rates thus inhibits the growth of finger-like voids inside depends on the concentration of mixer. (c) Air gap: a larger air gap is good for the formation of top dense layer, but the situation could be more complicated when coagulant changes into NMP or NMP/H_2O mixer. (d) Bath temperature: a higher bath temperature could enhance. the exchange rates thus facilitating the formation of finger-like channels. (e) Spinneret structure: the size of spinneret (inner and outer radius), flow angle of suspension also needs to be considered in affecting the final microstructures of the membranes.[51-55]

(3) High temperature sintering: Sponge-like layers usually densify during the high temperature sintering and eventually becomes gas tight for some ceramic materials. While finger-like voids above some certain size could still retain the shape even after sintering at elevated temperatures.[47] Sintering temperature, heating and cooling rates, dwelling time are also important factors in affecting the performance of the fabricated membranes.

1.3 Application of ceramic hollow fibers

1.3.1 Progress in hollow fiber oxygen permeation membranes

In 2000, J Luyten first reported to prepare $LaSrCoFeO_{3-x}$ hollow fiber oxygen permeation membrane using phase inversion spinning-sintering technique.[56] They use N-methyl-2-pyrrolidone (NMP) as solvent, and polyethersulfone (PESF) as polymer binder and water as coagulant to spin the nascent hollow fiber. Then they sinter the fiber at 1225 °C for 24h to obtain the dense membrane. The spinning rate and ratio of NMP to water of bore liquid were changed to try their influence on the bending strength of dense membranes.

Later, K. Li, XY. Tan took a series of investigation on fabricating and characterizing ceramic hollow fibers based on LSCF. They synthesized fibers which has a "sandwich structure": sponge like structure in the core which later densified after high temperature sintering, while finger like structure stayed on the outer and inner side of the fiber which still retained porous (Figure 1.9). The membrane deliver an oxygen permeance as high as 5.49×10^{-7} $mol\cdot cm^{-2}\cdot s^{-1}$ at 900 °C.[57] As water was used as coagulant, although remain porous, the porosity of inside and outside surface decrease sharply after sintering. Therefore, they use NMP (94 wt.%)- H_2O mixer as inner coagulant and got highly asymmetric LSCF hollow fiber membranes which possess an oxygen permeation flux of 0.11 - 2.19 $mL\cdot cm^{-2}\cdot min^{-1}$ in the temperature range of 650 - 1000 °C, which is 2.6 - 10.5 times higher than that of the sandwich-structured ones.[58] They also fabricated $BaBiCoNbO_{3-x}$ hollow fiber membranes based on this microstructure and got an oxygen flux as high as 14.1 $mL\cdot cm^{-2}\cdot min^{-1}$ at 950 °C.[59] Furthermore, they enhance the oxygen permeation by acid etching or adding methane in the Helium sweep gas to modify the inside

surface.[60, 61] Ag/Pt was also used to decorate the outside surface of hollow fibers in order to improve the total permeation by accelerating the oxygen surface exchange rates.[62] Other perovskite materials like $BaCoFeZrO_{3-x}$ [63-65] and $BaSrCoFeO_{3-x}$[66-70] are also used in fabricating hollow fiber membranes with various microstructures and modifications.

Due to the instability of perovskite materials under CO_2 atmosphere, dual phase oxygen permeation hollow fibers are also being prepared right now. C. Chen and S Liu etc. fabricates different kinds of dual-phase composite hollow fiber membranes. The membranes demonstrate decent performance and much better stability which show a huge potential in commercialization.[71-75] There are some other configurations like multichannel hollow fiber membranes or hollow fiber membrane bundles are also fabricated for oxygen permeation.[76-78]

1.3.2 Progress in hollow fiber solid oxide cells

Hollow fiber spinning-sintering technology has been widely applied used in preparing microtubular SOFCs (MT-SOFCs) due to its economy and simplicity. Recently, lots of groups have successfully fabricated MT hollow fiber using various methods. Among them, anode-based MT-SOFs which has feature of multiple-layered microstructures demonstrate the best performances.[79-85] However, both the sponge-like layer and the skin layers contain small and non-continuous pores thus inhibiting fuel/gas transport. As a result, the electrochemical performance of MT-SOFCs especially at the operating conditions of large current densities are still very limited. Investigations right now are focusing on eliminating either the middle-sponge-like layer or relatively dense inner surface skin layer of microtubular anode substrate. For example, optimize the slurry viscosity to reduce the thickness of mid sponge-like layer.[86]

Li's group has putted forward co-extrusion technique which extrude anode-substrate/electrolyte assembly in one-step. The electrolyte layer was attached to the sponge-like layer directly after extrusion which greatly simplifies the steps for cell fabrication.[87, 88] Our group has recently developed a novel strategy in preparing MT-SOFCs.[89] Based on co-extrusion phase inversion-spinning, the inner graphite layer was used as a sacrificial layer to eliminate the middle sponge-like layer and inner surface dense skin layer. The peak power density of the cell was ~1484 $mW \cdot cm^{-2}$ at 600°C, approximately 1.5 times that of a similar cell with an anode substrate fabricated from other extrusion method. It is also the highest performance among the SOFCs with the same material system in open literature.

1.4 Objectives

Tremendous effects have been devoted into finding materials to satisfy all the requirements that not only have perfect performance but also excellent chemical and mechanical strength. However, the developed materials that show exceptional high performance generally degrade quickly. A trade-off effect is standing in front, yet no materials right now could meet the large-scale application standards. Fabricating novel and beneficial microstructure, especially utilizing ceramic based hollow fibers featuring with radially well aligned microchannels open at inner surface, seems to be a vital solution.

In chapter 2, a microtubular solid oxide cell supported with nanostructure is fabricated and tested in CO/CO_2 mixer atmosphere to show its performance in both SOFC and SOEC modes. LSCF-ZnO composite hollow fiber based OPM for long-term operation under harsh thermal conditions is fabricated and optimized in chapter 3. In chapter 4, Co_3O_4 nanorod array is loaded onto the surface of GDC-LSCF dual phase OPM by hydrothermal

process to evaluate its influence. The effect of surface modification on air side and permeated side is studied and the underlying mechanism are discussed. In this work, SOC and OPM will be prepared and characterized based on novel microstructures to provide an insight of alternated method in improving the performance of SOC and OPM rather than developing novel materials.

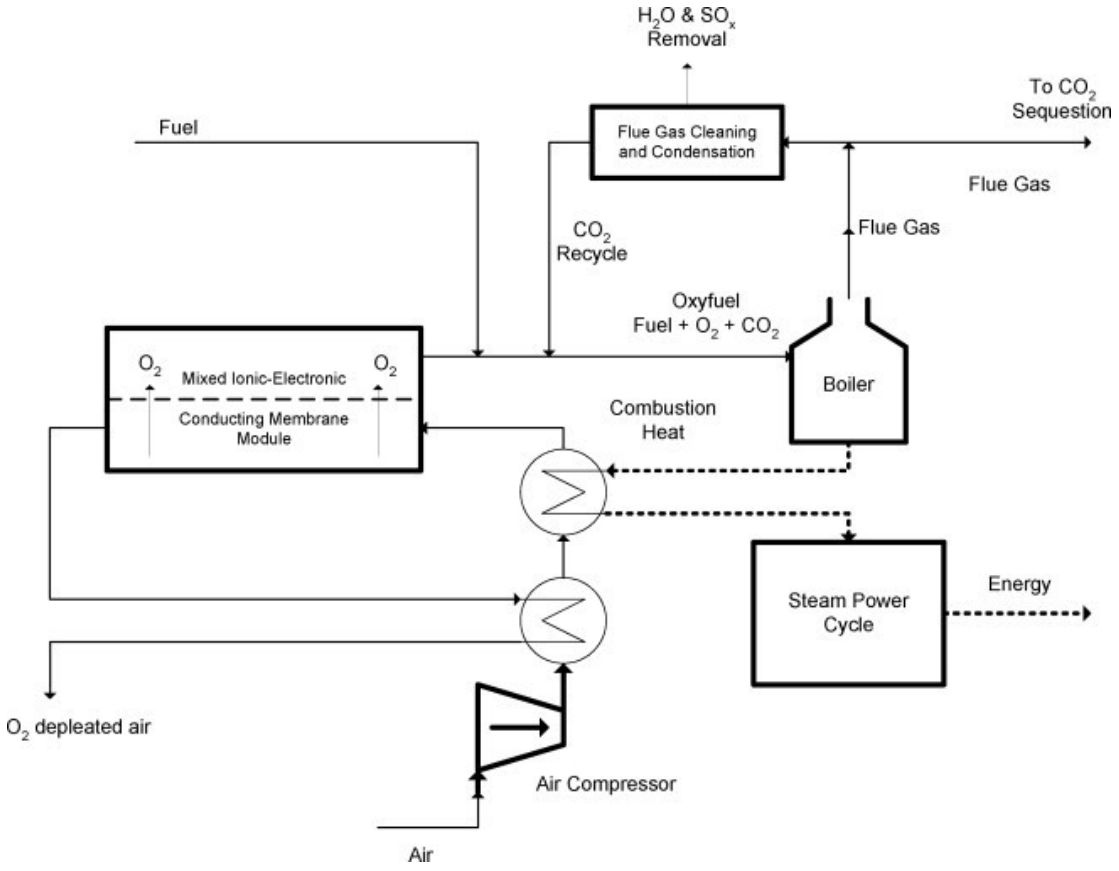

Figure 1.1 Schematic of an oxy-fuel power station utilizing an OPM unit.[8]

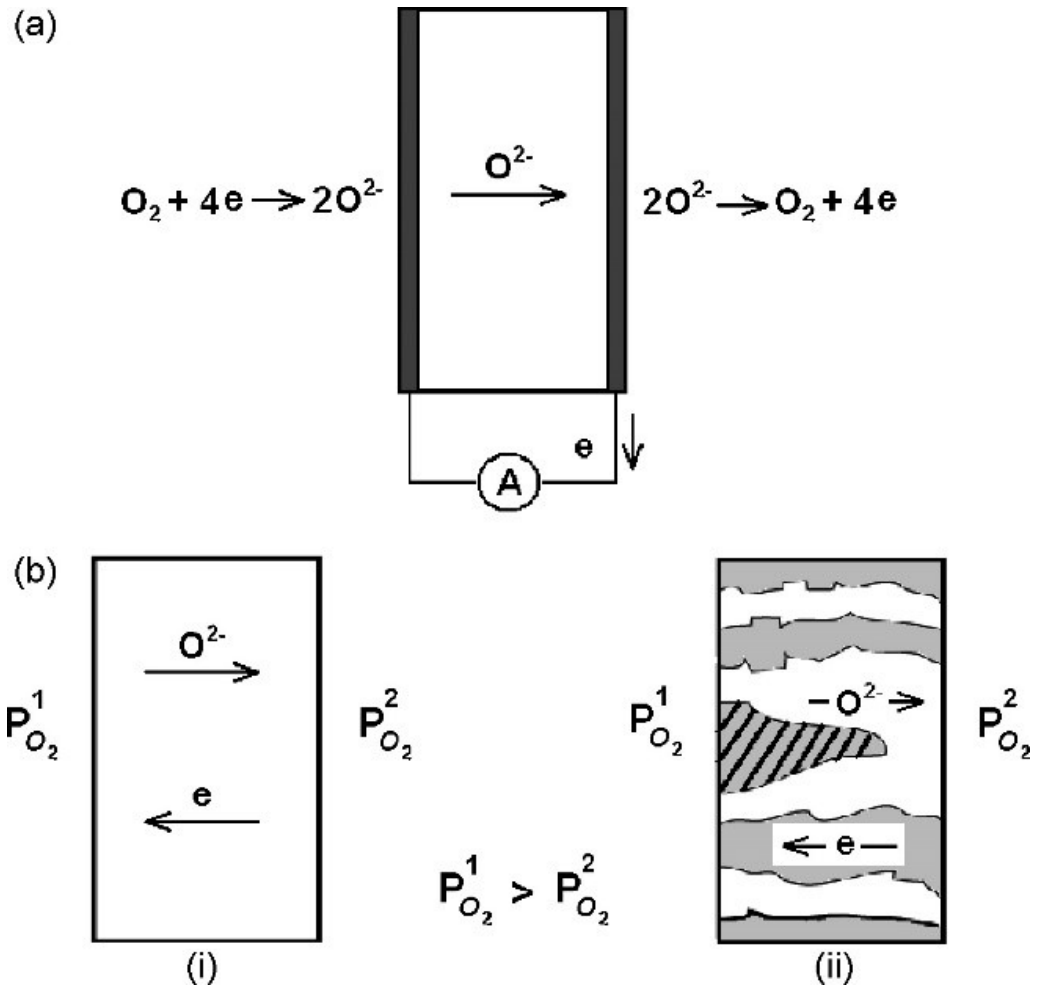

Figure 1.2 Ceramic membrane types based on conduction mechanism (a) solid electrolyte (b) mixed ionic–electronic (i) single phase membrane (ii) dual-phase membrane.[10]

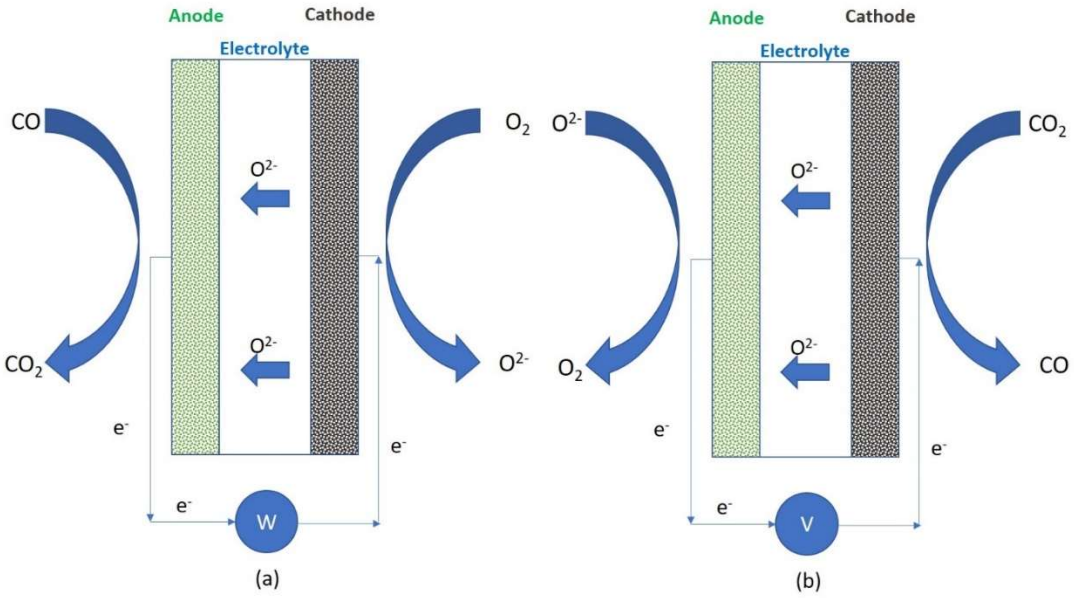

Figure 1.3 Working Principle of (a) SOFC and (b) SOEC.

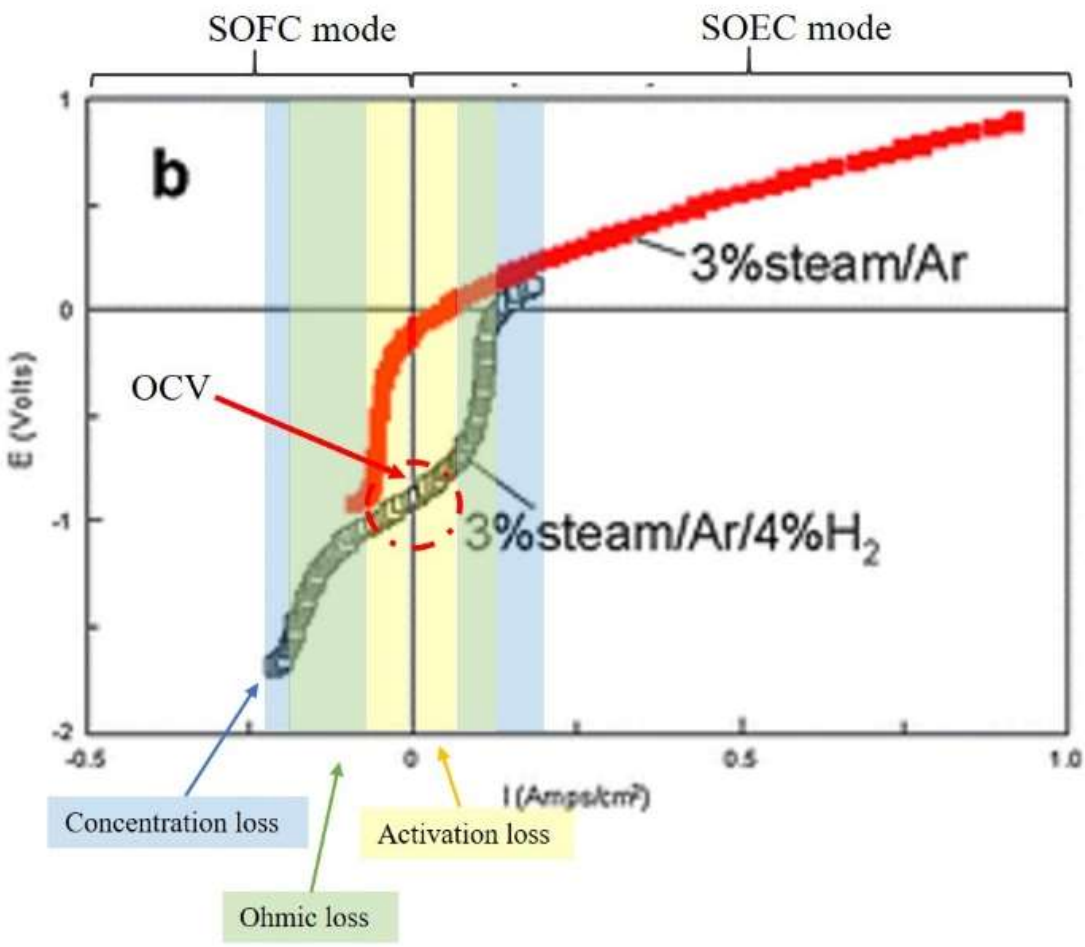

Figure 1.4 Typical V-I graph of SOC.[28]

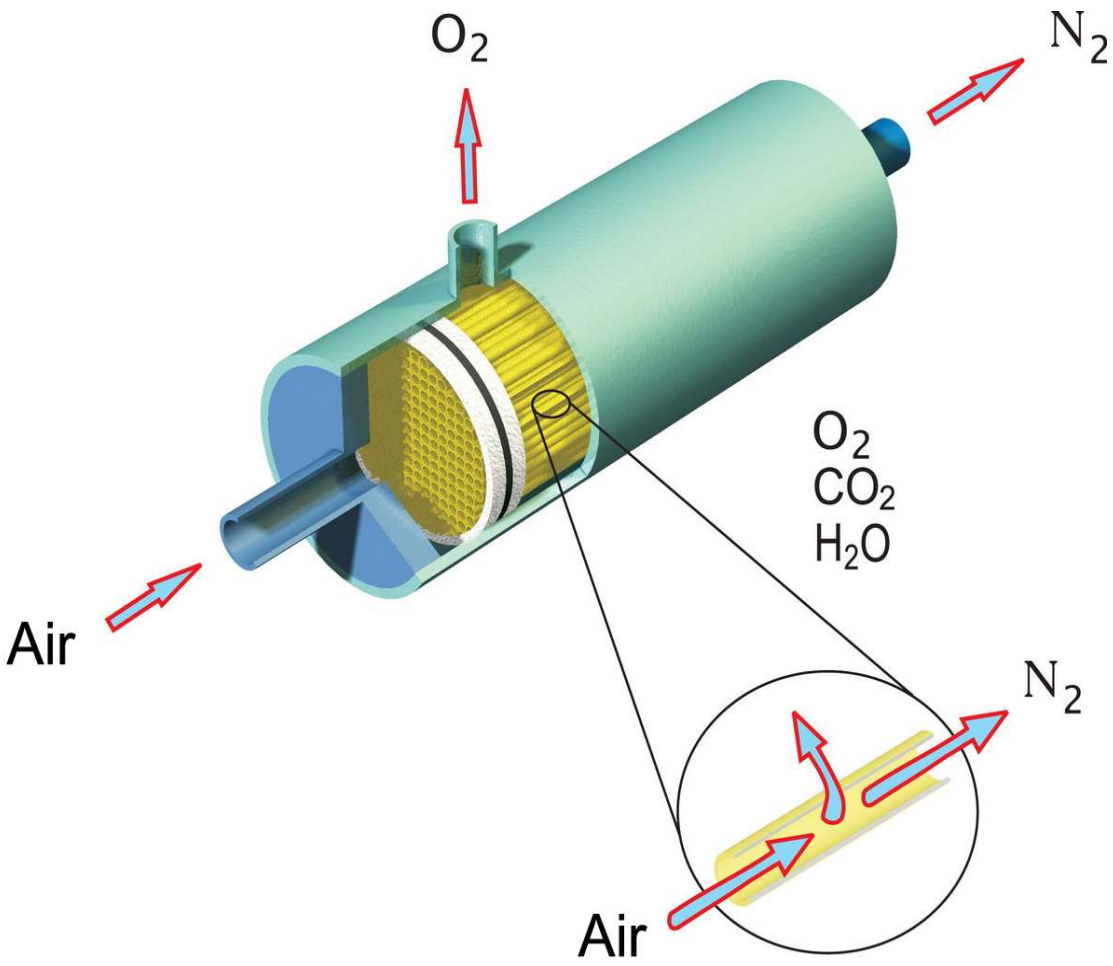

Figure 1.5 Schematic of a hollow fiber bundle used to separate oxygen, carbon dioxide, and water from air.[31]

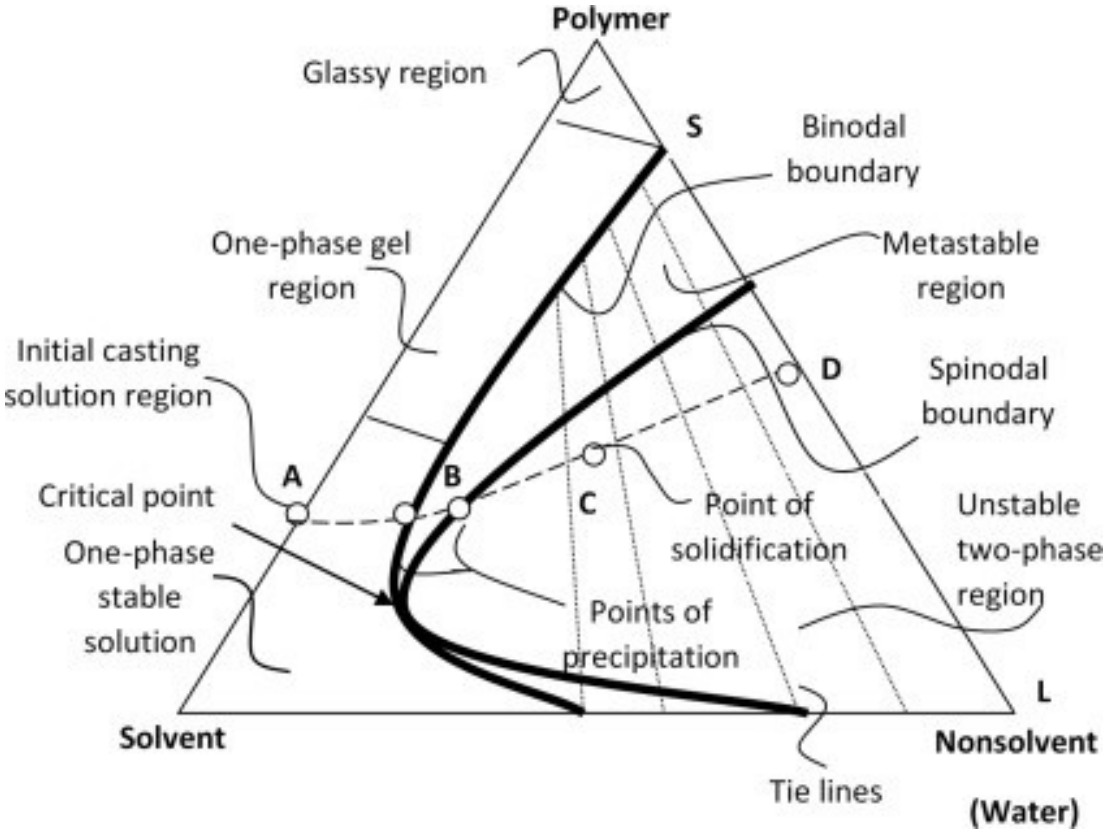

Figure 1.6 Schematic representation of the three-component phase diagram describing the formation of water-precipitation phase separation membranes.[45]

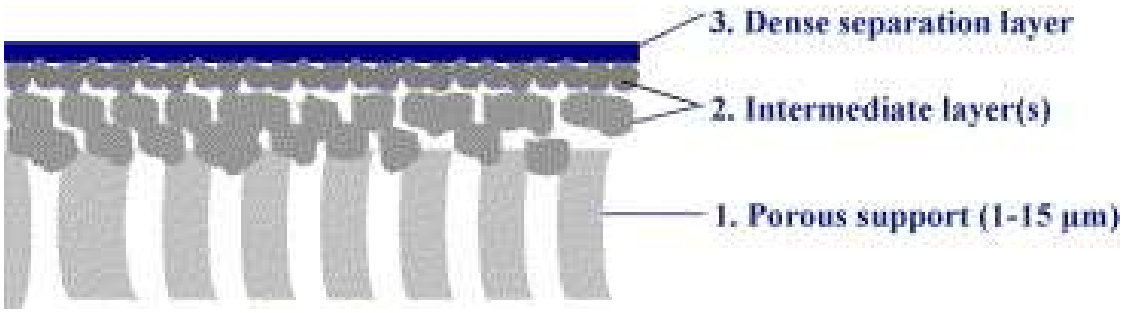

Figure 1.7 A general structure of ceramic membrane membranes.[49]

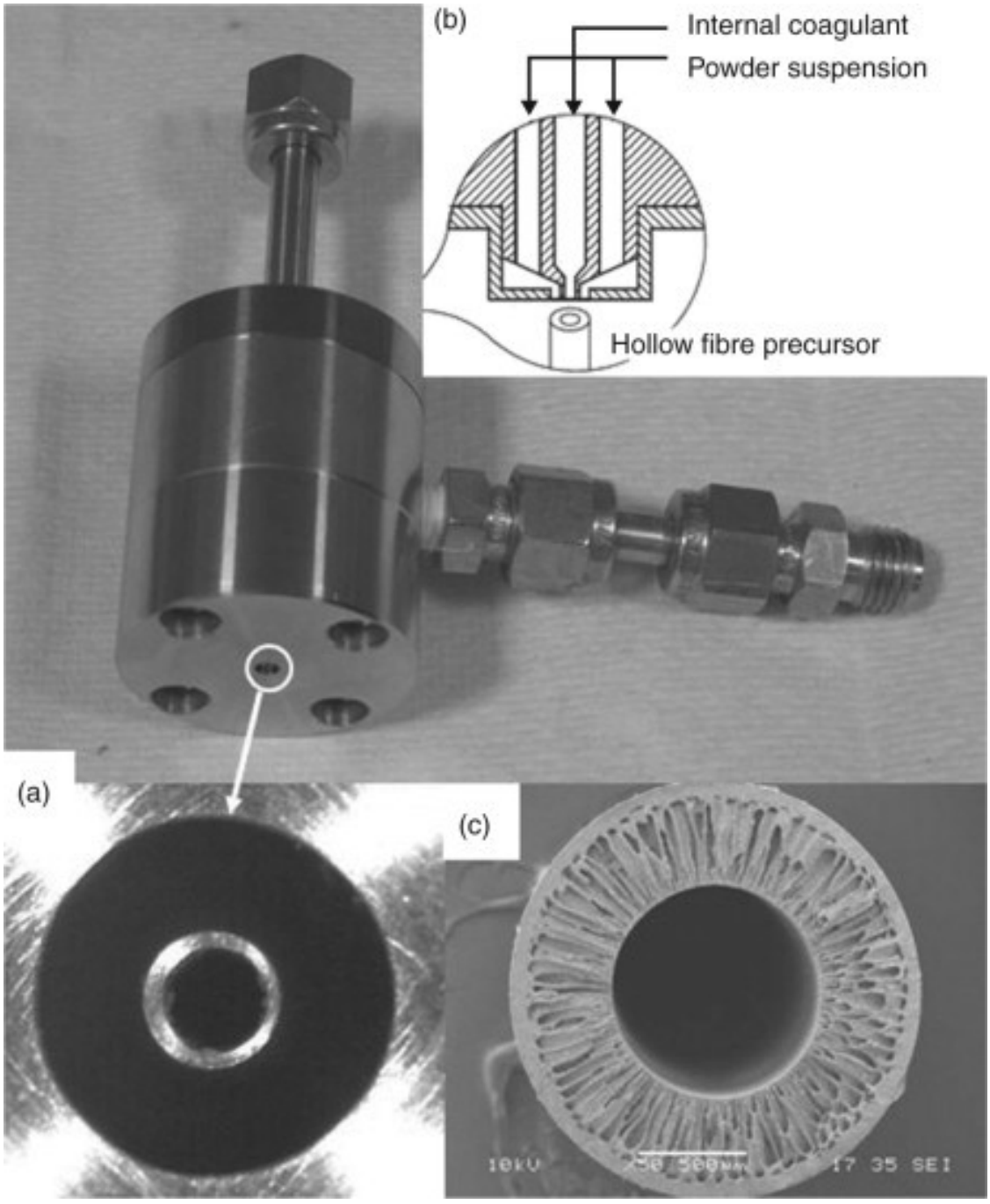

Figure 1.8 Structure of the spinneret (a and b) and (c) the hollow fiber membranes.

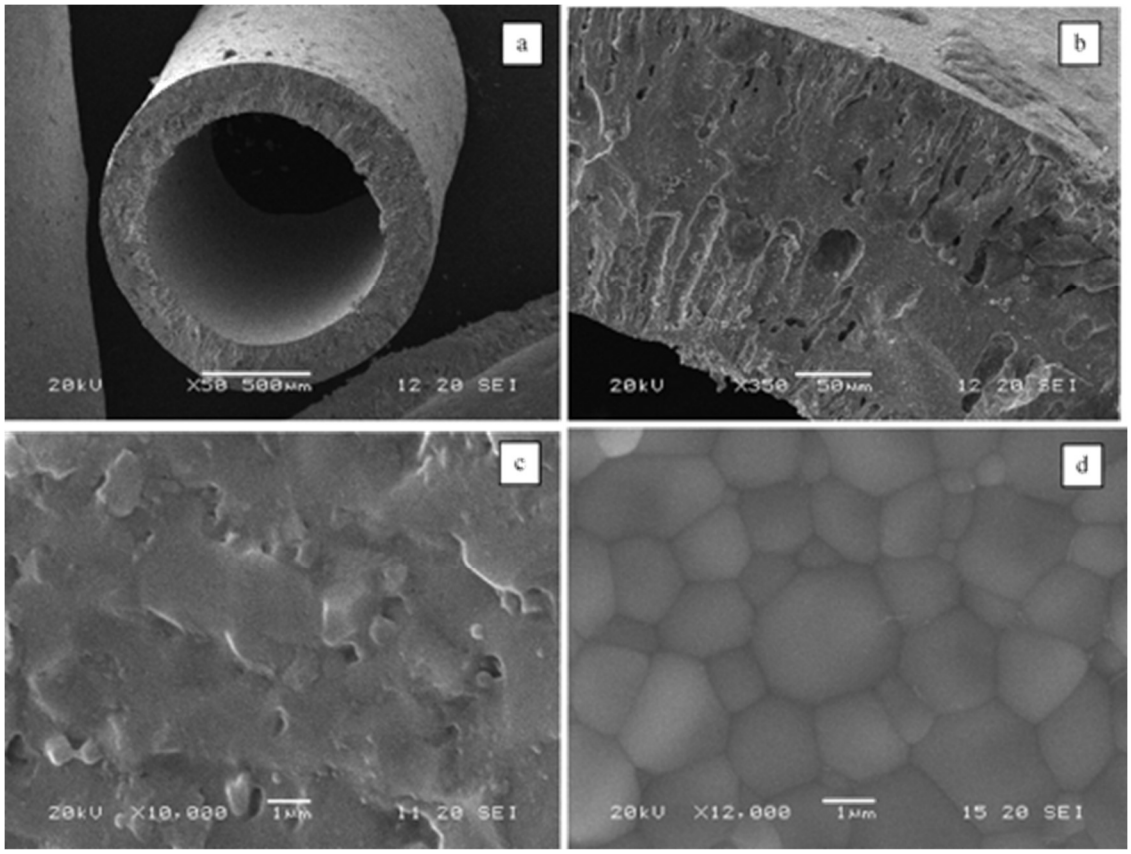

Figure 1.9 “Sandwich structure”: SEM micrographs of the LSCF hollow fibers sintered at 1280 °C.[58]

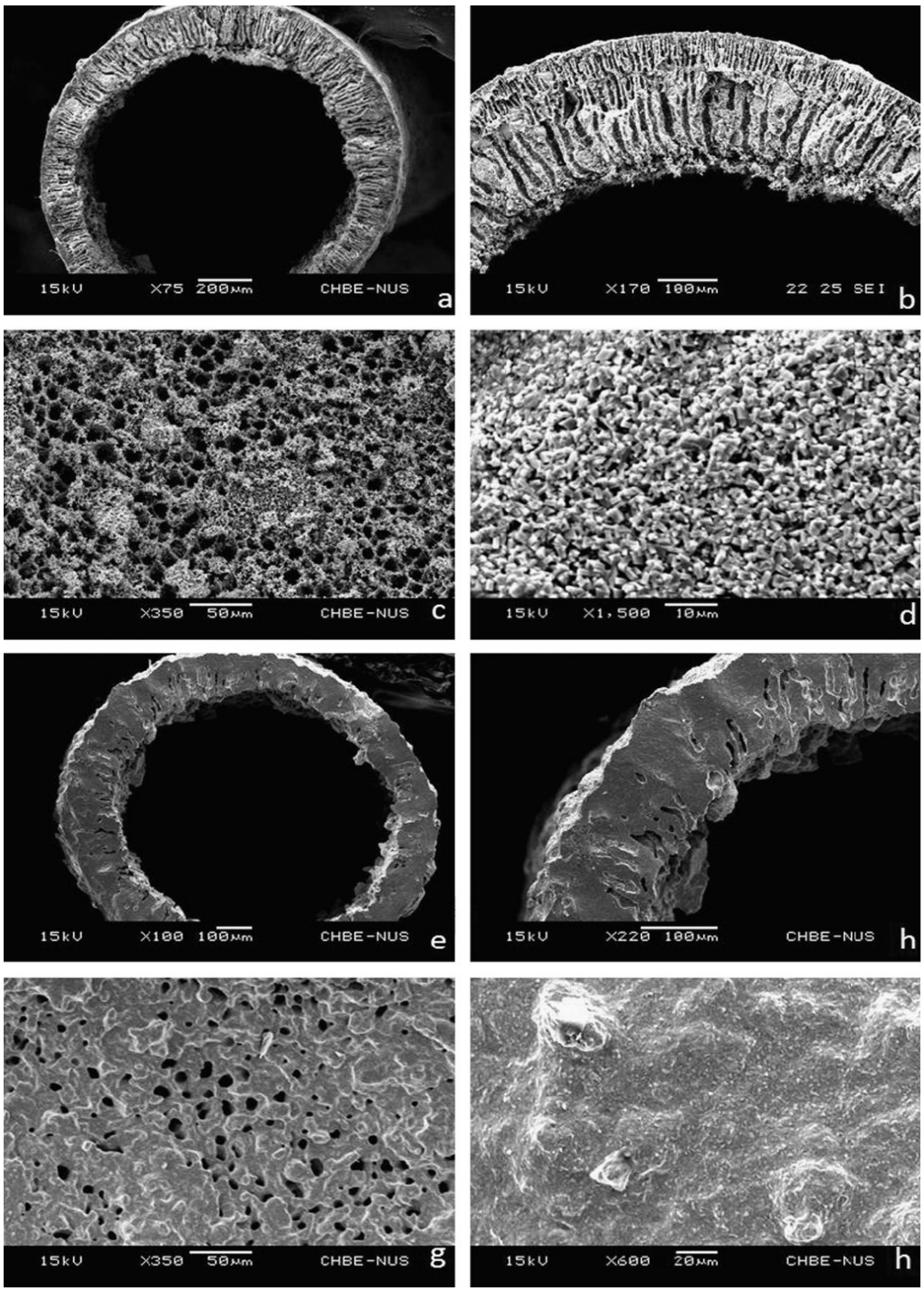

Figure 1.10 Highly asymmetric structure: SEM images of fresh hollow fiber membranes: (a) cross section, (b) fiber wall, (c) inner surface, (d) outer surface; and sintered at 1110 °C for 4 h: (e) cross section, (f) membrane wall, (g) inner surface, (h) outer surface

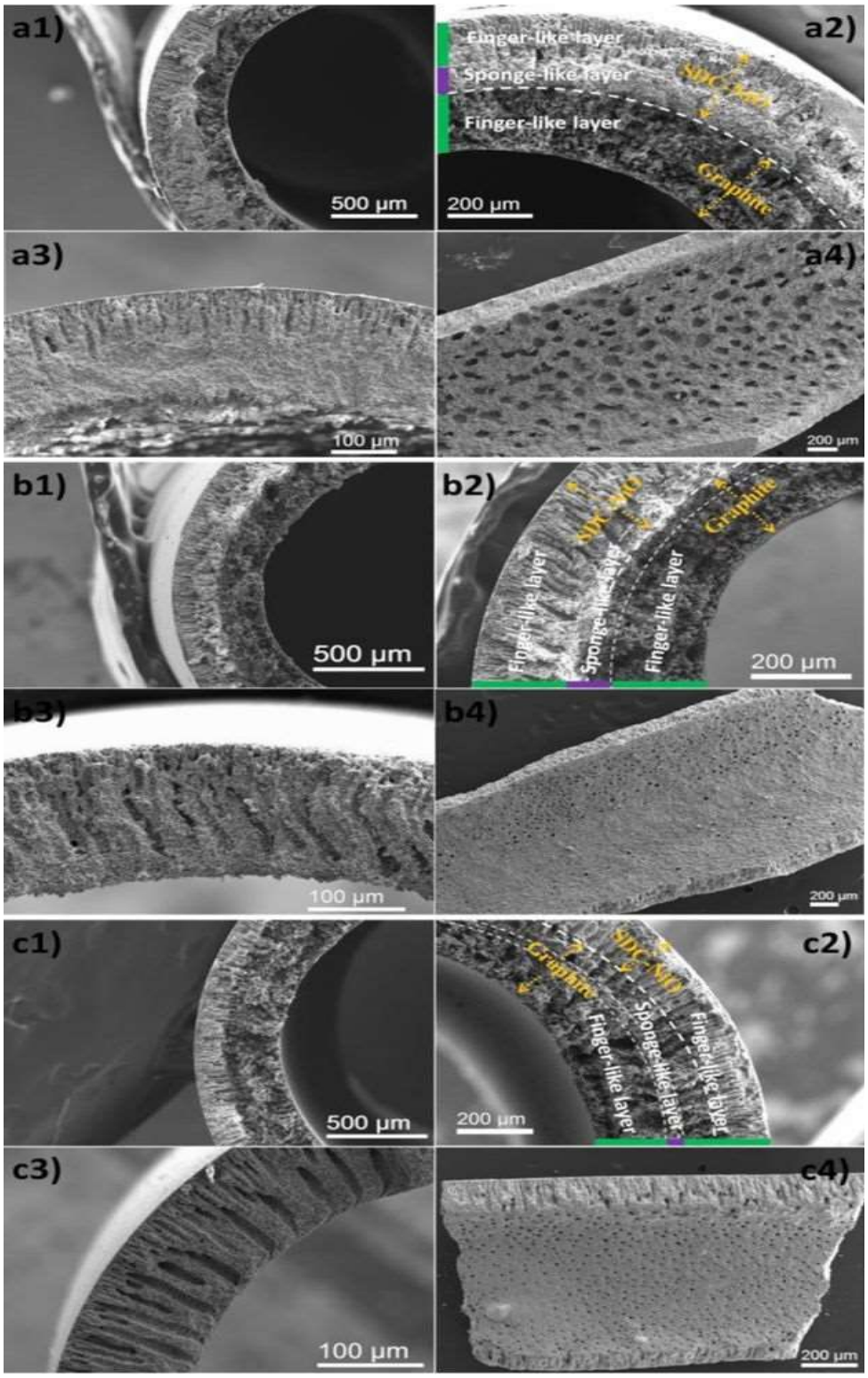

Figure 1.11 SEM images of the NiO-SDC/Graphite dual-layer micro-tubes prepared with different slurry compositions. (a) solid content 80 wt.%; (b) 75wt.% and (c) 70 wt.%.[89]

CHAPTER 2

FABRICATION AND CHARACTERIZATION OF MICROTUBULAR SOLID OXIDE CELL SUPPORTED WITH NANOSTRUCTURED MIXED CONDUCTING PEROVSKITE FUEL ELECTRODE

2.1 Introduction

Very complicated multi-physicochemical processes take place in a fuel electrode. These include fuel/gas species transport in pores, charge (electron and ion) transfer via porous electrode skeleton, surface catalytic reactions, and electrochemical reaction enabled fuel oxidations and/or reductions depending on cell operating modes, e.g., SOFC mode and SOEC mode.[90, 91] Accordingly, multiple functionalities are required for fuel electrode. These include the desired porous microstructures for facile fuel/gas diffusion, high electrical conductivity, high catalytic activity, good stability in reducing atmosphere, as well as good chemical and thermal compatibility with the electrolyte layer. The widely used fuel electrodes are nickel cermet electrodes, where nickel is composited with electrolyte materials to form the skeleton of porous electrodes. Because of nickel phase, Ni-cermet electrodes usually demonstrate excellent catalytic activity and high electrical conductivity. However, they also suffer from the issues of redox instability induced by reduction and oxidation of Ni phase, and micro-morphology instability induced by nickel phase agglomeration.[92] Additionally, carbon coking and sulfur poisoning may deactivate catalytic property of nickel surface when hydrocarbon fuels are utilized.[93] These issues

together with their complicated interactions deteriorate both electrochemical performance and long-term stability of SOCs.

To overcome the intrinsic drawbacks of Ni-cermet electrodes, nickel-free mixed conducting materials have been studied for fuel electrodes. These include a class of ABO3 type simple perovskites such as $La_{0.75}Sr_{0.25}Cr_{0.5}Mn_{0.5}O_3$ (LSCM) [94] and double perovskites e.g., $Sr_2Mg_{1-x}Mn_xMoO_{6-\delta}$ [95], $PrBaMn_2O_{5+\delta}$ [96], and their derivatives [97]. It has been realized that electrical conductivities of p-type conducting perovskites, e.g., LSCM, decrease upon reduction, while those of n-type conducting perovskites such as the doped strontium titanates, (La, Sr)TiO_3 (LSTO), increase after reducing treatment.[98] Since the fuel electrode is usually operated in a reducing atmosphere especially under SOFC mode, the n-type conducting perovskites are preferred for fuel electrode. On the other hand, the catalytic properties of mixed conducting perovskites are in general much lower than that of nickel. To take advantage of conducting perovskites while achieving high surface catalytic property, nickel nanoparticles are loaded onto the inner surface of porous fuel electrode through infiltrations.[99, 100] It usually takes multiple times for infiltration technique to obtain sufficient Ni nanoparticle loading, and Ni nanoparticles distribution on the surface of porous electrodes could be non-uniform. Furthermore, the micro-morphological stability of Ni nanoparticle-infiltrated porous electrodes could be a potential issue, especially in long-term operating conditions.[101] Alternative method is also used to generate surface Ni nanoparticles. In particular, the catalytically active transition metals, e.g., nickel, is incorporated into the perovskites through B-site doping at material synthesis stage. A part of doped nickel would then be exsolved from the B-site and decorated onto the surface of porous electrode upon reducing treatment.[102, 103] This method tends to

introduce more uniform distribution of surface Ni-nanoparticles while obtaining relatively stable surface micro-morphologies.

The SOFCs are primarily electrolyte-supported planar designs when conducting perovskites are employed as fuel electrodes.[104, 105] While the electrolyte supported SOFCs are relatively easy to fabricate, the thick electrolyte support layer usually induces very high ohmic resistance. To reduce thick electrolyte induced ohmic resistance loss, electrode-supported designs are usually utilized. Since the polarization loss of cathode electrode is a major factor limiting the overall efficiency of SOFCs due to the sluggish oxygen reduction reactions,[106] the anode electrode (typically Ni-cermet) -supported designs have been widely employed. Furthermore, the Ni-cermet anode electrode support is physically and chemically more compatible with oxide electrolytes than the cathode electrode support in high temperature sintering conditions. However, the anode-supported designs with metal oxides as anode materials, e.g., conducting perovskite, are difficult to fabricate. In general, high sintering temperature is needed to co-fire the anode substrate/electrolyte assembly to densify the thin electrolyte layer, which in turn could destroy the porous microstructure of anode substrate, resulting in the loss of anode porosity and increased concentration polarization resistance. Very few studies have investigated the fabrications of mixed conducting perovskite anode supported SOFCs, which is primarily confined to planar type of SOFCs in the open literature.[107] The tubular counterparts are rarely studied to our best knowledge especially the mixed conducting perovskite anode-supported microtubular SOFCs. Microtubular SOFCs may provide advantages of high volumetric power density, easy sealing requirement, and good thermal-shock resistance. However, the fabrication of

microtubular SOFCs is usually very difficult particularly the perovskite anode-supported ones.

In this chapter, $(La_{0.3}Sr_{0.7})_{0.9}Ti_{0.9}Ni_{0.1}O_{3-\delta}$-$Sm_{0.2}Ce_{0.8}O_{1.9}$ (LSTN-SDC) supported microtubular solid oxide cell LSTN-SDC/YSZ/LSM was studied. The microtubular fuel electrode substrate LSTN-SDC was prepared using spinneret extrusion in combination with modified phase inversion method, featuring radially well-aligned micro-channels open at the inner surface. Built upon the substrate fabrication, thin film YSZ electrolyte layer and LSM oxygen electrode layer were coated followed by sintering alternatively to form single microtubular cells. Upon reducing treatment, Ni nanoparticles were exsolved from LSTN crystal grains and uniformly decorated onto the inner surface of micro-channels, enabling high surface catalytic activity of substrate electrode. The fabricated microtubular cells were systematically measured and characterized with CO/CO_2 gas mixture as the fuel under SOFC mode and SOEC mode as well as SOFC-SOEC reversible mode, and the complicated electro-/chemical reactions were identified in the electrode substrate. The electrolysis process in combination with surface catalytic process of nanostructured substrate electrode resulted in highly efficient CO production from CO_2. The conversion efficiencies were well above 100% and tended to increase with increasing the applied cell voltages beyond open circuit voltages. The redox stability advantages of the cell were demonstrated in both alternative reduction (CO)/oxidation (air) atmospheric conditions and reversible operating mode.

2.2 Experimental

2.2.1 Materials synthesis and preparation of microtubular substrates

All the chemicals used in the experiments were purchased from VWR and used as purchased unless otherwise specified. $(La_{0.3}Sr_{0.7})_{0.9}Ti_{0.9}Ni_{0.1}O_{3-\delta}$ (LSTN) powders were synthesized by solid-state reaction method. Specifically, stoichiometric amounts of La_2O_3, $SrCO_3$, TiO_2, NiO were mixed in ethanol and grinded with zirconia ball milling for 1 h. After drying, the mixed powders were pressed into pellets under the pressure of 7 tons followed by calcinating at 1400 °C for 10 h in air to form LSTN phase. The calcinated pellets were then grinded into powders for use. $(La_{0.8}Sr_{0.2})_{0.95}MnO_{3-\delta}$ (LSM) powders were prepared using the same method with a calcinating temperature of 1100 °C for 3 h in air. Here the A-site deficient compositions of both LSTN and LSM are employed. The A-site deficiency of LSTN is used to facilitate the exsolution of Ni nanoparticles upon reducing treatment and therefore improve the catalytic property of fuel electrode. The A-site deficiency in LSM is utilized to improve the formation of oxygen vacancies and thus the performance of oxygen electrode.

Although LSTN is a mixed conducting material, its ionic conductivity is much lower than that of doped ceria. Therefore, LSTN-SDC composite is employed to improve ionic conductivity of fuel electrode. LSTN-SDC microtubular substrate was prepared through spinneret extrusion in combination with modified phase inversion process. Specifically, the synthesized LSTN powders were mixed with commercial SDC powders (SDC, Fuel cell materials, Ohio, USA) in the weight ratio of LSTN:SDC = 6:4. The powder mixture was then put into ethanol, which was ball-milled for 2 h to form a uniform mixture and subsequently dried at 80 °C overnight. Polyethersulfone (PESf, Veradel 3000P, Solvay

Specialty Polymers, USA; 5.1 wt.%) and polyvinylpyrrolidone (PVP, K30, CP, Sinopharm Chemical Reagent Co., China; 0.73 wt.%) were dissolved in N-methyl-2-pyrrolidone (NMP, HPLC grade, Sigma Aldrich, USA; 25.52 wt.%) and ball-milled for 2 h to form an organic solvent. The LSTN-SDC powder mixture (63.65 wt.%) prepared above and graphite powder (MTI, USA; 5 wt.%) were added into the organic mixture and ball-milled for 48 h to form a homogeneous slurry. The as-prepared slurry was de-aired for 10 min and then used for microtubular substrate extrusion. The in-house built spinneret extrusion system and process control parameters were detailed elsewhere. [89, 108] The de-aired slurry was first loaded into the chamber of a stainless-steel die. A double orifice spinneret with outer diameter of 2.6 mm and inner diameter of 1.6 mm was attached at the bottom of the chamber. The mixture of NMP (95 vol. %) and tap water (5 vol. %) was used as internal coagulant. The internal coagulant and slurry co-flew through the spinneret orifice. The flow rates of the slurry and internal coagulant were driven and controlled by a pressurized nitrogen gas system with flow meters (Seven Star, China). Tap water was used as external coagulant. The air gap between the tip of spinneret orifice and the surface of water bath was close to zero. Once the extruded slurry was immersed into the water bath, the microtubular precursor was formed and phase-inversion process took place. The exchange between water (non-solvent) in the bath and NMP (solvent) in the slurry led to the formation of radially well-aligned micro-channel pores, which were open at the inner surface of the microtubular precursor. In the meantime, solidification process occurred due to the decrease of solvent (NMP) concentration in the microtubular precursor. The extruded microtubular green bodies were left in water bath for 24 h, allowing for the completion of the exchange and solidification process. The precursors were then dried in air and cut into

desired length as electrode substrate. The substrates were then pre-sintered at 1200 °C for 5 h in air to achieve sufficient mechanical strength for subsequent coating process of single cell fabrications.

2.2.2 Fabrication of fuel electrode-supported micro-tubular single cells

Solution for dense electrolyte layer coating was first prepared. In particular, commercial YSZ powders (Fuel cell materials, Ohio, USA) were mixed with dispersant, plasticizers, and binder in a solvent, which was ball-milled for 7 days to form a solution before use. The composition of the prepared electrolyte solution is detailed in Table 2-1. Pre-sintered LSTN-SDC microtubular substrates were sealed at both ends using PTFE films and vertically immersed into the prepared YSZ electrolyte solution for 30 seconds, then dried up in air at room temperature. Such a coating procedure was repeated for 7 times. The coated samples were then fired at 1400 °C for 5 h in air to densify the electrolyte layer and form half-cells. The synthesized fine LSM powders were grinded with ethylcellulose and α-terpineol to prepare a cathode ink. The as-prepared ink was brush-painted onto the YSZ electrolyte of the half-cells, followed by sintering at 1100 °C for 3 h in air to obtain single microtubular cells.

2.2.3 Characterization and electrochemical measurement

Phase purity of the synthesized LSTN and LSM materials were examined at room temperature using X-ray diffraction (XRD, D/MAX-3C) in the range between 10^{o} and 90^{o} (2θ) at a scanning rate of $5°\ min^{-1}$. The phase compatibility between LSTN and SDC is also examined using XRD technique. The microstructures of as-prepared substrates as well as single cells were observed by scanning electron microscopy (SEM, Zeiss Ultra plus FESEM, Germany). The exsolution and distribution of nickel nanoparticles on the surface

of microtubular substrates were analyzed using SEM in combination with Energy-dispersive X-ray spectroscopy (EDS, Oxford Instrument detector).

The LSTN-SDC substrate precursors were sintered at 1400 °C for 5 h in air and then reduced at 850 °C in CO for 5 h. The gas permeability of the sintered substrates was measured before and after the reducing treatment, respectively. The apparatus and associated system for gas permeability measurement of microtubular substrates were described elsewhere.[89]

The electrochemical performance of fuel electrode-supported microtubular cell LSTN-SDC/YSZ/LSM was measured in SOFC mode and SOEC mode as well as SOFC-SOEC reversible mode. Platinum paste was painted onto the LSM electrode and end of LSTN-SDC electrode as current collectors. Silver wire was wound around the LSM electrode and at either end of LSTN-SDC substrate to serve as external circuits. The electrochemical test stand is schematically shown in Figure 2.1. The single cell was connected and sealed to alumina tubes at both ends using ceramic paste (Aremco products, Inc. USA). The alumina tube-cell-alumina tube assembly was supported by another alumina tube. The temperature of the cell was controlled by a tube furnace (MTI, USA). The LSM electrode was exposed to ambient air while CO or the mixture of CO and CO_2 was supplied to the LSTN-SDC electrode through the alumina tube connected to the cell depending on the operating modes. The flow rates of fuel/gas were controlled by precision flowmeters (APEX). The compositions of effluent gases from LSTN-SDC electrode were analyzed by an on-line gas chromatograph (GC-8A, Shimadzu, Japan). The voltage-current (*V-I*) curves and electrochemical impedance spectra (*EIS*) were measured using a Zahner IM6E electrochemical workstation with a voltage perturbation of 10 mV over a frequency

range from 0.01 Hz to 1 MHz. Nitrogen gas was first supplied to the LSTN-SDC electrode of the cell at room temperature. The cell was then heated up from room temperature to 850 °C at a rate of 2 °C per minute. Once the temperature of the cell reached 850 °C, the gas supplied to the LSTN-SDC electrode was switched from nitrogen to humidified hydrogen. The LSTN-SDC electrode reduction under this condition was last for 5 h, and the humidified hydrogen was then switched to CO or the mixture of CO/CO_2 for further electrochemical testing in different modes.

In SOFC operating mode, pure CO with the flow rate of 5, 15, and 30 $mL \cdot min^{-1}$ was supplied into the LSTN-SDC electrode respectively. The *V-I* curves of the cell were measured at different fuel flow rates. The corresponding *EIS* curves were obtained at open circuit voltage (OCV) conditions. The redox cycling test was also conducted, where pure CO and air were supplied into the LSTN-SDC electrode alternatively with nitrogen as a purging gas in between. The flow rates of both pure CO and air were 30 $mL \cdot min^{-1}$. The duration of CO and air supplies within each redox cycle varied from one to another. The duration of nitrogen purging was about 10 minutes in each cycle. The total time length of redox operations was about 24 h. And the OCV history of the cell was measured.

The SOFC-SOEC performance of the cell was measured in a coherent manner. The gas mixture of CO and CO_2 with the ratio of $CO:CO_2$ = 2:1, 1:1, and 1:2 was supplied to the LSTN-SDC electrode respectively. The overall flow rate of the gas mixture was controlled at 30 $mL \cdot min^{-1}$ for each of the three cases. The external potentials applied on the cell were varied from 0.2 V to 2.0 V, therefore both SOFC and SOEC performance were measured simultaneously. The corresponding *V-I* curves were recorded under mixed fuel flow rate of 30 $mL \cdot min^{-1}$ at each $CO:CO_2$ ratios. The EIS was measured at different

potentials applied on the cell, e.g., 0.2, 0.4, 0.6, 0.8, 1.4, 1.6, and 2.0 V, respectively, at each $CO:CO_2$ ratios. In addition, short-term stability test of SOEC performance was carried out under the supplied gas mixture of $CO:CO_2$ = 15 $mL \cdot min^{-1}$:15 $mL \cdot min^{-1}$ and at applied external cell potentials of 1.4, 1.6 and 2.0 V respectively. The SOEC test was run for 1 h under each external potential, which was then step-changed to another external potential. The time history of cell currents was recorded, and the corresponding compositions of effluent gases from LSTN-SDC electrode were analyzed.

The reversible operations between SOFC mode and SOEC mode were also conducted. The gas mixture of $CO:CO_2$ = 15 $mL \cdot min^{-1}$:15 $mL \cdot min^{-1}$ was supplied to LSTN-SDC electrode. The applied voltage on the cell was switched between 0.4 V (i.e., SOFC mode) and 1.6 V (i.e., SOEC mode). In each cycle, the duration of the applied voltage 0.4 V lasted for 2 h while that of the 1.6 V lasted for 1 h. A total of 5 cycles was continuously carried out for the reversible operations. The time history of cell currents was recorded accordingly.

2.3 Results and discussions

Figure 2.2a and Figure 2.2b show the XRD patterns of the synthesized LSTN and LSM powders, respectively. The diffraction peaks of LSTN can be well indexed to a single cubic phase structure according to the PDF card of No. 79-0185 with a space group of Pm-3m, while those of LSM can be indexed to a pure hexagonal phase structure (R-3C) according to the PDF card of No. 53-0058. These peaks are very sharp, indicating that the synthesized powder materials LSTN and LSM were well crystallized. No peaks corresponding to other phases could be detected.

Figure 2.3a shows the cross-sectional SEM image of the as-prepared LSTN-SDC micro-tubular substrate after pre-sintering treatment. It is clear to see that radially well-aligned micro-channels are embedded in the substrate. The diameters of the micro-channels are varied in the range of about 15 ~ 25 μm. Near the shell side of the substrate, the diameters of micro-channels become smaller, but the density of micro-channels increases. One also can see that the micro-channels are open at the inner surface of the micro-tubular substrate (Figure 2.3b). The micro-tubular substrate with such microstructures facilitates facile fuel/gas diffusion and increases the density of electrochemical reaction sites especially near the substrate/electrolyte interface.

To demonstrate advantages of such microstructures for facile gas diffusion, the gas permeability of the as prepared microtubular substrate was carried out. As shown in Figure 2.4a, the gas permeability of the microtubular substrate before the reducing treatment reached 20×10^6 L m^{-2} h^{-1} bar^{-1}, approximately one order of magnitude higher than the best gas permeability of microtubular substrates fabricated using the similar method in literature.[108] After reducing treatment, the sample demonstrated similar gas permeability (Figure 2.4b), implying that the porous microstructure of the substrate is redox stable.

After sintered at 1400 °C in air for 5 h, the phases of LSTN-SDC electrode substrate were examined using XRD and the results are shown in Figure 2.5a. It can be seen that the peaks correspond to LSTN and SDC phases respectively. No other phases can be detected, indicating the excellent chemical compatibility between LSTN and SDC. Since the LSTN-SDC electrode is subject to reducing conditions in SOFC mode, the phases of LSTN powder materials were further examined after reducing treatment in CO at 850 °C for 5 h. The XRD patterns of as-synthesized LSTN powders and after reducing treatment are

shown in Figure 2.5b. It can be seen that a new peak appeared between 44 and 45° in the reduced LSTN powders, which corresponds to the (111) facet of metal nickel. To further confirm the metal nickel exsolved from parent LSTN crystal grains, the fabricated LSTN-SDC microtubular substrate was treated in the same reducing conditions. The microstructure was then examined using SEM technique. As shown in Figure 2.6a, nanoparticles with white color were exsolved from grains and uniformly decorated on the surface of the electrode substrate. The nanoparticles along the grain boundaries were relatively large probably due to the coalescing of neighboring smaller nanoparticles (Figure 2.6b). Further EDS analysis indicated that these surface nanoparticles were nickel nanoparticles (Figure 2.6c). The exsolved nickel nanoparticles are expected to significantly improve the surface catalytic property of LSTN phase and therefore that of the porous LSTN-SDC microtubular substrate.

Shown in Figure 2.7a is the cross-sectional SEM image of the fabricated microtubular single cell. Obviously, multilayer microstructures can be clearly seen, consisting of LSTN-SDC thick substrate/thin YSZ electrolyte/thin LSM electrode/thin platinum current collector. The radially well-aligned micro-channels in the substrate were well retained after high temperature sintering process, indicating their excellent thermal stability. The thickness of YSZ electrolyte layer was about 15 μm whilst that of LSM air electrode was about 25 μm. The locally zoom-in SEM image in Figure 2.7b demonstrates that the thin YSZ electrolyte was dense and intimately adhered to both porous LSM electrode and LSTN-SDC substrate. The insert photo in Figure 2.7a shows a fabricated single cell with the diameter of about 2 mm and the length of about 20 mm.

In conventional Ni-cermet electrode supported solid oxide cells, it usually takes a certain period to fully reduce NiO in the electrode to Ni depending on the volume and porosity of substrate electrode. Once fully reduced, a reducing atmosphere is required to protect Ni from being oxidized again. This would complicate the operations of solid oxide cells and cause other issues as mentioned above especially when startup/shutdown or reversible operations are needed to satisfy certain energy conversion requirements. With mixed conducting perovskite fuel electrode designs, e.g., LSTN-SDC fuel electrode, the operating complications associated with Ni-cermet electrode could be overcome. As a result, the reducing and oxidizing atmosphere can be freely switched for the fuel electrode without affecting its functionality. To demonstrate such redox advantages of the LSTN-SDC microtubular substrate-supported cell, the reducing gas CO and air were supplied into the substrate electrode alternatively with nitrogen as the purging gas in between. The LSM electrode was exposed to ambient air. The temperature of the cell was controlled at 850 °C. The history of cell OCVs was monitored and recorded with the elapsed time. As shown in Figure 2.8, when air was supplied to the LSTN-SDC electrode, the OCVs stayed at zero, because the oxygen partial pressure difference across the dense YSZ electrolyte was zero. Once the sweep nitrogen gas was applied, the oxygen partial pressure in the microtubular substrate would be rapidly decreased, resulting in a prompt increase of OCVs. After switching to CO gas, the OCVs experienced a period of transient process and reached a steady state value of about 0.96 V. When the supplied CO gas was switched back to nitrogen gas, followed by applying air again, the OCVs demonstrated fluctuating variations due to oxygen partial pressure changes in the LSTN-SDC electrode and were then back to the steady state value of 0 V. During five non-uniform redox cycling operations, the OCVs

of the cell followed the changes of gas atmosphere in fuel electrode well and did not show any observable degradations. The OCVs of the cell usually reflect its structural integrity in a comprehensive manner. To obtain reasonably high OCVs, the microstructures of the cell should fulfill a set of conditions. The electrolyte should be dense and gas-tight without cracks or holes; the electrolyte should adhere well with electrodes on either side; the porous electrodes should have sufficient triple phase boundaries and allow facile fuel/gas diffusions so that sufficiently high fuel/gas partial pressures can be built at reaction sites in porous electrodes for electrochemical reactions. Any failure of these conditions would lead to abnormally low OCVs. The short-term redox cycling experiment demonstrated that LSTN-SDC microtubular substrate-supported cell was redox stable, and the OCVs of the cell were able to rapidly follow the changes of reducing/oxidizing atmospheres in the LSTN-SDC substrate electrode.

The electrochemical performance of the cell was then measured at 850 °C. The LSM electrode was still exposed to the ambient air whilst pure CO gas was supplied to the LSTN-SDC electrode. The *V-I* curves, and power density curves are shown in Figure 2.9a. When the supplied CO flow rate was 5 $mL \cdot min^{-1}$, the *V-I* curve showed approximately a straight line with a slight down-bending at high current densities. Once the CO flow rate was increased to 15 $mL \cdot min^{-1}$ and 30 $mL \cdot min^{-1}$, the corresponding *V-I* curves demonstrated straight lines. These results indicate that the overall cell resistance did not obviously change with increasing load current especially at high current conditions probably due to the high gas permeability of microtubular substrate mentioned above. With increasing the CO flow rate from 5 $mL \cdot min^{-1}$ to 15 $mL \cdot min^{-1}$ and 30 $mL \cdot min^{-1}$, the corresponding cell peak power density increased from ~ 170 $mW \cdot cm^{-2}$ to ~ 215 $mW \cdot cm^{-2}$ and ~ 250 $mW \cdot cm^{-2}$ respectively.

Figure 2.9b shows the electrochemical impedance spectra (*EIS*) of the cell at OCV conditions under different CO flow rates. It can be seen that the cell ohmic resistance decreased from 0.78 Ω cm^2 to 0.66 Ω cm^2 when the CO flow rate was increased from 5 $mL \cdot min^{-1}$ to 30 $mL \cdot min^{-1}$. The ohmic resistance was contributed by dense YSZ electrolyte layer and the skeletons of both fuel electrode and oxygen electrode. Since only CO flow rate into the fuel electrode was changed, it is reasonable to assume that the decrease of cell ohmic resistance was primarily induced by the skeleton of porous fuel electrode. It is known that LSTN is an *n*-type mixed conductor, which has higher electrical conductivities in the gas environment of lower oxygen partial pressures. The increase of supplied CO flow rate would directly lead to the decrease of oxygen partial pressure in the fuel electrode, and therefore the ohmic resistance of the fuel electrode and the cell. The overall polarization resistance represented by the difference between low frequency intercept and high frequency intercept decreased from ~ 0.46 to ~ 0.29 Ω cm^2 with increasing the CO flow rate from 5 $mL \cdot min^{-1}$ to 30 $mL \cdot min^{-1}$ respectively. Each of the *EIS* curves consists of two arcs, a relatively large high frequency arc associated with charge transport process and a small low frequency arc related to fuel/gas diffusion process. The low frequency arc did not show obvious change while the high frequency arc decreased with increasing CO flow rates. The low frequency arc is closely related to fuel/gas diffusion processes in both fuel and oxygen electrodes. Since gas supply condition at the oxygen electrode did not change, it is reasonable to postulate that the variations of *EIS* curves were mainly induced by fuel electrode conditions. Due to the radially well-aligned microchannels in the substrate, the corresponding gas permeability is very high, leading to the fact that fuel/gas diffusion resistance was low in the substrate and the low frequency arc was not sensitive to the

increase of CO flow rate from 5 mL·min^{-1} to 30 mL·min^{-1}. On the other hand, the increased CO flow rates would reduce oxygen partial pressures in the substrate electrode. Due to the *n*-type nature of LSTN material, the corresponding electrical conductivities of fuel electrode increased. As a consequence, the high frequency arc associated with charge transport process decreased with increasing CO flow rates.

The SOFC and SOEC performances of the microtubular cell were also measured in a coherent way, where the operating temperature was controlled at 850 °C, the oxygen electrode was exposed to the ambient air, while the CO/CO_2 gas mixture with different CO:CO_2 ratios of 2:1, 1:1, and 1:2 was supplied into the substrate electrode respectively. Under each CO:CO_2 ratio, the total flow rate of gas mixture was remained at 30 mL·min^{-1}. When the voltage applied on the cell swept from 0.05 V to 2.0 V, the electrochemical performance of the cell represented by *V-I* curves are shown in Figure 2.10. As one can see, with increasing the CO:CO_2 ratio from 1:2 to 1:1, the SOFC performance of the cell showed significant improvement. Further increasing the CO:CO_2 ratio from 1:1 to 2:1, the SOFC performance of the cell was slightly improved. It is well known that CO was the fuel in the supplied gas mixture and electrochemically oxidized in the fuel electrode through the reaction (2-1) when the cell was operated in SOFC mode,

$$\mathrm{CO} + \mathrm{O}'' \rightarrow \mathrm{CO_2} + 2\mathrm{e}' \qquad (2-1)$$

where O'' is oxygen ion and e' is electron.

The increase of CO:CO_2 ratio in the gas mixture would directly increase CO concentration, and thereby SOFC performance of the cell. As will be shown later on, Boudouard reaction described by (2-2) could also take place,

$$2\mathrm{CO} \leftrightarrow \mathrm{CO_2} + \mathrm{C} \qquad (2-2)$$

When CO concentration in the gas mixture was relatively high, the forward Boudouard reaction occurred, decreasing CO concentration whilst increasing CO_2 concentration. In addition, electrochemical oxidation of CO also generates CO_2 as described by reaction (2-1). Together these in turn would deteriorate SOFC performance of the cell. The combinational effects of different CO:CO_2 ratios in the gas mixture and Boudouard reactions could lead to above behaviors of SOFC performance, where the SOFC performance was not linearly correlated with inlet CO:CO_2 ratios.

As demonstrated above, nickel nanoparticles were uniformly decorated on the inner surface of micro-channels in microtubular substrate, forming a fixed catalyst bed. When CO/CO_2 gas mixture was supplied into the substrate electrode, in addition to Boudouard reaction, another potential reaction that can affect composition and concentration of gases in the substrate electrode is the direct thermal splitting of CO_2 with the aid of surface Ni nanoparticle catalyst,

$$CO_2 \leftrightarrow CO + \frac{1}{2}O_2 \qquad (2-3)$$

To examine the effects of Boudouard reaction and direct CO_2 thermal splitting, the gas mixture of CO and CO_2 was supplied into the substrate electrode under open circuit voltage condition at 850 °C. As a result, the effect of electrochemical reactions can be eliminated. The overall inlet mixed gas flow rate was controlled at 30 mL·min^{-1} at several CO:CO_2 ratios of 2:1, 1:1, and 1:2 respectively. For each of the CO:CO_2 ratios, the corresponding outlet gas compositions from the substrate were measured using the GC. The comparison results of inlet and outlet CO flow rates are shown in Figure 2.11. It is clear to see that the CO outlet flow rates are lower than the CO inlet flow rates in all of the three cases, indicating that Boudouard reaction and/or CO_2 thermal splitting could take

place in the substrate electrode. It was also observed from GC (not shown here) that very tiny oxygen and nitrogen peaks appeared and remained almost the same in the three cases, implying that the oxygen in effluent gases could come from the leakage induced by non-perfect sealing at membrane/supporting tube interface. The GC results further demonstrate that the concentration ratio of O_2:N_2 in the effluent gas was lower than that in air, indicating that part of the leaked oxygen was consumed probably due to the direct burning of CO. Combining these results together, one can see that the CO_2 thermal splitting reaction (3) was less likely to take place, or at least the effect of reaction (2-3) was negligible. Therefore, it is strongly suggested that the composition variations of gas mixture in the substrate electrode was mainly induced by Boudouard reaction. It is easy to understand that high inlet CO:CO_2 ratios would favor the forward Boudouard reaction, reducing outlet CO concentrations as demonstrated above for CO:CO_2 = 2:1 and 1:1. Interestingly, when the inlet CO:CO_2 ratio was reduced to 1:2, the outlet CO flow rate was still less than the inlet CO flow rate, indicating that the forward Boudouard reaction took place. Since carbon is needed for backward Boudouard reaction and the substrate electrode was lack of carbon, this could be the reason that the forward Boudouard reaction occurred even though the CO_2 concentration was relatively high, e.g., CO:CO_2 = 1:2.

At the condition of net zero current density, the cell demonstrated the OCVs in the range of 0.7 V - 0.8 V at different CO:CO_2 ratios. According to the Nernst equation, the OCVs of the cell are mainly dependent on the operating temperature and partial pressures of oxygen and gas species (i.e., CO, CO_2) at the shell electrode and substrate electrode side respectively. Since the operating temperature and oxygen partial pressure at the shell electrode remained unchanged, the slight variations of OCVs were mainly attributed to the

changes of CO and CO_2 partial pressures in the substrate electrode. The CO partial pressure was determined by the combinational effects of supplied gas mixture and Boudouard reactions. Even though the CO content in the supplied gas mixture increased and thereby CO partial pressures, the increased CO content could enhance the forward Boudouard reaction, which in turn decreased CO content and increased CO_2 content. This could be the reason that a large change of CO:CO_2 ratios in the supplied gas mixture only resulted in slight variations of OCVs.

When the applied cell voltages were beyond OCVs, the cell entered into the operations of SOEC mode. For a given applied voltage, the corresponding current density increased with increasing the CO:CO_2 ratios in the feeding fuel, and thereby SOEC performance. The slopes of the *V-I* curves demonstrated two obvious regions: the nonlinear region below the voltage of approximately 1.4 V and the linear region above 1.4 V. The SOEC performance was affected by both polarization resistance and ohmic resistance of the cell. At relatively low current density conditions, e.g., below the applied voltage of 1.4 V, ohmic resistance loss was relatively low and polarization resistance loss dominated the overall resistance loss of the cell. Accordingly, the *V-I* curves demonstrated nonlinear behavior in this region. At relatively high current density conditions, e.g., above 1.4 V, the overall cell resistance loss was dominated by the ohmic resistance loss, therefore *V-I* curves showed approximately linear behaviors. It is noteworthy that the CO_2 is the fuel for the cell in the SOEC mode. In principle, increasing CO_2 concentration in the substrate electrode would improve SOEC performance. Interestingly, with increasing CO:CO_2 ratios in the feeding fuel from 1:2 to 1:1 and 2:1, and thereby decreasing CO_2 concentrations, the SOEC performance was actually improved. It should be admitted that increasing CO:CO_2 ratio

favored the forward Boudouard reaction, resulting in the increase of CO_2 content. But the corresponding increase of CO_2 concentration could be partially offset by the effect of increased $CO:CO_2$ ratios. As mentioned above, LSTN is an *n*-type mixed conductor. Increasing $CO:CO_2$ ratios in the feeding fuel would directly decreasing oxygen partial pressures in the substrate, thereby increasing its electrical conductivities. It might also increase the surface oxygen vacancies of LSTN and therefore surface exchange property. These complicated combinational effects led to the increased SOEC performance under higher $CO:CO_2$ ratios.

In order to study polarization performance of the cell at different operating conditions, the *EIS* were measured at different applied cell voltages under both SOFC mode and SOEC mode. The results are shown in Figure 2.12. The overall polarization resistances of the cell were extracted from *EIS* curves and the correlations between the applied cell voltages and overall polarization resistances under different $CO:CO_2$ ratios in the feeding fuel are shown in Figure 2.13. For a given $CO:CO_2$ ratio in the feeding fuel, the overall cell polarization resistance slightly decreased with increasing cell potentials from 0.2 V to 0.4 V, 0.6 V, and 0.8 V, which were primarily the operations of SOFC mode. When the applied cell voltage increased from 0.8 V to 1.4 V, and therefore the SOFC mode was switched to SOEC mode, the overall polarization resistance demonstrated significant increase. Beyond 1.4 V, the overall polarization resistance decreased significantly with increasing applied cell voltages. One also can see that $CO:CO_2$ ratios in the feeding fuel affected polarization resistances of the cell in different degrees at different operating conditions. In the SOFC mode, or approximately below 0.8 V of the cell potentials, the cell polarization resistance decreased with increasing $CO:CO_2$ ratios in the feeding fuels. Since the gas composition at

the oxygen electrode side did not change, the variation of polarization resistance was primarily induced by the change of gas compositions in the substrate electrode. As mentioned above, LSTN is an *n*-type mixed conductor at low oxygen partial pressure conditions. Higher $CO:CO_2$ ratio and therefore lower oxygen partial pressure would produce more oxygen vacancies both at the surface and in the bulk of substrate electrode. Accordingly, surface exchange property and electrical conductivity of the substrate electrode were improved, and cell polarization resistance was decreased. Under the SOEC mode, i.e., beyond 1.4 V, the CO_2 in the feeding gas is the fuel. Although the electrochemical kinetic properties of LSTN electrode were improved with increasing $CO:CO_2$ ratios, it also diluted CO_2 concentrations in the feeding fuel. The combination of these two competing factors caused very complicated effects on cell polarization resistance. In particular, when $CO:CO_2$ ratio increased from 1:2 to 1:1, the variation of cell polarization resistance was negligible, probably because the effect on the improvement of LSTN electrochemical kinetic properties was comparable to that on CO_2 dilution. Further increasing $CO:CO_2$ ratio from 1:1 to 2:1, the cell polarization resistance was decreased a little bit, possibly because the effect from the former exceeded the latter.

The short-term CO_2 electrolysis performance of the cell was further studied. The operating temperature was kept at 850 °C, the oxygen electrode was still exposed to the ambient air while the gas mixture with $CO:CO_2$ =15 $mL \cdot min^{-1}$:15 $mL \cdot min^{-1}$ was supplied into the substrate electrode. A series of step-change voltages were applied on the cell. The cell was initially at open circuit voltage condition. A voltage of 1.4 V was then applied to the cell and lasted for 1 h. The applied voltage was then step-changed to 1.6 V and 2.0 V respectively and the duration time of each applied voltage was 1 h. The time history of the

corresponding cell current density was measured and the compositions of effluent gases from substrate electrode were analyzed by an on-line gas chromatograph. As shown in Figure 2.14a, after the cell voltage was step-changed from OCV to 1.4 V, the cell current density experienced a transient process towards a steady state value due to the dynamic behavior of multi-physicochemical processes in a solid oxide electrochemical system. [109] Depending on the step-change magnitude of the applied voltages, e.g., 1.4 V, 1.6 V, and 2.0 V, the responses of the corresponding transient process were also slightly different. Compared to electrolyte-supported cells that have very thin fuel electrode layers, the fuel electrode-supported cells have relatively thick LSTN-SDC electrode. Due to oxygen release/incorporation capability of mixed conducting LSTN, it would take relatively longer time for the bulk mixed conducting LSTN electrode to reach a new equilibrium when the applied voltage on the cell was subject to a step change from one value to another.[110] This could be another reason that causes relatively long transient process of the cell current density shown in Figure 2.14a.

During CO_2 electrolysis test under a series of step-change voltages, the CO content in the effluent gases from the substrate electrode was measured every 0.5 h and also shown in Figure 2.14a. The right vertical axis in Figure 2.14a represents the net CO production rate generated by the cell, which was obtained by subtracting the inlet CO flow rate from the outlet CO flow rate. It can be seen that the net CO production rate from fuel electrode kept increasing with the testing time. Since the applied voltages on the cell were step-changed in an increasing way, the corresponding cell currents were also increased. Accordingly, the CO production rate was enhanced according to Faraday conservation law. Within the range of each applied constant voltage, the CO production rate was also

increased with the testing time due to the fact that the cell was experiencing a transient process, so did the net CO production rate. The theoretical CO production rates were also calculated using Faraday's charge conservation law and compared with the practical CO production rates. It is interesting to see from Figure 2.14b that the measured net CO production rate was higher than the theoretical one at every concerned operating condition. Accordingly, the conversion efficiencies from CO_2 to CO were higher than 100% as shown in Figure 2.14b. This result implies that a catalytic process other than electrolysis process should exist in the substrate electrode, converting CO_2 into CO. The Boudouard reaction has been experimentally verified above, contributing to the conversions between CO and CO_2 in the substrate electrode. However, too much CO content in the substrate would drive the reaction towards producing more CO_2 whilst reducing the CO content. Therefore, in addition to Boudouard reaction, surface catalytic processes would exist, enhancing the CO production from CO_2. As demonstrated above, the LSTN-SDC microtubular electrode substrate is embedded with radially aligned micro-channels and the inner surfaces of micro-channels are uniformly decorated with nickel nanoparticles. The substrate electrode with these features forms a fixed catalyst bed, in which both surface nanoparticles and surface oxygen vacancies of LSTN phase would provide catalytic functions. The extra CO produced by the cell beyond the capacity of electrolysis process could be induced by surface catalytic processes occurred in substrate catalyst bed. Accordingly, the following surface catalytic processes, converting CO_2 into CO, are suggested in Kroger-Vink notation,

$$\mathrm{CO_2(g) + Ni \rightarrow NiO + CO(g)} \qquad (2-4)$$

$$\mathrm{CO_2(g) + 2e' + V_O^{\cdot\cdot} \rightarrow CO(g) + O_O^{\times}} \qquad (2-5)$$

where the main symbol e is the electron, O the oxygen, V the vacancy; superscript indicates relative charge with $' = \text{negative}$, $\cdot = \text{positive}$, and $\times = \text{neutral}$; subscript indicate lattice site with $\text{o} = \text{oxygen site}$; $\text{g} = \text{gas phase}$; other symbols are self-explained. In the reaction (2-4), CO_2 oxidizes surface Ni nanoparticles whilst being reduced to CO. In the reaction (2-5), CO_2 is reduced to CO with the catalytic activity of surface oxygen vacancies of LSTN phase. As shown in Figure 2.14b, depending on the applied cell voltages, the conversion efficiencies were also different. For instance, the conversion efficiencies reached up to 250% and 350% under the voltages of 1.4 V and 1.6 V respectively. It has been experimentally demonstrated above that under open circuit voltage condition, the outlet CO flow rate was less than the inlet CO flow rate and the forward Boudouard reaction was the primary reaction in the substrate electrode. Together these observations seem indicate that the surface catalytic activities are closely related to the electrolysis process. Since the applied cell voltage higher than the OCVs would drive charge transport processes in the material skeleton of substrate electrode, the higher the voltage the stronger the charge transport processes, it is reasonable to postulate that the enhanced sustainable surface catalytic properties of substrate electrode are closely related to the charge transport processes. Therefore, the following regenerative reactions for surface catalysis are suggested in Kroger-Vink notation,

$$\text{NiO} + 2\text{e}' \rightarrow \text{Ni} + \text{O}'' \qquad (2-6)$$

$$\text{O}_\text{O}^\times \rightarrow \text{V}_\text{O}^{\cdot\cdot} + \text{O}'' \qquad (2-7)$$

Both surface Ni nanoparticles and surface oxygen vacancies of LSTN phase are regenerated through electro-reduction reactions of (6) and (7) respectively. The regenerated surface catalytic properties would contribute to both electrolysis process and surface

catalytic processes. Accordingly, the CO production rate was beyond the capacity of electrolysis process. While the fundamental mechanisms are worthy to be further studied, it is well demonstrated that the LSTN-SDC supported microtubular cell with nanostructured-substrate electrode is highly efficient for CO production from CO_2.

The dynamic performance of the LSTN-SDC substrate-supported microtubular cell LSTN-SDC/YSZ/LSM was further investigated under SOFC-SOEC reversible operating mode. The operating temperature was kept at 850 °C. The LSM electrode was exposed to the ambient air while the gas mixture with $CO:CO_2$ =15 $mL \cdot min^{-1}$: 15 $mL \cdot min^{-1}$ was supplied into the substrate electrode. The cell was operated in SOFC mode for 2 h followed by the operation in SOEC mode for 1 h. Such an operating cycle pattern was repeated for five times. In the SOFC mode, the voltage of 0.4 V was applied to the cell, which corresponded approximately to the peak power density output of the cell. In the SOEC mode, the voltage of 1.6 V was applied to the cell. Initially, the cell was in the equilibrium state of open circuit voltage. During the reversible operations, the responses of cell current density history were measured and shown in Figure 2.15. It can be seen that the current density experienced a period of significant fluctuations after the cell voltage was switched from open circuit voltage to 0.4 V. Other than this significant fluctuation period, the cell current density demonstrated a transient process toward a new equilibrium after every step change of the applied voltages. It seems that the cell in the SOEC mode tended to reach a new steady state faster than that in the SOFC mode. This could be related to different properties of oxygen incorporation and release of LSTN-SDC substrate electrode. While the fundamental mechanisms associated with such different behaviors are worth to be

further studied, no obvious degradations were observed after five reversible cycles, and the reversible performance of the cell was very stable.

2.4 Conclusion

The LSTN-SDC microtubular substrates were successfully fabricated using an in-house built spinneret extrusion system in combination with modified phase inversion method, featuring radially-well aligned micro-channels open at the inner surface of the substrate. The diameters of the micro-channels near the shell side were relatively small but their densities were relatively high. The micro-tubular substrates with such microstructures demonstrated both excellent thermal stability and very high gas permeability. Upon fabrication of LSTN-SDC substrates, the fuel electrode-supported microtubular cell LSTN-SDC/YSZ/LSM was successfully fabricated, where the dense thin film YSZ electrolyte layer with the thickness of ~ 15 μm and the thin porous LSM oxygen electrode with the thickness of ~ 25 μm were obtained. Ni nanoparticles were exsolved from LSTN grains and uniformly decorated onto the surface of LSTN grains, and therefore the inner surface of micro-channels of the substrate after exposing to a reducing atmosphere at elevated temperatures.

The OCVs of the microtubular cell were able to rapidly follow the atmospheric changes in the substrate electrode between the reducing (CO) and oxidizing (air) gas, demonstrating redox stability advantages of Ni-nanoparticles decorated mixed conducting LSTN-SDC electrode over conventional Ni-cermet electrodes. The peak power density of 250 $mW \cdot cm^{-2}$ was obtained at 850 °C with ambient air as the oxidant at the shell side and pure CO as the fuel supplied into the substrate at the flow rate of 30 $mL \cdot min^{-1}$. Approximately linear *V-I* curves in SOFC mode implies the advantages of radially well-

aligned micro-channels in the substrate for facile fuel/gas diffusion. The current density responses of the cell were able to rapidly follow the step-changes of applied voltages in both SOEC mode and reversible mode. Due to the dynamic behaviors of complicated multi-physicochemical processes and the property of oxygen release/incorporation in the thick mixed conducting LSTN-SDC substrate electrode, it usually took relatively long time for the cell to reach a new equilibrium after a step-change voltage was applied, demonstrating conversion-storage characteristics. The electrolysis process in combination with fixed catalytic bed of nanostructured substrate electrode led to a highly efficient device for CO production from CO_2. The electrolysis process tended to regenerate and enhance surface catalytic properties of substrate electrode, resulting in the conversion efficiency of well above 100%. In reversible operating conditions, the cell tended to reach a new equilibrium state faster in the SOEC mode than that in the SOFC mode. The electrochemical performance of the cell was very stable after a few cycles of reversible operations. No obvious degradations were observed.

Table 2-1 Composition of the anode substrate extrusion slurry (wt.%)

NMP	PESf	PVP	LSTN-SDC	Graphite
25.52	5.1	0.73	63.65	5

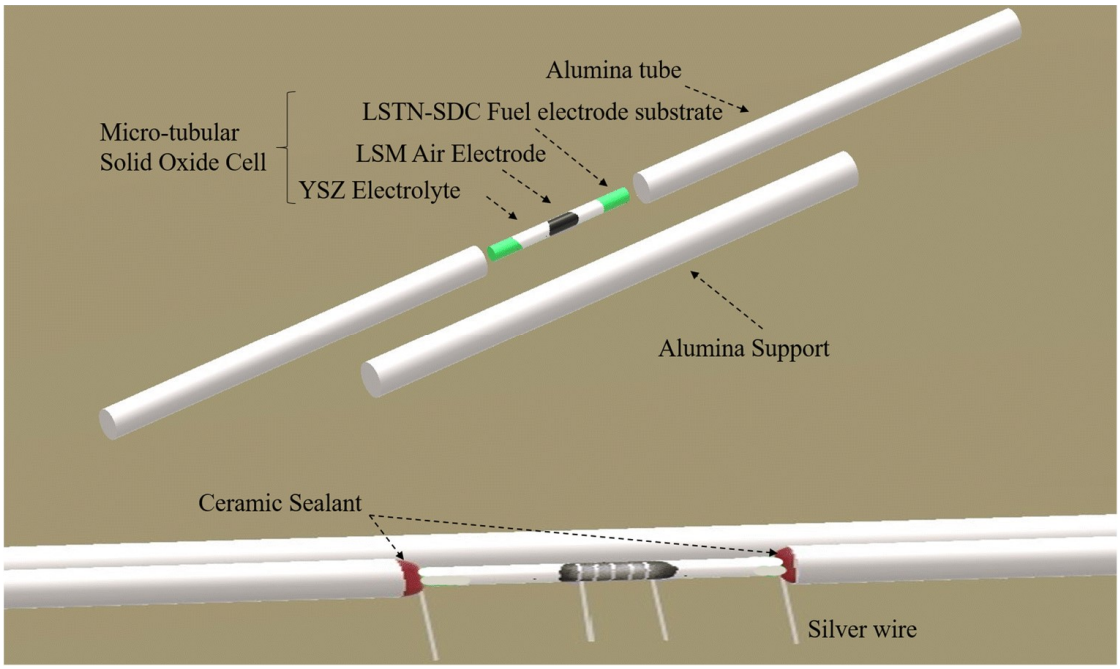

Figure 2.1 Schematic illustration of testing system for microtubular solid oxide cells. **Bottom**: test system assembly; **top**: exploded view.

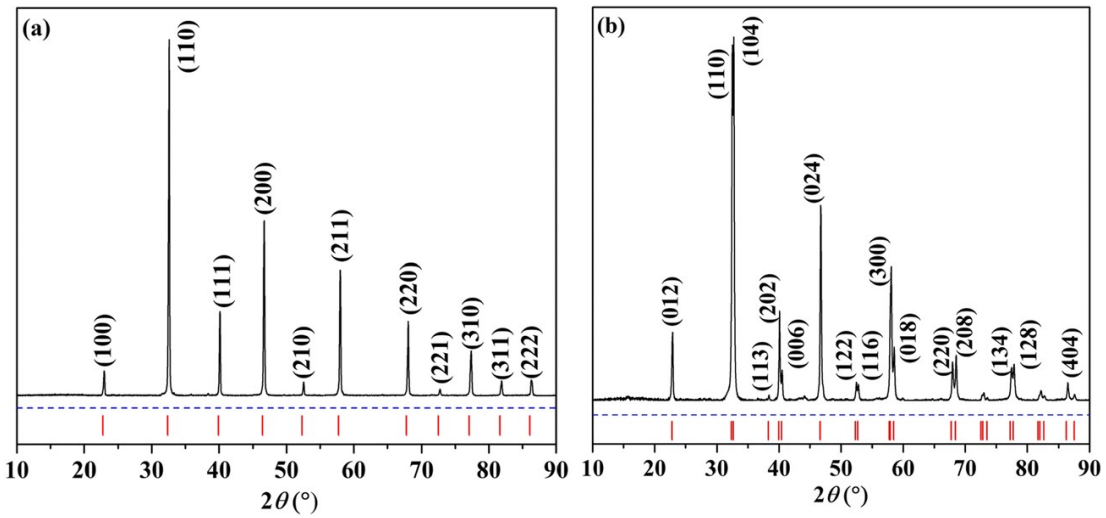

Figure 2.2 XRD patterns of synthesized powders. **a)** LSTN. **b)** LSM.

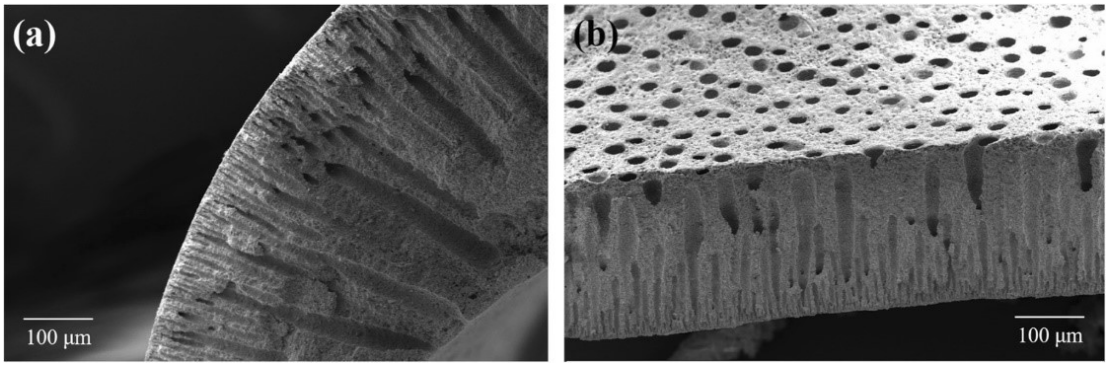

Figure 2.3 SEM images of the as-prepared LSTN-SDC microtubular electrode substrate. **a)** Cross sectional view. **b)** Inner surface view.

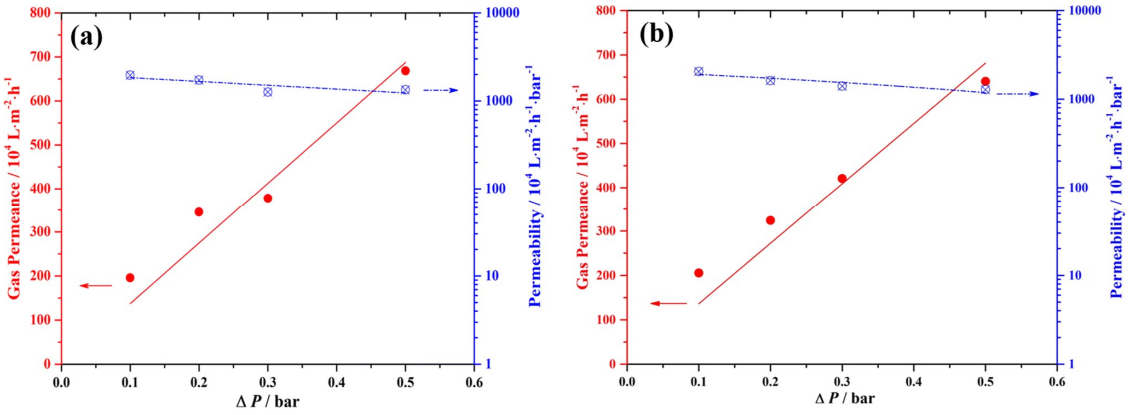

Figure 2.4 Gas permeability of the as-prepared LSTN-SDC microtubular substrate. **a)** Before reducing treatment. **b)** After reducing treatment.

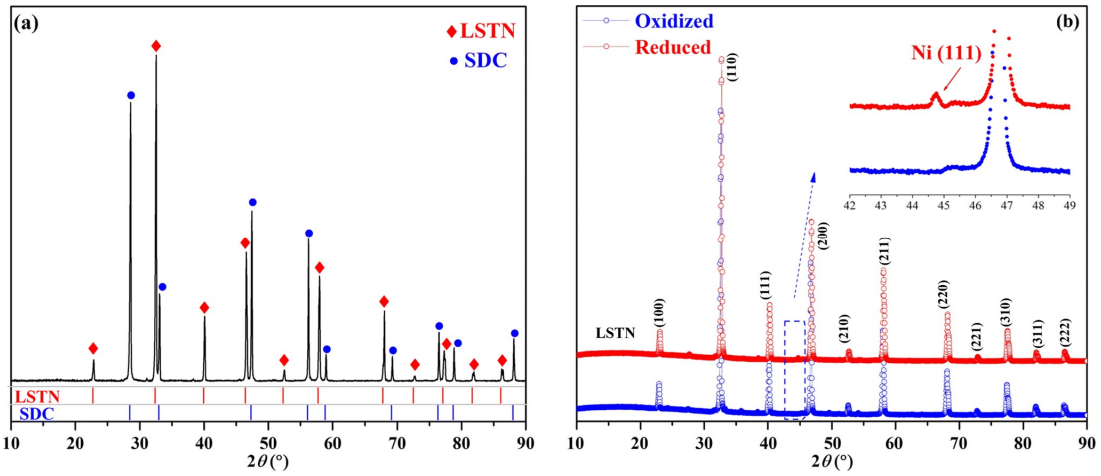

Figure 2.5 **a)** XRD patterns of the composite LSTN-SDC after sintered at 1400 °C in air for 5 h. **b)** XRD patterns of the synthesized LSTN powders before and after reducing treatment.

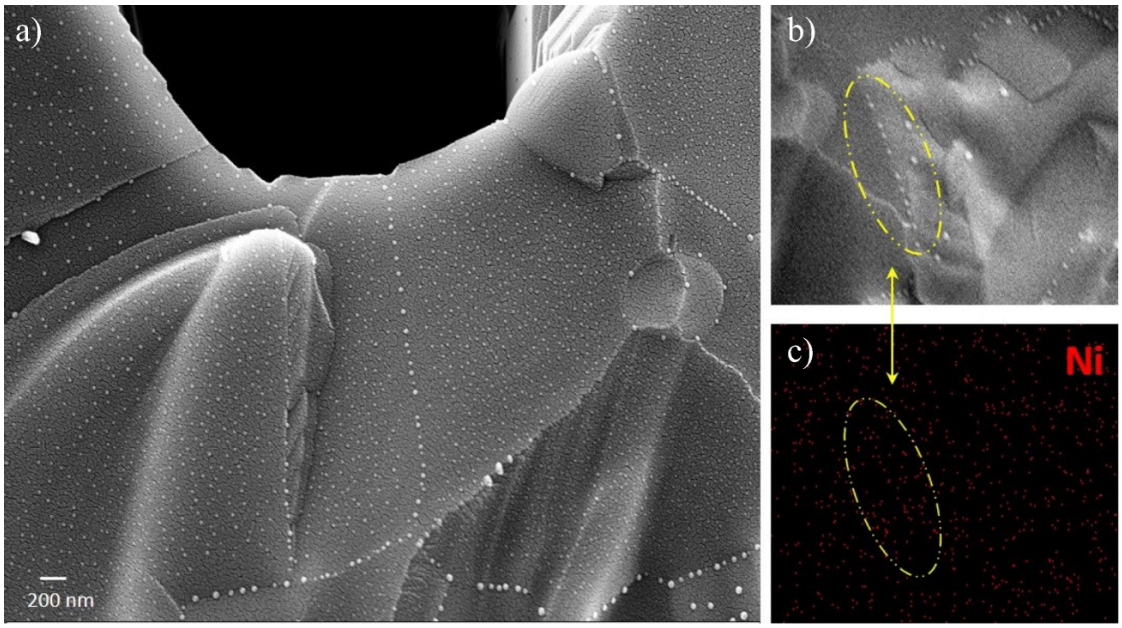

Figure 2.6 **a)** Porous surface SEM image of as-prepared LSTN-SDC microtubular substrate after reducing treatment. **b)** Locally enlarged SEM image. **c)** Mapping of exsolved surface Ni nanoparticle distribution.

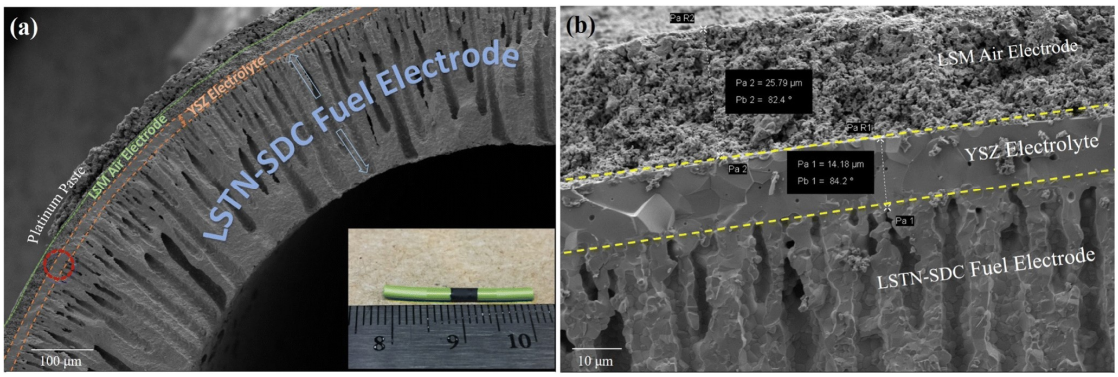

Figure 2.7 **a)** SEM cross-sectional image of as-prepared fuel-electrode-supported microtubular solid oxide cell; the insert is the picture of a fabricated single cell. **b)** Enlarged SEM image of local area marked with the red circle in **a)**.

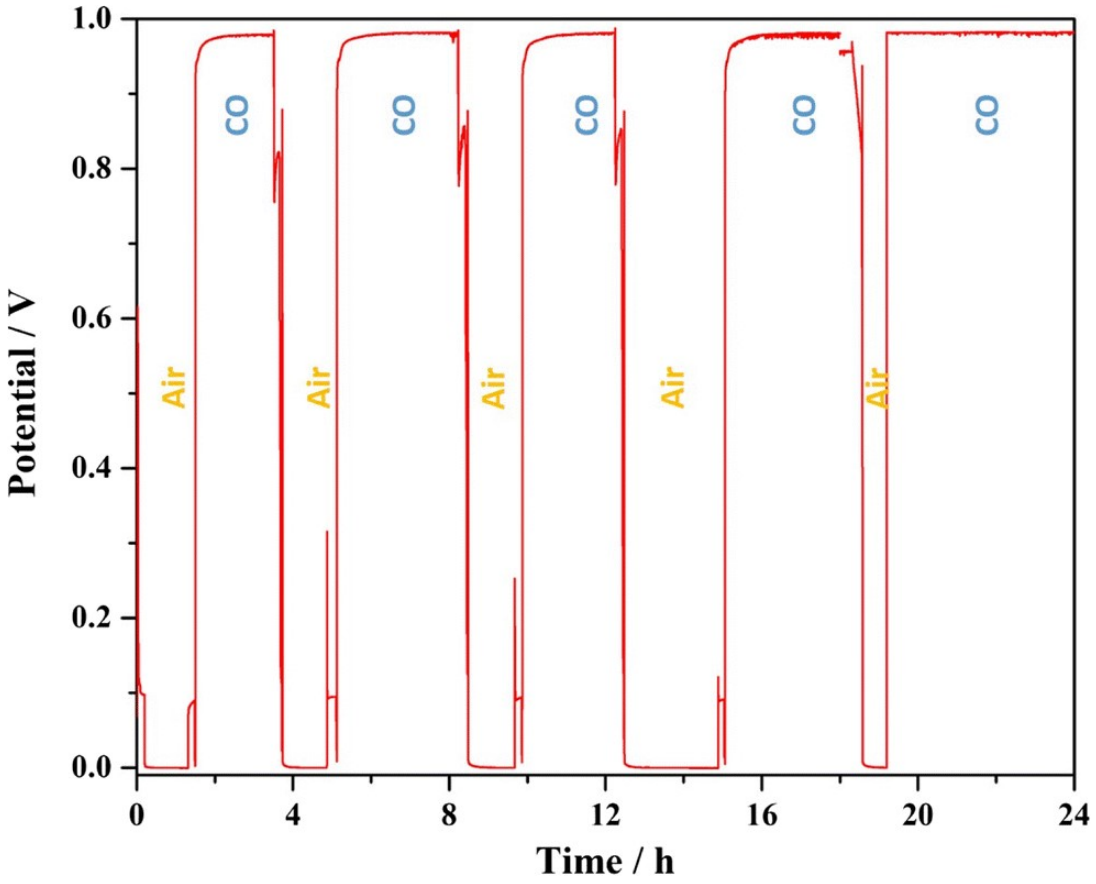

Figure 2.8 Time history of open-circuit voltage of the LSTN-SDC-supported solid oxide cell at 850 °C when air and CO were supplied to the fuel electrode alternatively.

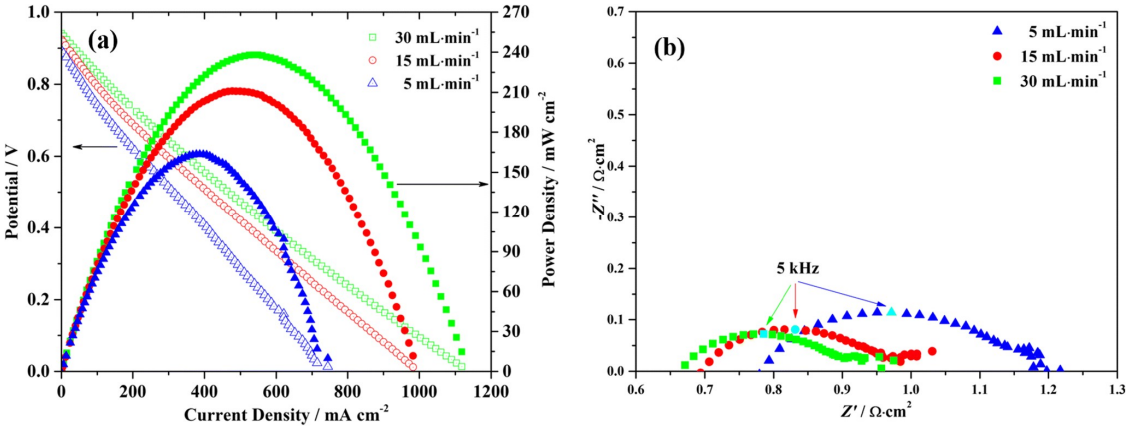

Figure 2.9 **a)** V-I curves and power density curves at different CO feeding rates under 850 °C. **b)** Corresponding EIS curves at open-circuit voltage conditions.

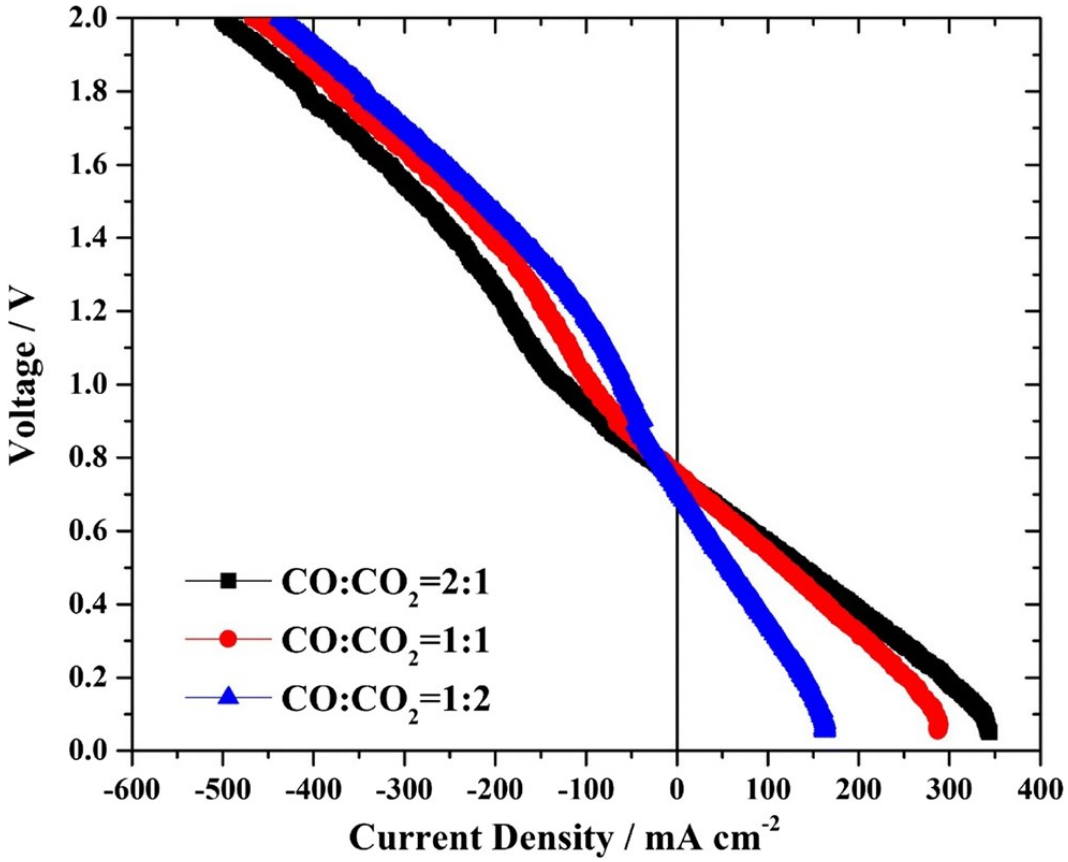

Figure 2.10 V-I curves under both SOFC mode and SOEC mode of the microtubular cell fed with 30 mL·min^{-1} mixture gas of CO and CO_2 at different ratios under 850 °C.

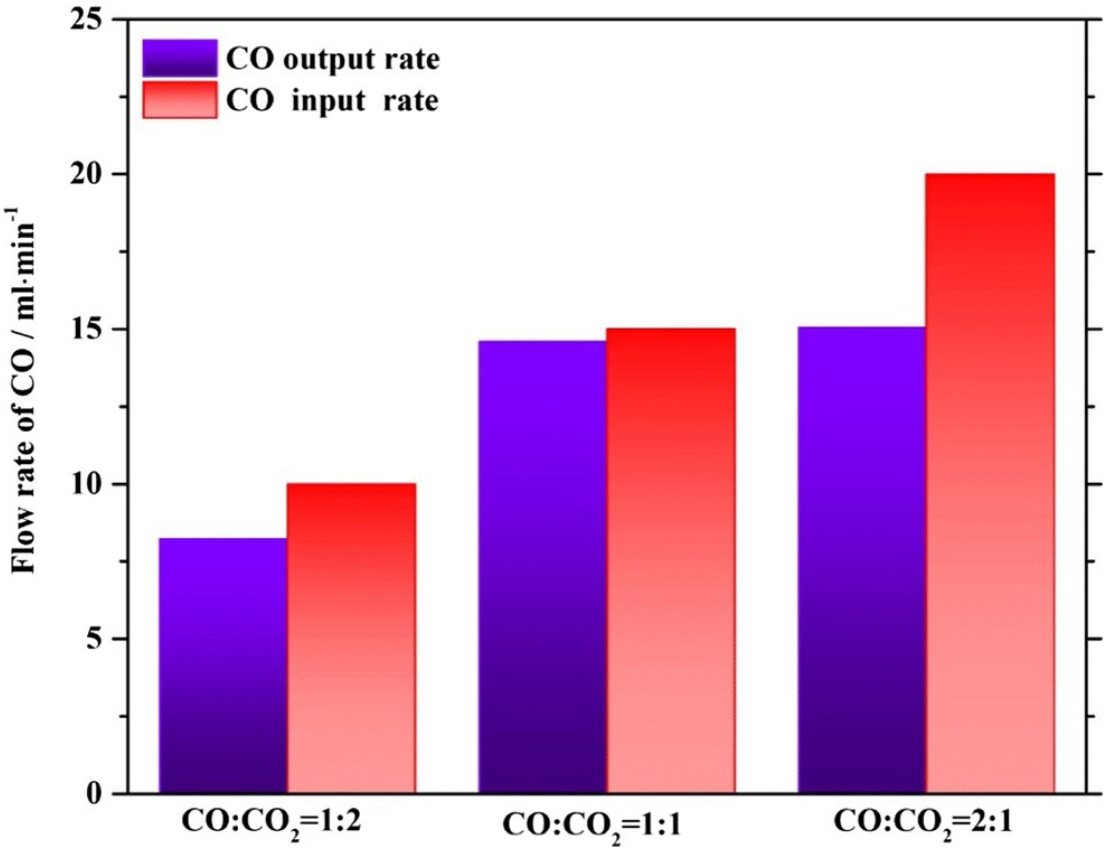

Figure 2.11 Comparisons of inlet and outlet CO flow rates of substrate electrode under different inlet CO/CO_2 ratios when the cell is operated at 850 °C under open-circuit voltage conditions.

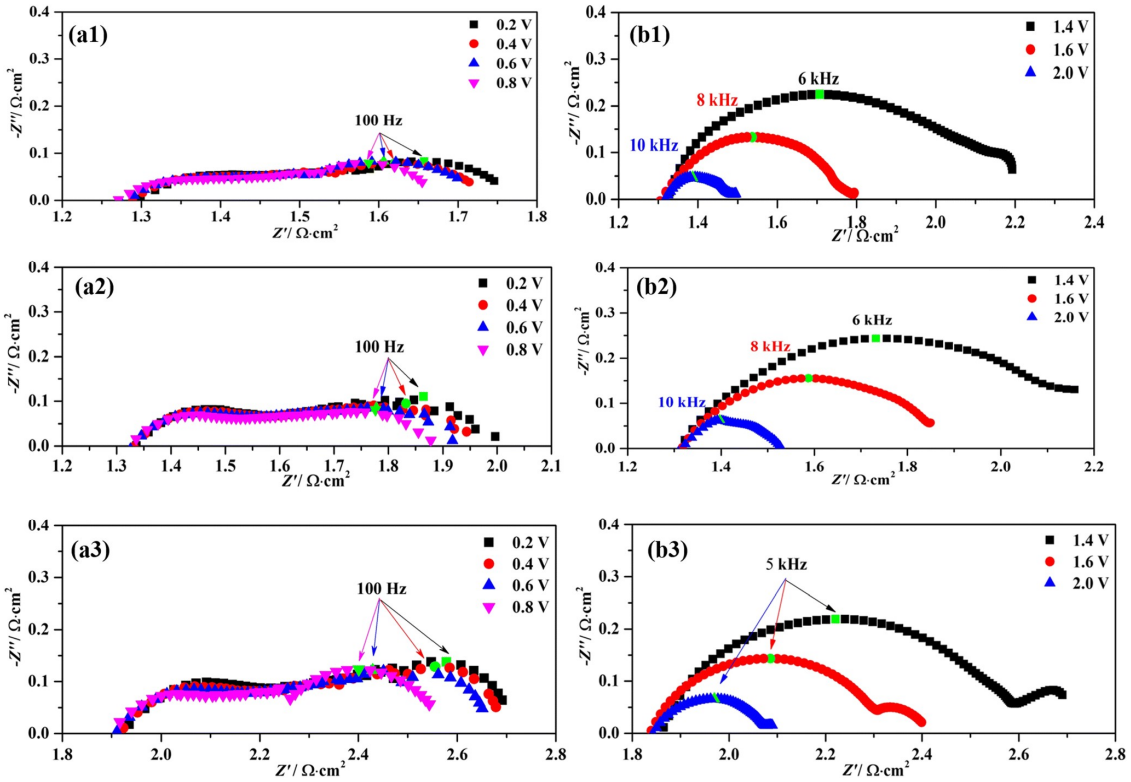

Figure 2.12 EIS of LSTN-SDC-supported microtubular cells at different applied voltages under mixture fuel feeding flow rate of 30 mL·min^{-1} at different CO:CO_2 ratios under 850 °C. **a1, b1** CO:CO_2 = 2:1. **a2, b2** CO:CO_2 = 1:1. **a3, b3** CO:CO_2 = 1:2

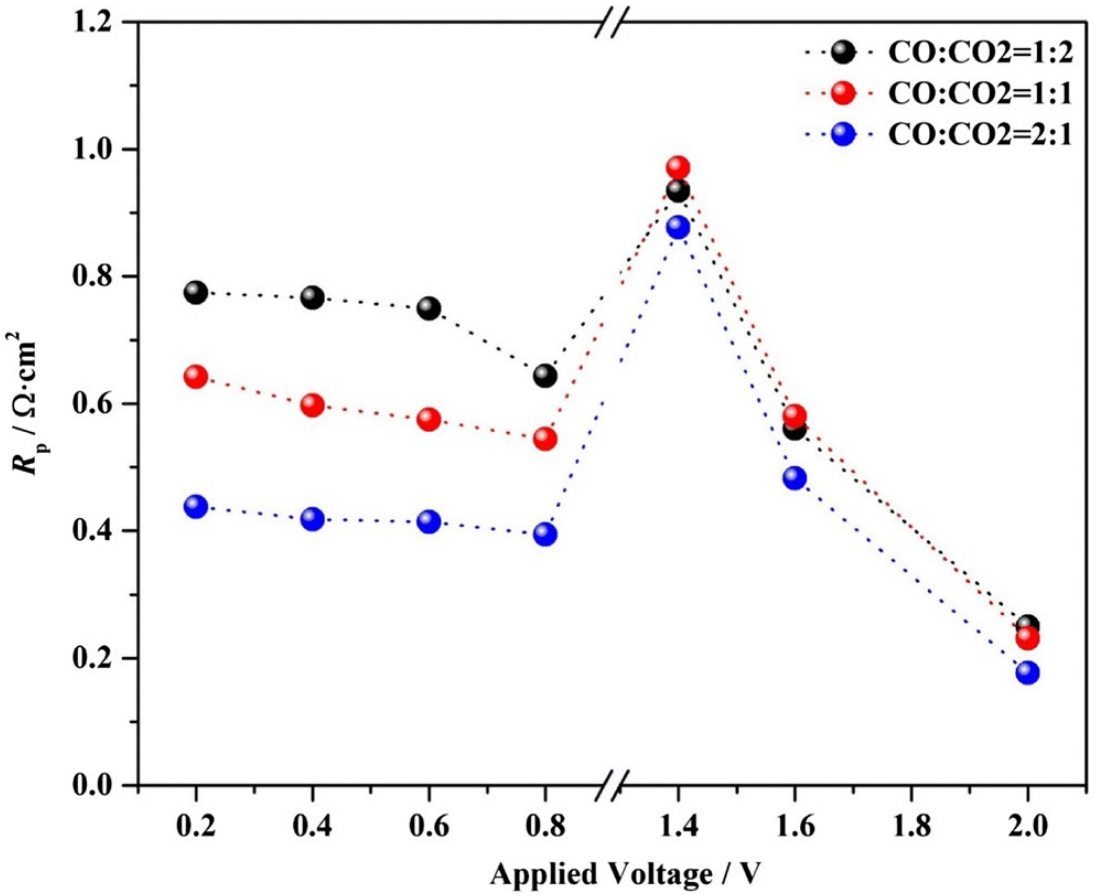

Figure 2.13 Overall cell polarization resistance vs applied voltage at different CO:CO_2 ratios under 850 °C.

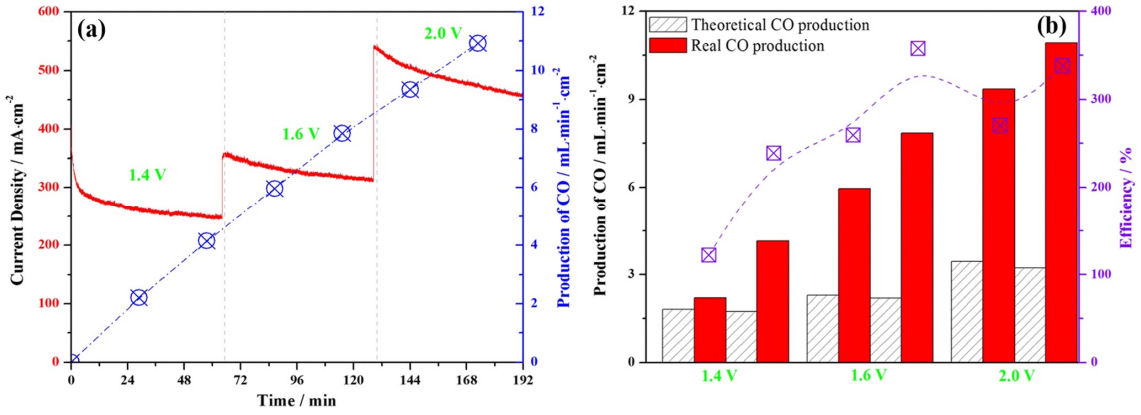

Figure 2.14 Dynamic electrolysis performance of the microtubular cell fed with gas mixture with $CO:CO_2 = 15:15$ mL·min^{-1} and subject to a series of step changes of the applied voltages at 850 °C. **a)** Current density history and CO production rate. **b)** Conversion efficiency.

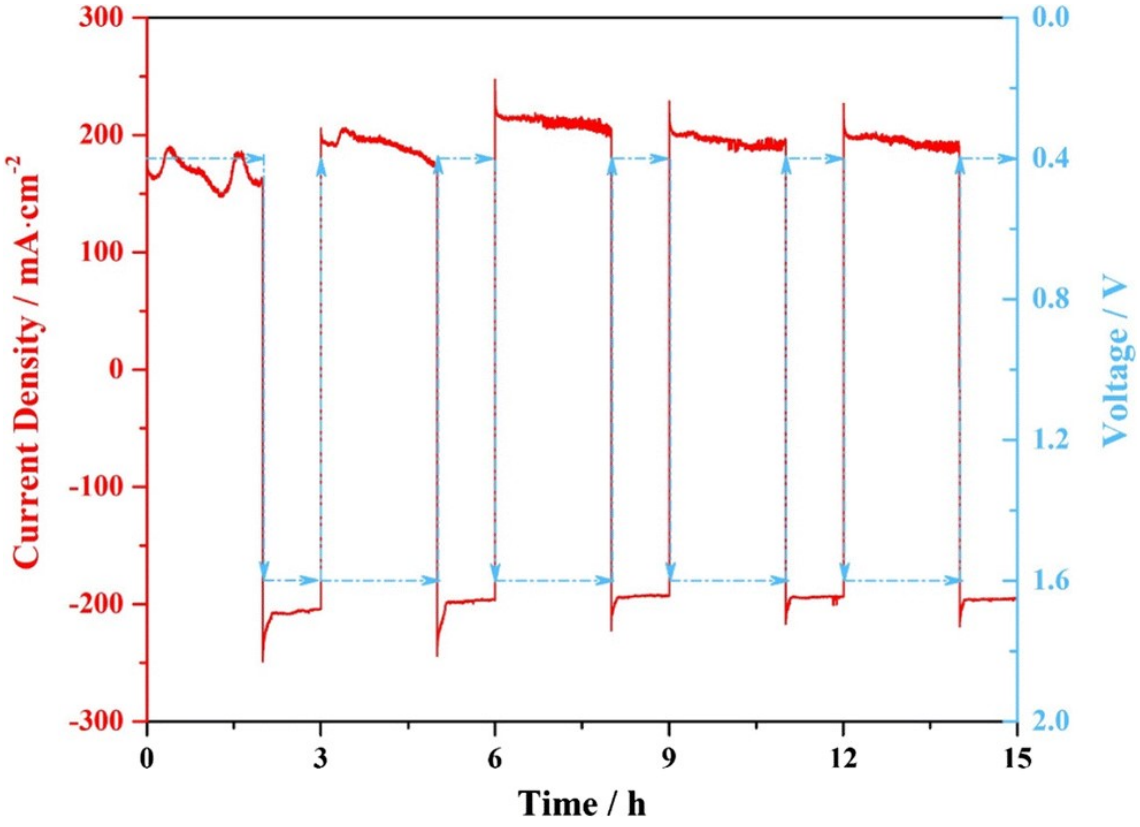

Figure 2.15 Current density history of the microtubular cell under reversible SOFC-SOEC operating conditions when subject to step changes of applied voltages at 850 °C.

CHAPTER 3

FABRICATION AND CHARACTERIZATION OF ROBUST AND DURABLE ASYMMETRIC THIN FILM OXYGEN SEPARATION MEMBRANE BASED ON LSCF-ZnO COMPOSITE HOLLOW FIBER

3.1 introduction

Oxygen is one of the most important chemicals, demonstrating wide applications in modern industries.[111-114] A few technologies have been developed to produce oxygen in industry, including cryogenic distillation, swing adsorption, redox process of metal oxides, and electrochemical oxygen separation membranes. Among these technologies, oxygen separation membrane stands out as a simple and cost-effective technology for highly pure oxygen production from air.[6, 9, 115-117] Oxygen separation membrane technology employs mixed ionic and electronic conducting (MIEC) ceramic materials to separate air for oxygen production. The separation process is driven by oxygen partial pressure gradient across a gas-tight membrane at elevated temperatures. Specifically, at the feed (oxygen rich) side, air is supplied and oxygen molecules are adsorbed onto the membrane surface, where oxygen molecule combines with electrons from the permeate (oxygen lean) side, thereby being reduced to oxygen ion (O^{2-}). The generated oxygen ion jumps into oxygen vacancy in dense membrane and migrates to the permeate side. At the permeate side, oxygen ion is oxidized to form gas oxygen molecule and release electrons. The released electrons at the permeate side then transport back to the feed side through the

membrane, forming a closed-circuit loop within the membrane. As long as a gradient of oxygen chemical potential is imposed across gas-tight dense membrane at elevated temperatures, oxygen is continuously permeated from oxygen rich side to lean side and released downstream without the need of electrodes and external electrical loadings.

Planar and tubular designs are widely used membrane configurations. The planar design has good manufacturability but requires relatively long sealing length, therefore imposing great difficulties on practical applications. The tubular design demonstrates advantages of short sealing length and good thermal shock resistance, especially micro-tubular membrane may effectively increase volumetric density of oxygen permeation. However, the tubular design also imposes challenges on manufacturing process, particularly the microtubular type, where the diameter is relatively small. In the past few years, the slurry spinneret technology in combination with phase inversion method has been successfully developed to fabricate hollow fiber membranes.[57, 67, 118-120] The early-stage hollow fiber membrane usually employs homogeneous material and tap water is used at both inner and outer of spinneret head to form green hollow fibers. The following one-step high temperature sintering process leads to gas-tight hollow fiber membrane. The resultant hollow fiber membrane demonstrates the feature of multiple-layered microstructures. When a cross-section perpendicular to the longitudinal direction is observed, a sponge-like layer in the middle is sandwiched by radially aligned finger-like pore layer on either side, and the shell and lumen sides are covered by relatively dense thin skin layers (Figure 3.1a). Depending on the specific spinneret process, only one finger-like pore layer could also occur, and the pore layer could be close to the shell side (Figure 3.1b) or the lumen side (Figure 3.1c). Although gas-tight membrane can be obtained by one-step

sintering process on these green hollow fiber samples, the sintering temperature is usually very high. For example, a sintering temperature of 1400 °C was needed to fabricate gas-tight $La_{0.6}Sr_{0.4}Co_{0.2}Fe_{0.8}O_{3-\delta}$ (LSCF) hollow fiber membrane.[121] The high temperature usually causes non-uniform sintering effect on green hollow fiber samples. In particular, the outer skin layer of the hollow fibers was usually over-sintered, however, the sponge-like layer and finger-like pore layer were under-sintered and could not be fully densified. This left the closed finger-like pores in the bulk of the membrane, which in turn causes two disadvantages. On one hand, the closed finger-like pores decrease the equivalent bulk conductivity of the membrane and therefore its permeation performance; due to their closed nature, they could induce extra steps of oxygen reduction reaction (ORR) and oxygen evolution reaction (OER) within the bulk, decreasing the membrane efficiency for oxygen separation process. The high sintering temperature could also produce sulfate impurities in the membrane, deteriorating its oxygen permeation performance.[122] Recently, solvent concentration gradient was applied to fabrication process by using tap water and the mixture of tap water and solvent as coagulants at inner and outer surface of green hollow fiber precursor respectively. As a result, the solvent/nonsolvent exchange rate at the inner surface was different from the outer, and radially aligned finger-like pores open at the inner surface were able to be created (Figure 3.1d).[123] While the open finger-like pores facilitate facile gas diffusion, very high sintering temperature is needed in order to obtain gas-tight membrane. To take advantage of open finger-like pores while reducing the sintering temperature, our group has recently developed an asymmetric hollow fiber membrane, where a thin dense separation layer is supported by such a microchannel-structured substrate.[89] Compared to the hollow fiber membrane fabricated by one-step extrusion and

one-step sintering process mentioned above, the fabrication of the asymmetric hollow fiber membrane requires one extra steps of separation layer coating. However, a relatively lower sintering temperature is sufficient to obtain gas-tight membrane by only densifying the thin film separation layer while keeping the microstructures of the substrate. For instance, for the hollow fiber membrane $Gd_{0.2}Ce_{0.8}O_{2-\delta}$-$La_{0.6}Sr_{0.4}Co_{0.2}Fe_{0.8}O_{3-\delta}$ (GDC-LSCF) substrate/GDC-LSCF composite thin film separation layer, the sintering temperature of 1300 °C is sufficient to densify the thin film separation layer and obtain gas-tight hollow fiber membrane.[124] The asymmetric membrane may also provide other advantages. In particular, the thin film dense separation layer may significantly reduce the bulk ohmic resistance for charge transport while the radially well-aligned open microchannels in the substrate can obviously improve the property for gas diffusion. Unfortunately, the mechanical strength of the hollow fiber membranes is generally not sufficient for robust and durable operations. The strategy through composite may improve the strength but could deteriorate charge transport property especially for none-conducting phases in the membranes. The asymmetric membrane design may overcome this issue by using composite substrate to improve the strength without affecting thin film dense separation layer.

In this research, a new composite hollow fiber substrate and substrate-supported asymmetric hollow fiber membrane were studied to improve its mechanical strength and stability. In particular, ZnO was used to form ZnO-LSCF composite substrate. The ZnO content was optimized so that the radially well-aligned microchannels open at the inner surface of the substrate were created meanwhile the robustness and durability of the membrane were also significantly improved. Built upon the microchannel-structured ZnO-

LSCF composite substrate, a dense LSCF thin film was fabricated to form an asymmetric hollow fiber membrane ZnO-LSCF substrate/LSCF. A thin porous LSCF catalyst layer was then coated to form the membrane ZnO-LSCF substrate/LSCF/porous LSCF. The ZnO addition in the substrate may reduce sintering temperature down to 1270 °C for gas-tight asymmetric membrane LSCF-ZnO/LSCF fabrication, significantly lower than the sintering temperature of 1400 °C required by one-step fabrication mentioned above. The low sintering temperature can reduce the fabrication cost and facilitate to maintain microstructures formed at green substrate fabrication stage. By replacing a considerable amount of high-cost LSCF with low-cost ZnO in the substrate, the capital cost of the membrane will be reduced. The oxygen separation performance was systematically measured, and the fundamental mechanism was analyzed. To demonstrate the significantly improved robustness and durability of the membrane, long-term stability test was conducted under very harsh thermal-cycling conditions. The microstructures of the membrane devices were characterized and analyzed before and after the stability test.

3.2 Experimental

3.2.1 Fabrication of composite hollow fiber substrate

To fabricate hollow fiber substrate, the substrate slurry was first prepared. Specifically, ZnO (200 Mesh, Alfa Aesar, USA) powders and LSCF (Fuel cell materials, USA) powders were ball-milled in ethanol for 48 hours to form a mixture. After drying, the composite powders of LSCF-ZnO were obtained. The composite powders with two different ZnO/LSCF weight ratios were prepared, including 25 wt.% ZnO-75 wt.% LSCF, and 50 wt.% ZnO-50 wt.% LSCF, which are simply denoted as LSCF-ZnO7525 and LSCF-ZnO5050, respectively. The polyether sulfone (PESF, Veradel 3000P, Solvay Specialty

Polymers, USA; 5.21 wt.%) and polyvinylpyrrolidone (PVP, K30, CP, Sinopharm Chemical Reagent Co., China; 0.74 wt.%) were dissolved in N-methyl-2-pyrrolidone (NMP, HPLC grade, Sigma Aldrich, USA; 26.05 wt.%), followed by ball-milling for 2 h to form an organic solvent. The prepared LSCF-ZnO composite powders (68 wt.%) were added into the organic solvent and then ball-milled for another 48 hours to form a homogeneous LSCF-ZnO7525 and LSCF-ZnO5050 slurry, respectively. The as-prepared slurry was degassed for 10 min and loaded into the chamber of a stainless-steel die. A double orifice spinneret with outer diameter of 2.6 mm and inner diameter of 1.6 mm was attached at the bottom of the chamber. The details of the die and orifice design were published elsewhere.[89] The mixture of NMP (95 vol. %) and tap water (5 vol. %) was used as internal coagulant. The internal coagulant and slurry co-flew through the spinneret orifice. The flow rates of the slurry and internal coagulant were driven and controlled by a pressurized nitrogen gas system with flow meters (Seven Star, China). Tap water was used as external coagulant. The air gap between the tip of spinneret orifice and the surface of water bath was close to zero. The involved in-house built spinneret extrusion system and process control parameters were detailed elsewhere.[124, 125] Once the extruded slurry was immersed into the water bath, hollow fiber precursor was formed, and phase-inversion process took place. The exchange between water (non-solvent) in the water bath and NMP (solvent) in the slurry led to the formation of different porous microstructures depending on material compositions. In the meantime, solidification process occurred due to the decrease of solvent (NMP) concentration in the hollow fiber precursor. The extruded hollow fiber green bodies were left in water bath for 24 hours, allowing for the completion of the exchange and solidification process. After drying in air at room temperature, the

green hollow fibers were cut into desired length for further treatment and fabrication of functional layers.

3.2.2 Fabrication of hollow fiber membrane

Built upon the prepared green hollow fiber substrate, membrane functional layer was then fabricated. For this purpose, the dip coating solution of LSCF dense function layer were first prepared. Specifically, LSCF powders were mixed with dispersant, plasticizers, binder in a solvent, which was ball-milled for a few days to form a solution before use. The solution preparation for dense functional layer is detailed elsewhere.[124] The prepared LSCF solution was then dip-coated onto the green substrate. In particular, the green LSCF-ZnO7525 substrate was sealed at both ends using PTFE films and vertically immersed into the prepared solution for 10 seconds, followed by drying in air at room temperature. Such a coating procedure was repeated for 20 times. The coated samples were then co-fired at 1270 °C in air for 6 h to densify the LSCF coating layer while bonding the coating layer and substrate together, forming the membrane device LSCF-ZnO7525 substrate/dense thin film LSCF. The LSCF powders (60 wt.%) were mixed with ethyl cellulose (4 wt.%) and α-terpineol (36 wt.%) together, which was then grinded in a mortar for a few hours to form LSCF ink. The LSCF ink was then brush-painted onto the dense functional layer, followed by heat treatment at 1100 °C in air for 3h to form the membrane device LSCF-ZnO7525 substrate/dense thin film LSCF/porous LSCF.

3.2.3 Characterization and measurement

Phase compatibility between LSCF and ZnO was examined using X-ray diffraction (XRD) technique. Particularly, the green hollow fiber substrate was sintered at 1270 °C in air for 6h, which was crushed to obtain powders. The XRD patterns of the powders were

then obtained using Cu-Kα radiation (D/MAX-3C). The obtained XRD patterns were compared with those of individual LSCF and ZnO phases.

To obtain gas permeability of hollow fiber substrates, the LSCF-ZnO5050 and LSCF-ZnO7525 substrate precursors were sintered at 1270 °C in air for 6h. The gas permeability of the sintered substrates was measured. The apparatus and associated system for gas permeability measurement of hollow fiber substrate were detailed elsewhere.[89, 125]

The microstructures of the prepared samples were observed using scanning electron microscopy (SEM, Zeiss Gemini500 FESEM, Germany). The spatial distribution of elements was analyzed using SEM in combination with energy-dispersive X-ray spectroscopy (EDS) mapping technology.

The gas tightness of the fabricated hollow fiber membranes was examined at room temperature. Specifically, one end of membrane sample was sealed with epoxy resin while the other end was connected to nitrogen gas. The sample membrane was immersed into the water while a pressure of up to 2 bar was applied to the nitrogen gas. The observation of bubbles on the membrane surface was used to indicate whether the membrane is gas tight.

For oxygen separation measurement, the fabricated hollow fiber membrane with a length of 50 mm was first connected and sealed to two supporting alumina tubes at either end. In particular, the conductive adhesive ink (DAD-87, Shanghai Research Institute for Synthetic Resins, China) was first used to seal the connecting part, followed by aging at 900 °C in air for 30 min. The ceramic paste (Aremco Products Inc., USA) was then applied on the surface of the sealing part. After drying, alumina tube/hollow fiber membrane/alumina tube assembly was heat-treated at 950 °C in air for 30 min to bond the sealing part for subsequent oxygen permeation measurement.

For oxygen permeation test, argon sweep gas was supplied to the lumen side of the hollow fiber membrane while the shell side was exposed to ambient air. The operating temperature of the membrane was controlled by a high temperature tube furnace. The effluent gas from the hollow fiber membrane was sampled by a 5Å molecular sieve column and the concentrations of sampled gas species were analyzed using an online gas chromatography (GC-8A, Shimadzu, Japan). The oxygen permeation flux is then determined using the measured species concentrations and Eqn. (3-1),

$$J_{O_2} = \frac{F\left(C_{O_2} - C_{N_2}(21/79)\right)}{A} \qquad (3-1)$$

where J_{O_2} is the permeated oxygen flux of the membrane, A the effective area of the membrane, F the flow rate of the effluent gas, C_{O_2} the concentration of oxygen in the effluent gas, and C_{N_2} the concentration of nitrogen leaking into the sweep gas.

3.3 Results and discussions

Figure 3.2 shows the XRD patterns of the prepared LSCF-ZnO composite substrates with two different weight ratios. Clearly, all peaks correspond to LSCF and ZnO phases, respectively. No other impurity phases can be detected, indicating the excellent chemical compatibility between LSCF and ZnO at elevated temperatures. The peak intensity of ZnO phase in LSCF-ZnO5050 is higher than that in LSCF-ZnO7525, which is consistent with the ZnO content in the composite substrate.

Figure 3.3 shows cross-sectional and inner surface SEM images of the sintered hollow fiber substrates. It is clear to see that radially well-aligned microchannels with diameters of 10-20 μm are embedded in the LSCF-ZnO7525 substrate of (Figure 3.3a1). The microchannels are open at the inner surface of the substrate (Figure 3.3a2).

Interestingly, while radially well-aligned microchannels were created in the LSCF-ZnO5050 substrate as well (Figure 3.3b1), they start from the outer surface and extend radially to the middle of the substrate, forming the dead end microchannels. Beyond the microchannel region, a sponge-like layer is formed, close to the half thickness of the substrate. The SEM image of inner surface further confirms that no open microchannels can be found and the inner skin layer is porous with random pore distribution (Figure 3.3b2). In the well-mixed substrate slurry, ceramic particles are surrounded by polymers. Depending on the size, ceramic particles precipitate at different rates during the solvent/non-solvent exchange process. Small particles move fast and tend to precipitate near the interface while larger ones move slow and precipitate far from the interface.[119, 126] The particle size of LSCF powder used for the spinning slurry is in the range of 0.7-1.1 μm while that of ZnO is about 70-80 μm. The ceramic particle size difference in combination with solvent/non-solvent gradients at inner and outer interfaces form very complicated precipitation dynamics to drive motions of ceramic particles and polymers, leading to hollow fiber sample with microstructures mentioned above. Clearly, the ZnO content in the composite affects precipitation dynamics, leading to different porous microstructures. Compared to the open radially well-aligned microchannels in the LSCF-ZnO7525 sample, the dead end microchannels and thick sponge-like layer would significantly hinder facile gas diffusion in LSCF-ZnO5050 sample.

Figure 3.4 displays gas permeation properties of the two hollow fiber substrates. The sintered LSCF-ZnO5050 substrate shows the permeability of ~1×10^4 $L\cdot m^{-2}\cdot h^{-1}\cdot bar^{-1}$, which is close to that of the hollow fiber substrate prepared by conventional method.[89] Interestingly, the gas permeability of LSCF-ZnO7525 substrate is around 10×10^4 $L\cdot m^{-2}\cdot h^{-}$

$^{1}\cdot bar^{-1}$, one order of magnitude higher than that of LSCF-ZnO5050 substrate. This result is consistent with the microstructure observation mentioned above. While more ZnO content could effectively enhance the mechanical strength of the substrate, it also destroyed the microstructure of open microchannels desired for facile gas diffusion as demonstrated here. Therefore, LSCF-ZnO7525 substrate is employed for further membrane fabrication to get a tradeoff between mechanical strength and gas diffusion property.

The LSCF separation functional layer was further fabricated built upon the LSCF-ZnO7525 substrate. For this purpose, LSCF solution was prepared, and dip coated onto the LSCF-ZnO7525 substrate. After drying, the coated hollow fiber sample was sintered at 1270 °C in air for 6 h, forming LSCF-ZnO7525/LSCF membrane device. Figure 3.5 shows the microstructure of the sintered membrane sample. The cross-sectional view in Figure 3.5a and 3.5b indicates that the thin film (~15 μm) separation layer is bonded onto the substrate very well. The radially well-aligned microchannels in the substrate remained well after high temperature sintering process, indicating their excellent thermal stability. The outer surface with separation layer being partially peeled off during sample preparation for characterization (Figure 3.5c) shows that the radially aligned microchannels are directly connected with the separation layer. This provides advantages for facile surface exchange process. The surface SEM of the separation layer (Figure 3.5d) clearly shows very good grain-boundary contacts, implying the gas-tightness of the thin film separation layer.

The EDS analysis shows that various elements are uniformly distributed (Figure 3.6). It is noteworthy that Zn distribution is confined within the substrate area, no Zn can be found in the region of dense LSCF separation layer. This observation confirms that no Zn element diffuses from the substrate to the dense LSCF layer during high temperature

sintering process even though the gradient of Zn element content exists between the two regions. As demonstrated above, ZnO is chemically compatible with LSCF and can reduce the sintering temperature of the bulk, both of which facilitates to resist Zn diffusion during the sintering process.

A porous catalysis layer of LSCF was further fabricated on the dense LSCF separation layer to form LSCF-ZnO7525/LSCF/porous LSCF membrane device. This was obtained by directly brush-painting LSCF ink onto the surface of LSCF separation layer, followed by heat treatment at 1100 °C in air for 3h. Figure 3.7 shows the microstructure of the LSCF-ZnO7525/LSCF/porous LSCF membrane device. It can be seen from Figure 3.7a that the thin functional layers are intimately contact with the microchannels-structured substrate. The zoomed region near the functional layers (Figure 3.7b) clearly indicates that a porous LSCF layer with a thickness of about 4 μm is well adhered to the dense LSCF separation layer, serving as a catalytic layer.

The oxygen permeation performance and stability of the fabricated hollow fiber membranes were systematically measured. The shell side of the hollow fiber as the feed side is exposed to ambient air. Argon gas as sweep gas is supplied to the lumen side. The operating temperature of the membrane is controlled by a high temperature test furnace. The permeation performance is measured in the temperature range of 800-950 °C with different sweep gas flow rates. Figure 3.8 shows the measurement results of LSCF-ZnO7525/LSCF membrane. For a given argon sweep gas flow rate, the oxygen permeation flux increases with increasing operating temperature from 800 to 950 °C, indicating thermally activated nature of permeation process. When the membrane is operated at 800 °C, the sweep gas flow rates have little effect on the oxygen permeation flux. Since

the sweep gas flow directly decreases oxygen partial pressure at the permeate side, this in turn enhances oxygen evolution process. The result implies that oxygen evolution process is not a limiting step in the entire oxygen permeation process of the membrane at the operating conditions. Beyond the operating temperature of 800 °C, oxygen permeation flux was improved upon increasing the sweep gas flow rate from 10 to 80 $ml \cdot min^{-1}$. Obviously, the higher the operating temperature the better the performance was improved. This observation implies that the variation of operating temperature may change the reactions involved in the permeation process from a none limiting step to a limiting one. It is also noticed that at a relatively low temperature (e.g., 850 °C), the oxygen permeation flux increased with increasing sweep gas flow rate from 10 to 50 $ml \cdot min^{-1}$. Beyond the 50 $ml \cdot min^{-1}$, the oxygen permeation flux showed little change. This result indicates that the oxygen evolution process was a limiting step at relatively low sweep gas flow rate but turned into a none limiting one at relatively high sweep gas flow rate. However, at higher operating temperatures of 900 and 950 °C, the oxygen permeation flux kept increasing with increasing sweep gas flow rate from 10 to 80 $ml \cdot min^{-1}$, implying oxygen evolution process is always a limiting step under these operating conditions. These observations demonstrate that every single step in oxygen permeation process was affected by operating conditions (operating temperature, sweep gas flow rate) in a complicated way. Depending on the variations of operating conditions, the reaction step in oxygen permeation process may change from a limiting step to a none limiting one, vise verse. The Arrhenius plot of oxygen permeation flux under different sweep gas flow rate is shown in Figure 3.8b. The activation energy derived from the Arrhenius plot is shown in Figure 3.8c. Clearly, the activation energy increases with increasing the sweep gas flow rate. As mentioned above, increasing

the sweep gas flow rate decreases oxygen partial pressure at the permeate side. This will increase the chemical potential across the membrane for oxygen permeation given the ambient air at the feed side. Accordingly, the activation energy for oxygen permeation should decrease. On the other hand, the Argon sweep gas at room temperature was supplied to the permeate (lumen) side of the membrane at elevated temperatures. This in turn will reduce the operating temperature of the membrane, increasing the activation energy. The effect of the latter could surpass that of the former, leading to the combinational effect of activation energy increase. This cooling effect shows greater influence for the membrane with microchannels open at inner surface of substrate and extend directly to the interface of function layer as displayed in the above SEM pictures. Short-term stability of LSCF-ZnO7525/LSCF membrane was tested. The Argon sweep gas flow rate of 50 $mL \cdot min^{-1}$ was used and the operating temperature was controlled at 900 °C. The oxygen permeation flux was recorded every one hour with an interval of 12 hours due to overnight. The whole test was running in total for about 150 h and the result is shown in Figure 3.8d. During the first 60 h, the oxygen permeation flux increased asymptotically from about 0.8 to 1.2 $mL \cdot cm^{-2} \cdot min^{-1}$. This stage may attribute to the activation process of the membrane, where defects and their distributions in the bulk could take time to change from one equilibrium (after fabrication) to another under current operating conditions. Between 60 - 100 h, the membrane performance was very stable. Beyond 100 h, the oxygen permeation flux decreases a little bit and then was stabilized by the end of the test (~ 150 h). This observation implies that the material defect and microstructure reached a new equilibrium.

As mentioned above, at 800 °C, oxygen evolution reaction at the permeate side is not a limiting step because increasing Argon sweep gas flow rate has little effect on oxygen

permeation flux. This result also implies that either charge transport through the bulk or oxygen reduction reaction at the feed side limits oxygen permeation process. It has been realized that the oxygen permeation process in LSCF membrane is limited by charge (oxygen ion) transport process when the membrane thickness is larger than 1.25 mm. Only when the thickness is reduced to 0.62 mm, surface exchange and bulk diffusion start to jointly affect oxygen permeation flux. [127] Based on this understanding, it is reasonable to assume that the characteristic length of LSCF bulk is roughly between 0.62 and 1.25 mm. Since the dense LSCF separation layer fabricated in this research is very thin (~ 15 μm), it is less likely that the charge transport through the dense layer is a limiting step. Accordingly, oxygen reduction reaction at the feed side is assumed to be a limiting step. To improve membrane performance, the properties for oxygen reduction reaction at the feed side needs to be enhanced. This can be achieved by improving the effective surface area for oxygen reduction reaction or using high performance catalyst. Here, the former strategy is employed. For this purpose, a thin porous LSCF layer was coated onto the dense LSCF separation layer, forming a hollow fiber membrane LSCF-ZnO7525 substrate/dense LSCF/porous LSCF as mentioned above. The oxygen permeation performance was systematically measured. The shell side was used as the feed side with ambient air being supplied while Argon sweep gas was supplied into the lumen side. The operating temperature was controlled in the range of 800 - 950 °C. Figure 3.9 shows the oxygen permeation performance of the membrane under different operating conditions. Obviously, at 800 °C, oxygen permeation flux increased with increasing Argon sweep gas from 10 to 40 $mL \cdot min^{-1}$, indicating oxygen evolution step at the permeate side becomes a limiting step again. Beyond the sweep gas flow rate of 40 $mL \cdot min^{-1}$, the oxygen permeation flux kept a

constant value. This result further confirms the understanding that the operating conditions affect the oxygen permeation process in a complicated way. The limiting reaction step can change into a none limiting one depending on specific operating conditions. Beyond the operating temperature of 800 °C, the oxygen permeation flux kept increasing with increasing the argon sweep gas flow rate from 10 to 80 mL·min-1, indicating that the oxygen evolution reaction is always a limiting step under these conditions. Comparing the membrane performance in Figure 3.8a and Figure 3.9a, one can see that within the range of sweep gas flow rate 10 to 40 mL·min-1, the lowest temperature for oxygen evolution reaction to transit from a limiting step to a none limiting one in the membrane without surface catalyst layer was 850 °C (Figure 3.8a). But the lowest temperature was reduced to 800 °C for the membrane with surface catalyst layer. Since surface catalyst layer is the only difference between the two membranes, the result indicates that such a temperature difference was induced by the porous LSCF catalyst layer. The comparison implies that a limiting step in oxygen permeation process can be evolved between oxygen evolution reaction at the lumen side and oxygen reduction reaction at the shell side depending on the surface microstructure and operating conditions. The Arrhenius plot of oxygen permeation flux under different sweep gas flow rate is shown in Figure 3.9b. The activation energy derived from the Arrhenius plot is shown in Figure 3.9c. Clearly, the activation energy increases with increasing the sweep gas flow rate, like those of the membrane without surface catalyst layer (Figure 3.8c), due to the same reason as mentioned above. Comparing the activation energy of the membrane LSCF-ZnO7525 substrate/dense LSCF with the membrane LSCF-ZnO7525 substrate/dense LSCF/porous LSCF, one can see that the latter is much lower than the former especially at the conditions of higher sweep gas flow rates.

This result is consistent with the performance of oxygen permeation flux mentioned above due to the same reason. Since the surface catalyst layer is the only difference between the two membranes, it is reasonable to assume that the decrease of the activation energy is primarily induced by the surface catalyst layer. As shown in Figure 3.9d, the activation energy difference increases with increasing argon sweep gas flow rate, particularly at relatively low sweep gas flow rate. The ratio of the decreased activation energy with respect to the total activation energy of the membrane without LSCF catalytic layer increases when the sweep gas flow rate increases from 10 to 30 mL min^{-1} (see the right vertical axis in Figure 3.9d). Beyond 30 mL min^{-1}, such a ratio reaches and maintains at a high value. In other words, surface catalyst layer plays a more important role in reducing the overall activation energy of the membrane at relatively high sweep gas flow rates.

Long-term stability of the membrane LSCF-ZnO7525 substrate/dense LSCF/porous LSCF was also conducted. The Argon sweep gas flow rate of 50 mL·min^{-1} was used and the operating temperature was controlled at 900 °C. The data was obtained in the same way as we tested the stability of LSCF-ZnO7525 substrate/LSCF membrane while this time the whole test was running for about 400 h. The results are shown in Figure 3.10, where the left vertical axis is the oxygen permeation flux while the right axis is the applied thermal cycling load on the membrane. During the first 150 h, a constant temperature of 900 °C was applied to the membrane, and the oxygen permeation flux was very stable. Beyond 150 h, a set of thermal cycling with different heating up and cooling down rates were applied to the membrane between 600 and 900 °C. Specifically, in the first set of thermal cycles, the operating temperature was decreased from 900 to 600 °C at the cooling rate of 3 °C·min^{-1}, maintained at 600 °C for 1h, followed by heating up back

to 900 °C at the heating rate of 3 °C·min^{-1}, and then maintained at 900 °C for 2h. Such a process was repeated for 3 cycles, forming the first set of thermal cycles. In the following second and third sets of thermal cycles, the heating and cooling rates of 5 °C·min^{-1} and 7 °C·min^{-1} were used respectively, the rest of parameters are the same as those in the first thermal cycle. In the last set of thermal cycles, the heating and cooling rates of 5 °C·min^{-1} was used. The overall thermal cycles applied to the membrane are also illustrated in Figure 3.10. It can be seen that oxygen permeation flux was very stable during the first ~ 280 h. After a total of 20 thermal cycles in the 200-h operation, the maximum performance degradation was about 15.2%. Given the very harsh operating conditions, e.g., long-term and thermal cycling load, such a degradation demonstrated that the stability of the membrane is superior.

After the long-term stability test, the membrane sample was further characterized. Figure 3.11 shows the SEM and EDS of the post-test membrane LSCF-ZnO7525 substrate/dense LSCF layer/porous LSCF layer. It can be seen that the radially aligned microchannels remained well in the substrate, and the dense LSCF separation layer still showed intimate contact with the porous LSCF layer and the substrate on either side. No crack or delamination can be observed. The EDS results indicate that the element La, Co, and Fe are uniformly distributed in the marked region. The element Zn is confined within the substrate, no observable Zn is diffused into the separation layer or porous catalyst layer. However, the element Sr seems showing certain nonuniformity particularly in the substrate region. It has been recognized that Sr tends to segregate onto the bulk surface of LSCF during the long-term high temperature conditions.[128] Under the long-term and harsh thermal cycling conditions, the Sr element of LSCF could segregate onto the surface of

radially-aligned microchannels in the substrate, leading to the observed nonuniform distribution of Sr element. Overall, the characterization of the post-test membrane sample indicates that the membrane structure is very stable and robust. This further implies that the ZnO addition into the LSCF substrate is able to significantly enhance the mechanical strength, robustness, and durability of hollow fiber membranes for practical applications.

3.4 Conclusion

A composite ZnO-LSCF hollow fiber substrate was successfully fabricated using spinneret process in combination with modified phase inversion method. The ZnO content was optimized so that radially well-aligned open microchannels were created in the substrate. Built upon the composite substrate, thin film dense LSCF separation layer was successfully fabricated, and a thin porous LSCF catalyst layer was also fabricated on the dense separation layer, forming an asymmetric hollow fiber membrane. The fabricated membrane devices were characterized and systematically measured in different operating conditions. The oxygen permeation process is thermally activated in nature and its limiting steps are affected by operating conditions. A limiting step in one operating condition could be changed to a non-limiting step in a different operating condition. Accordingly, oxygen permeation performance of the membrane can be improved by changing operating condition or design associated with the limiting steps, such as increasing sweep gas flow rate or effective surface area with porous catalyst layer. The novel hollow fiber membrane demonstrated very good long-term and thermal cycling stability. Overall, the ZnO formed ZnO-LSCF composite hollow fiber substrate and membrane device can significantly reduce the capital cost, decrease the sintering temperature, and improve the mechanical strength, and therefore the robustness and stability for oxygen permeation applications.

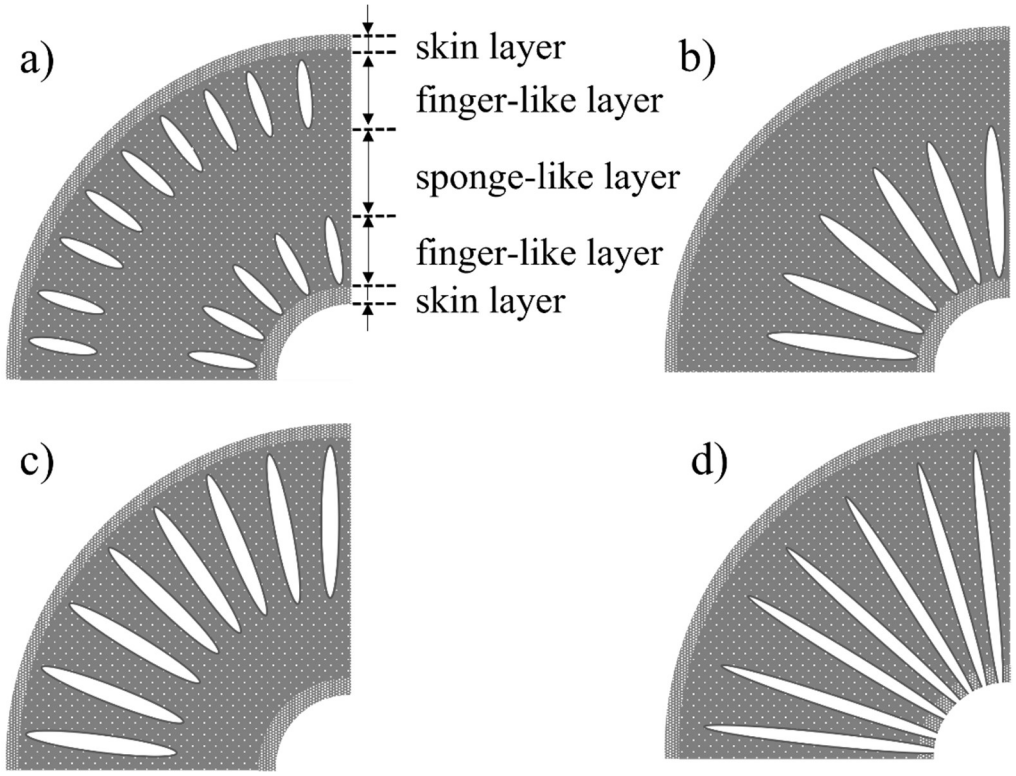

Figure 3.1 Cross-sectional microstructure illustration of hollow fibers prepared by slurry spinneret technology in combination with phase inverse method. **a)** Conventional method; **b)** Modified method with sponge layer close to shell side; **c)** Modified method with sponge layer close to lumen side; **d)** Modified method with open pores at lumen side.

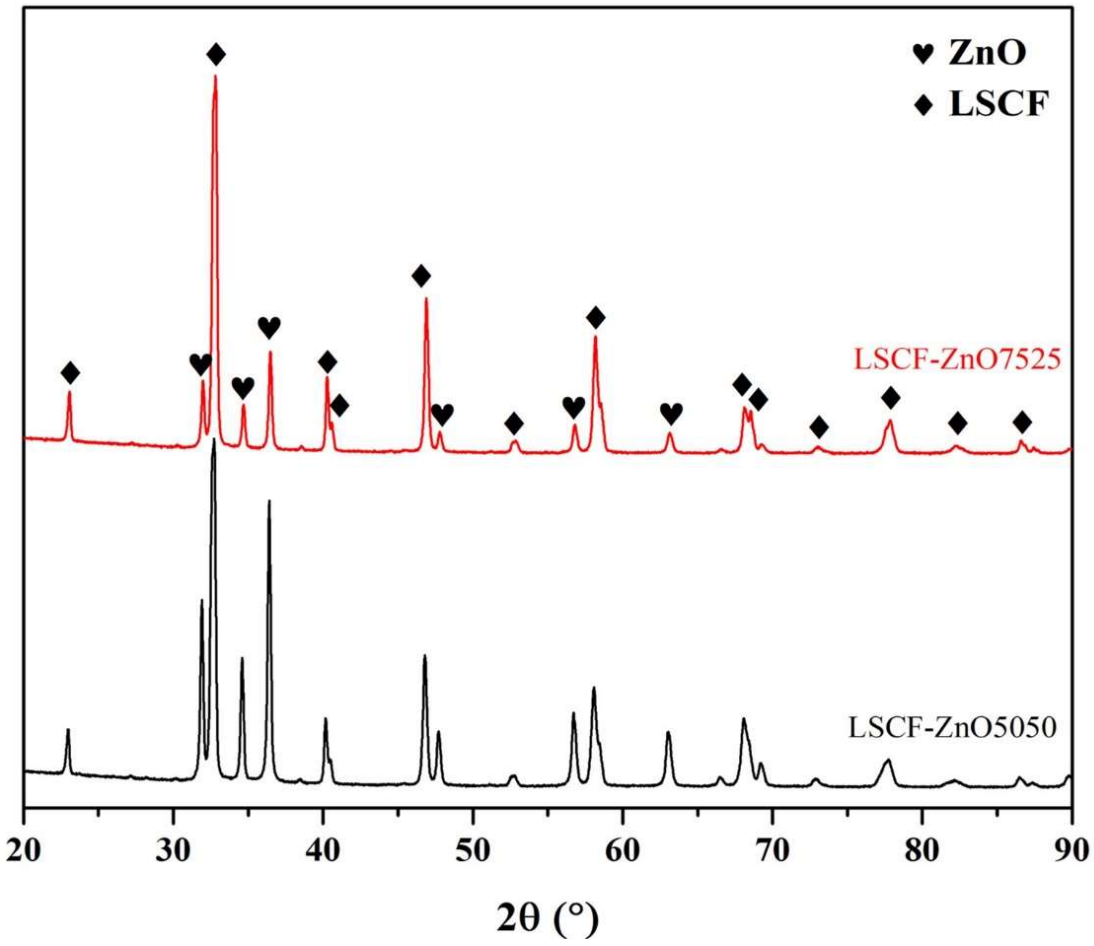

Figure 3.2 XRD patterns of LSCF-ZnO membrane sintered at 1270 °C for 10h.

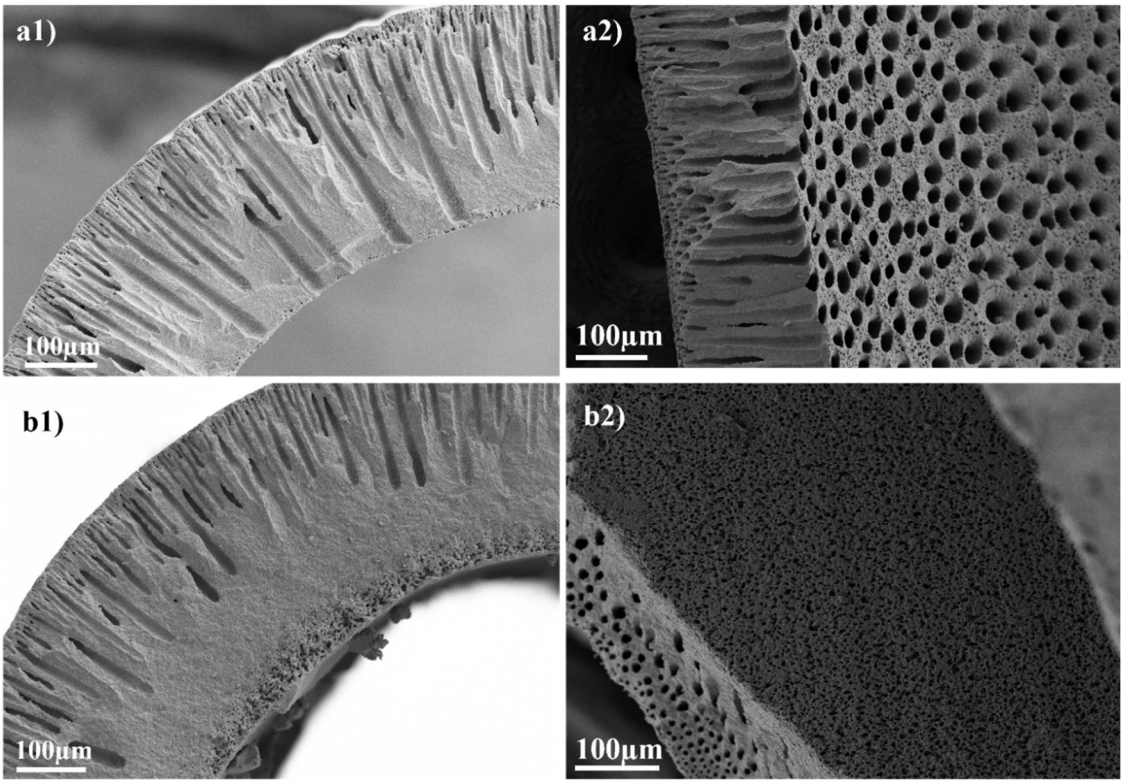

Figure 3.3 Cross-sectional and inner surface SEM images of the composite hollow fiber substrate sintered at 1270 °C in air for 6 h. **a)** LSCF-ZnO7525; **b)** LSCF-ZnO5050.

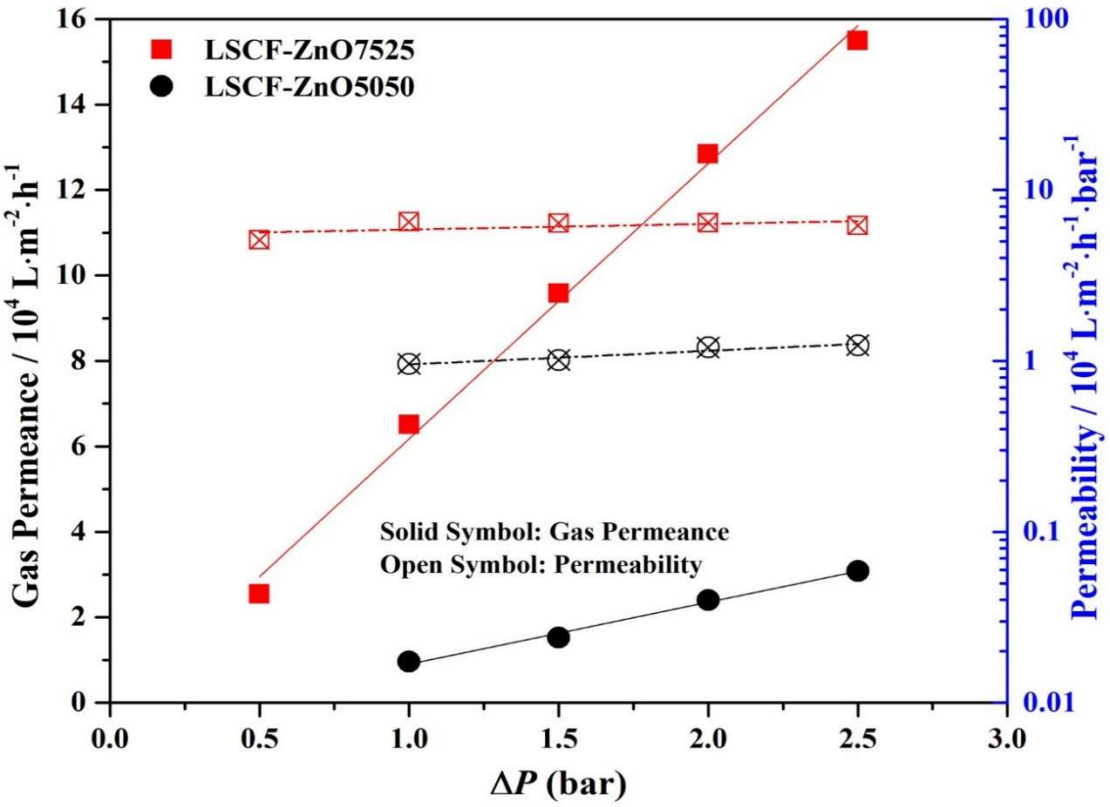

Figure 3.4 Gas permeability of the as-prepared hollow fiber substrates LSCF-ZnO7525 and LSCF-ZnO5050 at room temperature.

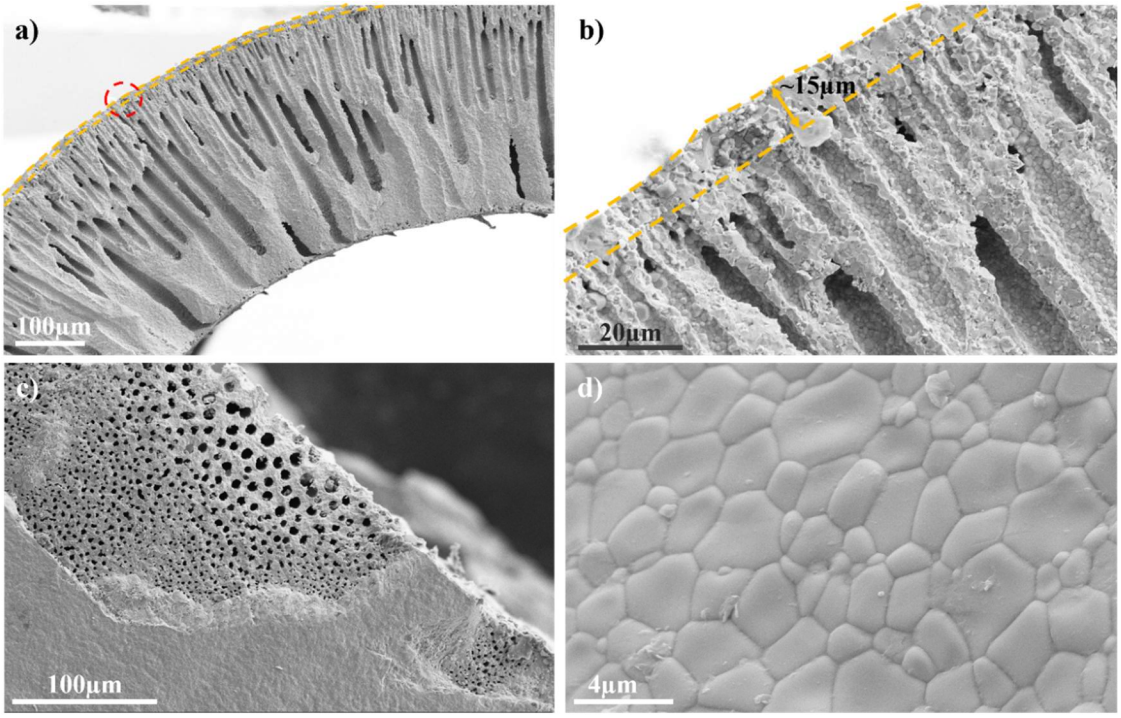

Figure 3.5 SEM images of LSCF-ZnO7525 supported LSCF oxygen permeation membrane sintered at 1270 °C for 6h. **a)** Cross section; **b)** Enlarged figure of red-circled area; **c)** outer surface; **d)** enlarged figure of outer surface.

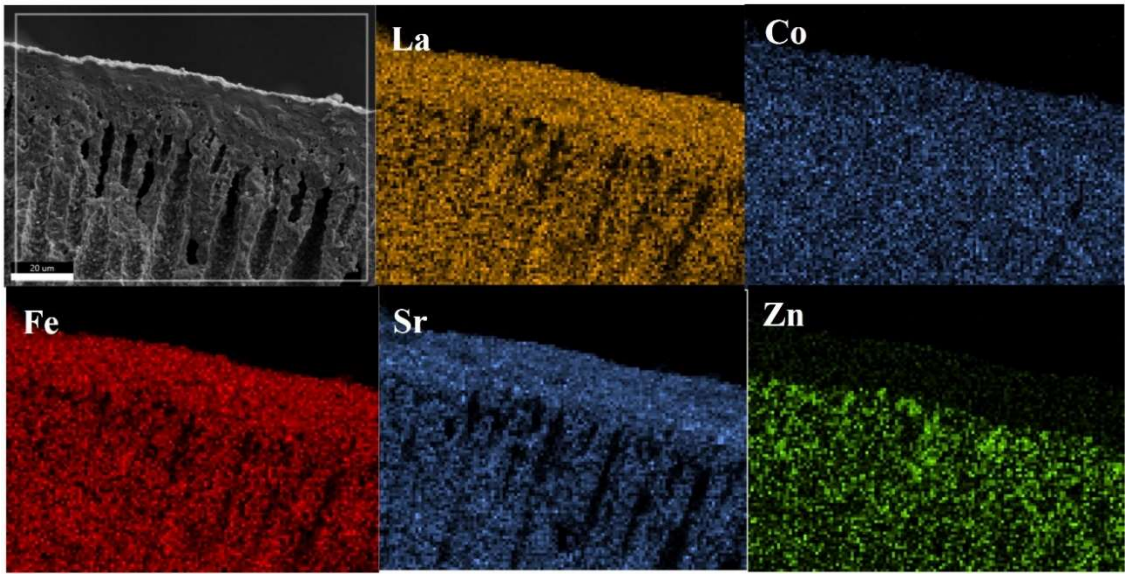

Figure 3.6 Cross-sectional SEM images of the LSCF-ZnO7525 supported thin film LSCF oxygen permeation membrane sintered at 1270 °C in air for 6 h.

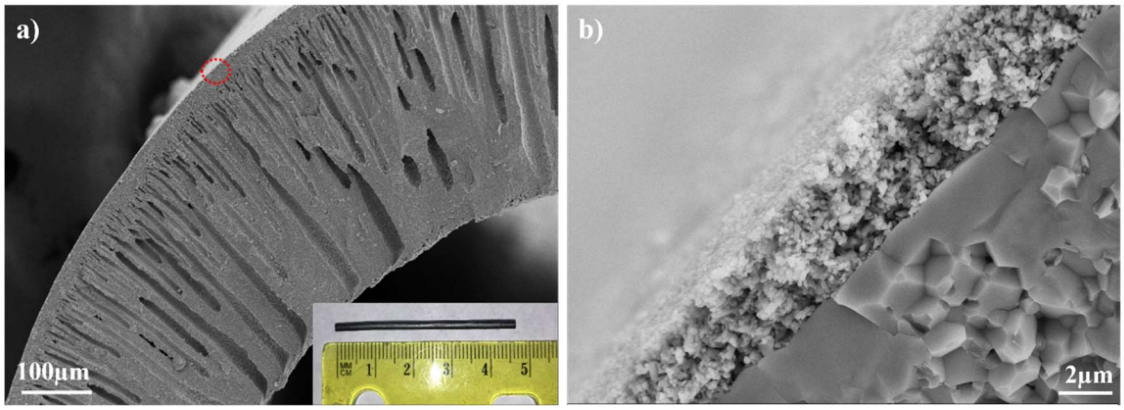

Figure 3.7 SEM images of LSCF-ZnO7525/LSCF/porous LSCF membrane device. **a)** cross section; the insert is the image of fabricated membrane sample; **b)** zoomed area marked by the dashed red circle in **a)**.

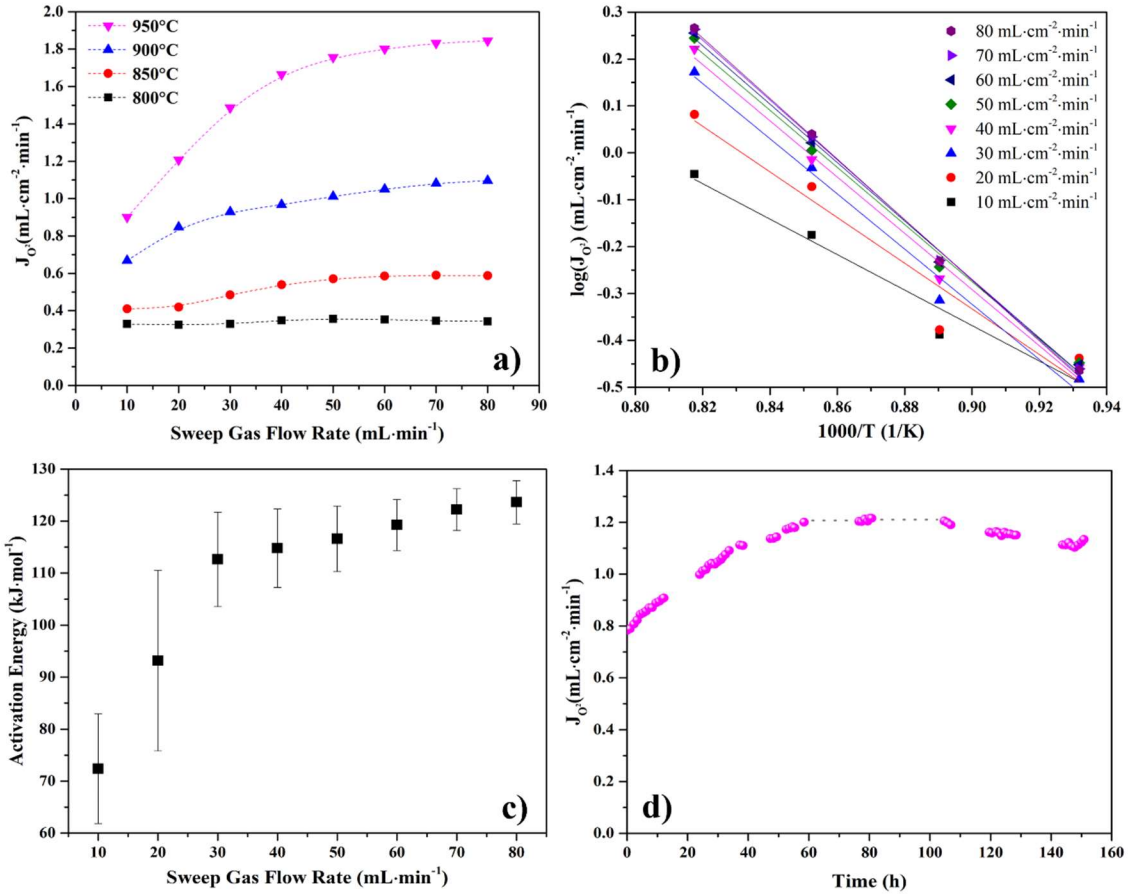

Figure 3.8 Performance of LSCF-ZnO7525 substrate/LSCF membrane. **a)** Oxygen permeation flux, **b)** Arrhenius plot, **c)** activation energy, **d)** stability.

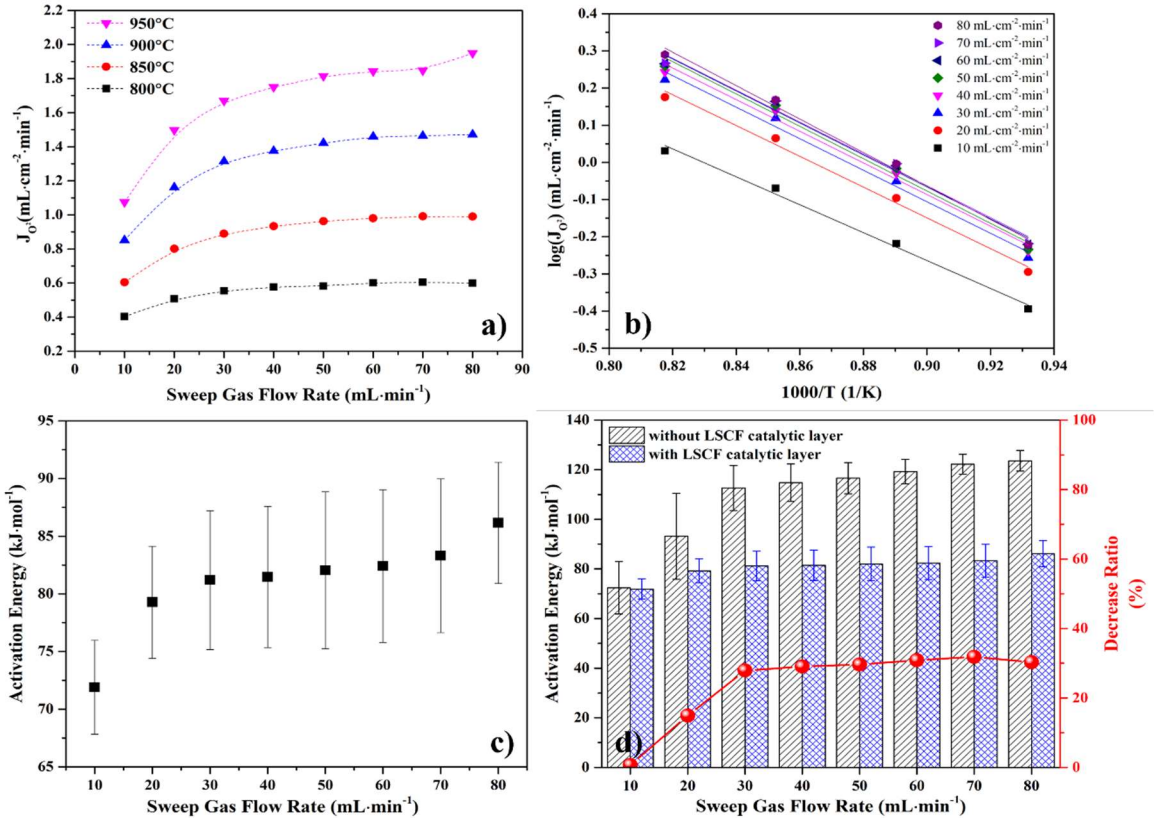

Figure 3.9 Performance of LSCF-ZnO7525 substrate/LSCF/porous LSCF membrane. **a)** Oxygen permeation flux, **b)** Arrhenius plot, **c)** activation energy, **d)** activation energy difference induced by surface catalyst layer.

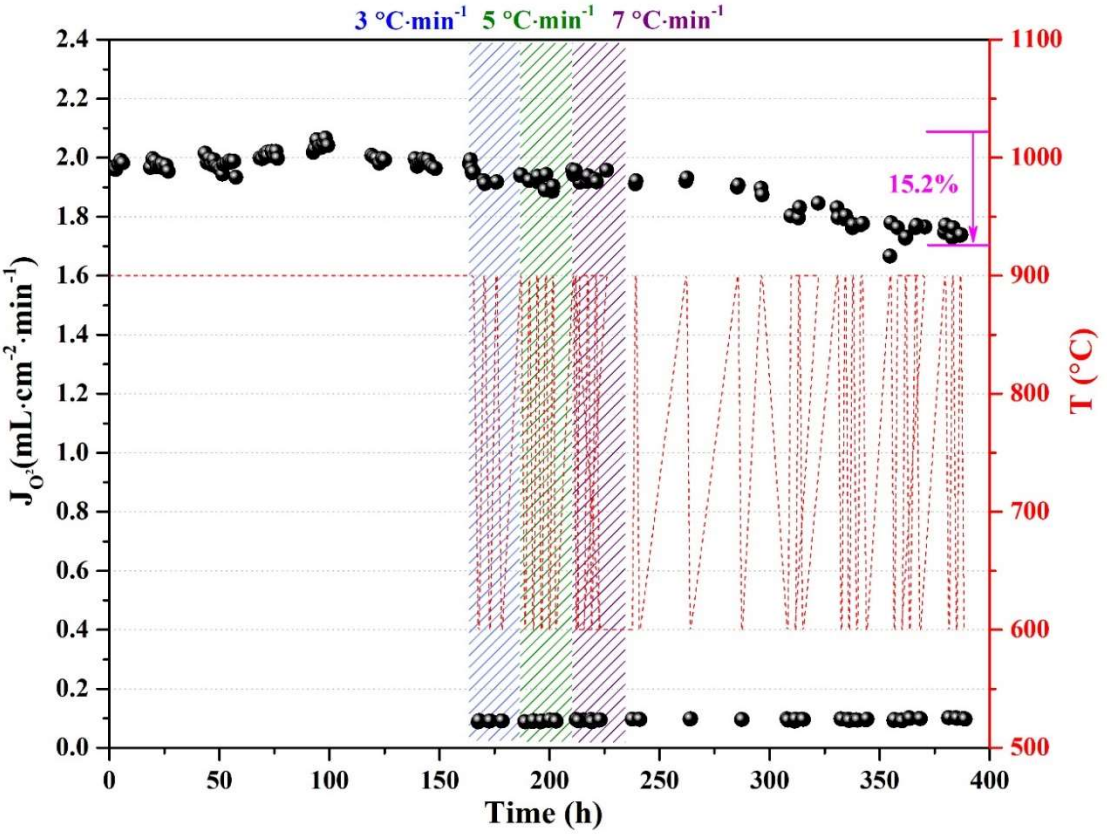

Figure 3.10 long-term and thermal cycling stability of the membrane LSCF-ZnO7525 substrate/dense LSCF layer/porous LSCF layer.

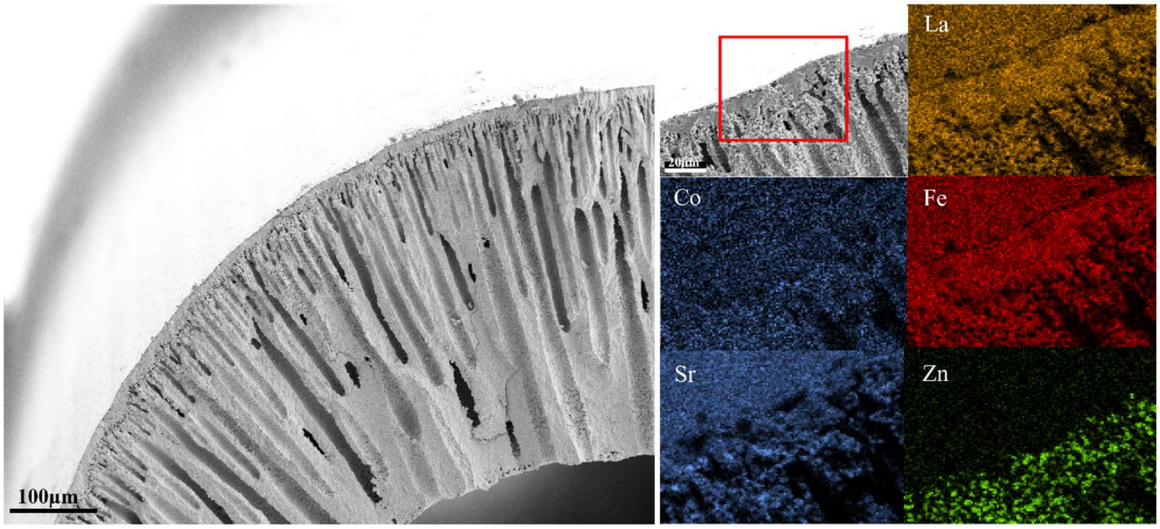

Figure 3.11 SEM and EDS images of the membrane LSCF-ZnO7525 substrate/LSCF separation layer/porous LSCF catalytic layer after long-term stability.

CHAPTER 4

SURFACE MODIFICATION WITH COBALT OXIDE NANOCLUSTER FOR ENHANCED SURFACE OXYGEN EXCHANGE OF GDC-LSCF MEMBRANE: FABRICATION, TRANSPORT MECHANISM, AND STABILITY

4.1 introduction

Oxygen production directly from air using dense ceramic membrane technologies has attracted considerable attention in the past few decades due to their high selectivity and economic benefits [6, 9, 116, 117]. The dense ceramic membrane technology for oxygen permeation can also provide advantage of directly integrating with combustion technology, whereby oxyfuel combustion can be obtained. This may significantly improve the efficiency of power plants while facilitating CO_2 capture [129].

The basic structure of oxygen permeation device is a gas-tight dense ceramic membrane. The material used for the membrane is either a mixed ionic and electronic conductor (MIEC) or a composite that can conduct both ions and electrons simultaneously [74, 116, 130, 131]. Due to thermally activated nature of charge transport in bulk ceramics, membranes need to be operated at elevated temperatures. And oxygen chemical potential gradient across the membrane is also needed to drive oxygen permeation process. Usually, air is supplied to the feed side of the membrane, where oxygen reduction reaction (ORR) takes place and oxygens are incorporated into oxygen vacancies of ceramic bulk, migrating

to the permeate side of the membrane. At the permeate side, oxygen evolution reaction (OER) occurs, and oxygen ions are released from ceramic bulk, forming gas phase oxygen. Apparently, from the point view of membrane designs, oxygen permeation performance is determined by the characteristics of ceramic bulk and bulk/gas interfaces. It has been recognized that oxygen permeation performance is limited by surface exchange processes when the thickness of membrane is less than the critical length of the corresponding bulk [132]. Since the membrane thickness at micro-scales can be obtained using thin film fabrication technologies, it would be important to control the characteristics of membrane surfaces so that high surface exchange rate can be achieved. This is usually obtained by surface modifications, for example, a porous catalyst layer can be applied on dense membrane surface to increase effective surface area for oxygen exchange. The widely used method for surface modification of membranes is coating method [133-136]. The acid treatment was also employed to improve effective surface area [137]. To significantly enhance effective surface area, the synthesis method for nanostructured materials was introduced to modify membrane surface. In particular, cobalt oxide (Co_3O_4) nanorods were grown on the surface of $Ba_{0.5}Sr_{0.5}Co_{0.8}Fe_{0.2}O_{3-\delta}$ membrane by using hydrothermal synthesis method [138]. As a result, oxygen permeation performance of the membrane was improved by 20% at 850 °C compared to the membrane without Co_3O_4 nanorod-structured surfaces. Such a surface modification method is still at its early stage for the fabrication of high-performance ceramic membranes. Since ceramic membranes are operated at elevated temperatures, thermal stability of nanostructured surfaces is still a concern and needs to be further studied toward practical applications. Also, it is not clear how the nanostructured surfaces affect oxygen permeation process, particularly the surface exchange process.

In this research, the composite of $Gd_{0.2}Ce_{0.8}O_{1.95}$ (GDC, 70 wt.%) and $(La_{0.6}Sr_{0.4})_{0.95}Co_{0.2}Fe_{0.8}O_{3-\delta}$ (LSCF, 30wt.%), simply denoted as GDC-LSCF, was used as a model material system to fabricate membrane. The GDC-LSCF composite was also used as the electrodes of GDC electrolyte-supported symmetric cells. Co_3O_4 precursor nanoclusters were then self-assembled onto the surfaces of the prepared membrane and symmetric cell by hydrothermal synthesis method. Systematic electrochemical measurements were conducted using the membrane and symmetric cells with two-electrode and three-electrode configurations. Surface exchange processes were analyzed including ORR and OER under different operating conditions and the effects of nanostructured surface are identified. A short-term stability (~ 100 h) was performed using symmetric cell, and both the performance and microstructure stability were characterized.

4.2 Experimental

4.2.1 Sample Preparation

Commercial 30wt.% LSCF powders (Fuel cell Materials, Ohio) were ball milled with 70 wt.% GDC (Fuel cell materials, Ohio) powders in ethanol for 2 hours. The mixture was dried in an oven at 80 °C overnight. The mixed powders were then mixed with polyvinyl butyral (PVB, 2 wt.%, Butvar B-98, Spectrum, USA) and uni-axially pressed into pellets (diameter ~15mm) using a stainless-steel die and a hydraulic equipment. The green pellets were sintered at 1400 °C in air for 6h to obtain dense samples with a relative density above 95%. The surface of sintered pellets was mechanically polished using sandpapers followed by washing with ethanol in an ultrasonic cleaner and the thickness of all prepared samples was controlled at ~350 μm.

The prepared LSCF-GDC pellets were used as the substrate for the growth of Co_3O_4 nanostructured surfaces using a hydrothermal synthesis process. Specifically, 1.25 mmol of $Co(NO_3)_2 \cdot 6H_2O$, 5 mmol NH_4F and 12.5 mmol urea were dissolved in 30 mL distilled water and stirred for 15 min to form a homogeneous solution. The solution was loaded into a Teflon-lined stainless-steel autoclave. The as-prepared LSCF-GDC pellets were immersed into the solution and soaked at 100 °C for 10 h, followed by cooling down to room temperature. When only one surface of the pellet needed to be modified, another surface was covered by a tape. The membranes were then rinsed with distilled water to clean up residual reactants and debris. After drying, the membranes were calcined at 900 °C in air for 3h to bond nanoclusters onto the membrane surface.

The green GDC pellets were prepared using the same procedure as the LSCF-GDC pellets mentioned above. The green GDC pellets were densified by sintering at 1450 °C in air for 6h. The dense GDC pellets were surface-polished with sandpaper, followed by ultrasonic cleaning in ethanol. The GDC-LSCF composite powders (60 wt.%) prepared above was mixed with α-terpineol (36 wt.%) and ethyl-cellulose (4 wt.%), and thoroughly ground to form electrode ink. The electrode ink was then screen-printed onto both sides of GDC pellets, which was sintered at 1100 °C in air for 2h to form symmetrical cell GDC-LSCF/GDC/GDC-LSCF. Silver wires were attached onto both sides of the symmetrical cells using silver paste (Heraeus 2807). Silver wire was also wound and attached with silver paste around the circumference of GDC electrolyte substrate. The symmetrical cells were then used for two-electrode and/or three-electrode measurement using electrochemical impedance spectra (EIS) technique. The Co_3O_4 nanoclusters were also synthesized on both surface of symmetrical cell LSCF/GDC/GDC-LSCF, followed by calcinating at 900 °C in

air for 3h to bond nanoclusters onto the surfaces of symmetrical cell. Silver wires were then attached to both surfaces of the cell and/or circumference of GDC electrolyte substrate for further measurement.

4.2.2 Oxygen permeation measurement

The prepared membrane sample was sealed on the top of an alumina tube using conductive adhesive ink (DAD-87, Shanghai Research Institute for Synthetic Resins, China) and heat-treated at 200 °C in air for 2h. Ceramic paste (Aremco Products Inc., USA) was then applied on the circumference of the sealing part and membrane. The membrane-alumina tube assembly vertically stood, and its temperature was controlled by a test furnace. The top surface of membrane as feed side was exposed to ambient air. Argon gas was supplied into the supporting alumina tube toward the bottom surface of the membrane. The effluent gas from the alumina tube was sampled by an online gas chromatography (GC-8A, Shimadzu, Japan) system with a 5Å molecular sieve column. The concentration of oxygen in the effluent gas was analyzed, and the corresponding oxygen permeation flux was determined using Eqn. (4-1),

$$J_{O_2} = \frac{F\left(C_{O_2} - C_{N_2}(21/79)\right)}{A} \qquad (4-1)$$

where J_{O_2} is the permeated oxygen flux of the membrane, A the effective area of the membrane, F the flow rate of the effluent gas, C_{O_2} the concentration of oxygen in the effluent gas, and C_{N_2} the concentration of nitrogen leaking into the sweep gas.

4.2.3 Electrochemical measurements

The as-prepared symmetrical cells were measured to understand the role of Co_3O_4 nanocluster-structured surface in improving surface exchange process. Specifically, the

symmetric cell was sealed in an alumina chamber. The temperature of the chamber was controlled by a test furnace. Gas mixture was supplied into the chamber by mixing oxygen and nitrogen through a three-way valve. The flow rates of O_2 and N_2 were controlled by flow meters (APEX) and the total flow rate was controlled at 60 $mL \cdot min^{-1}$. By tuning the flow rate of oxygen and nitrogen, the gas mixture with oxygen partial pressure of 0.21, 0.5 and 1.0 atm were obtained in the chamber. Under each of oxygen partial pressures, EIS was measured in the temperature range of 800-900 °C using two-electrode configuration of the symmetrical cell and Zahner IM6E electrochemical workstation. The voltage perturbation was set at 10 mV while the sweeping frequency range was from 10^6 Hz to 0.1 Hz. To further understand ORR and OER in individual electrode, three-electrode configuration with symmetrical cell was employed for EIS measurement in ambient air and temperature range of 800-900 °C. The current load from -160 $mA \cdot cm^{-2}$ to 160 $mA \cdot cm^{-2}$ was applied between working and counter electrode. The EIS was measurement between the reference and working electrode.

4.2.4 Characterization

The phase compositions of as-prepared samples were identified with X-ray diffraction (XRD) technique (D/MAX-3C) scanned a rate of 5° min^{-1} in the range of 20-90° (2θ). The microstructure and micromorphology of the samples were characterized using scanning electron microscopy (SEM) technique (Zeiss Gemini500 FESEM, Germany).

4.3 Results and discussions

4.3.1 Phase and microstructure

With the prepared solution containing $Co(NO_3)_2 \cdot 6H_2O$, NH_4F and urea, the following reaction (4-2) takes place under hydrothermal conditions [139], and precipitates cobalt hydroxide carbonate on the surface of immersed pellet,

$$\begin{aligned} &H_2NCONH_2 + CoF_x^{(x-2)^-} + yOH^- + (n+2)H_2O \rightarrow \\ &2NH_4^+ + 0.5yCO_3^{2-} + xF^- + Co(OH)_y(CO_3)_{1-0.5y} \cdot nH_2O \end{aligned} \qquad (4-2)$$

The micromorphology of precursor precipitated on the LSCF-GDC pellet is shown in Figure 4.1. Obviously, 1-D array of spring onion-like clusters with an average size of 10 μm was deposited on the substrate. The clusters are composed of several smaller clusters with an average size of 5 μm that bundled up while growing in different directions from the same middle nucleation sites. Each unit cluster consists of a relatively high density of nanosized spikes (~50 nm in diameter) well-aligned as demonstrated in Figure 4.1b. From Figure 4.1c and Figure 4.1d, it can be seen that cobalt precursor is bonded to the substrate very well.

After sintered at 900 °C in air for 3 hours, the cobalt hydroxide carbonate precursor on LSCF-GDC pellet surface would be converted into cobalt oxide through thermal decomposition process (4-3),

$$\begin{aligned} &3Co(OH)_y(CO_3)_{1-0.5y} \cdot nH_2O + 0.5O_2 \rightarrow \\ &Co_3O_4 + (3n+1.5y)H_2O + (3-1.5y)CO_2 \end{aligned} \qquad (4-3)$$

Figure 4.2 shows XRD patterns of the LSCF-GDC pellet treated through above hydrothermal and sintering process. All the diffraction peaks were perfectly assigned to GDC fluorite, LSCF perovskite and Co_3O_4 spinel (i.e., $CoCo_2O_4$) phases, respectively. No

secondary impurity phases could be found. To a large extent, these results validated the assumed reactions of (4-2) and (4-3).

Figure 4.3 shows the SEM images of surface modified membrane after heat treatment at 900 °C in air for 3 h. The micromorphology after the heat treatment is quite similar to that before the treatment, particularly the micromorphology of nanoclusters. This observation indicates that the surface micromorphology has reasonably good thermal stability. It is not surprising to see obvious changes of surface microstructures. In particular, the nanosized spikes with sharp tips in the nanocluster precursor (Figure 4.1) were changed into nanorods (Figure 4.3). The nanorod is composed of Co_3O_4 nanoparticles connected in series very uniformly. Obviously, such a microstructure will significantly enhance the effective surface area for oxygen reduction and oxygen evolution reactions, therefore the related device performance.

4.3.2 Oxygen permeation performance

Oxygen permeation performance of the fabricated membranes was measured in the temperature range of 800-900 ºC and the sweep argon flow rate of 80 $mL \cdot min^{-1}$ was used. As shown in Figure 4.4a, oxygen permeation flux increases with increasing operating temperature, indicating the thermal activation nature of the process. For a given operating temperature, the blank membrane shows the lowest performance while the membrane with nanostructured Co_3O_4 surface only at the feed side (simply denoted as M-FS) demonstrates the highest performance, the performance of the membrane with nanostructured Co_3O_4 surface only at the permeate side (simply denoted as M-PS) is in between. In particular, the oxygen permeation flux of the M-FS reached 0.57, 0.64, and 0.73 $mL \cdot cm^{-2} \cdot min^{-1}$ at 800, 850, and 900 °C, respectively. These performances are 10 ~ 2.9 times those of the

blank membrane, and 2.9 ~ 1.3 times those of the M-PS under the same operating conditions. Since the thickness of the dense part is the same for these membranes, the enhancement of oxygen permeation performance is attributed to the surface modification by nanostructured Co_3O_4. It is reasonable to assume that nanostructured Co_3O_4 surface improves surface exchange process, including ORR and/or OER process. As mentioned above, the oxygen permeation flux of the M-FS is higher than that of the M-PS under the same operating conditions, indicating that the surface modification at the feed side is more effective than the permeate side in enhancing the membrane performance. This result implies that the ORR at the feed side is a major step limiting oxygen permeation process. Figure 4.4b shows the corresponding Arrhenius plots of three types of membranes. The activation energy of the blank membrane derived from the Arrhenius plot is 171.29 $KJ \cdot mol^{-1}$. However, those of the M-PS and M-FS are only 109.12 and 25.22 $KJ \cdot mol^{-1}$, respectively. These results are consistent with the oxygen permeation performance in Figure 4.4a, further confirming that the surface modification with nanostructured Co_3O_4 can effectively improve oxygen permeation performance of the membrane.

Figure 4.5 shows the effect of argon sweep gas flow rate on oxygen permeation performance of the membranes at 900 °C. With increasing the sweep gas flow rate from 10 to 80 $mL \cdot min^{-1}$, the oxygen permeation flux increased for all three types of membranes. In fact, the increase of sweep gas flow rate decreases oxygen partial pressure at the permeate side. This in turn increases chemical potentials for oxygen permeation process, and therefore the membrane performance. This result also implies that the surface exchange at the permeate side is a limiting step in oxygen permeation process. Although the performance of all the three membranes was improved upon increasing the sweep gas flow

rate, the effects on the M-FS and M-PS were more pronounced than the blank membrane, especially at high sweep gas flow rates.

4.3.3 Electrochemical characterization

The measurement results of above membranes clearly indicate that nanostructured Co_3O_4 surface can significantly improve oxygen permeation performance. To further understand the fundamental mechanism of surface modification on performance enhancement, a systematic electrochemical measurement is conducted using symmetric cells and electrochemical impedance spectra (EIS) technique. The symmetrical cells are GDC electrolyte-supported with the configurations of GDC-LSCF/GDC/GDC-LSCF and nano-Co_3O_4/GDC-LSCF/GDC/GDC-LSCF/nano-Co_3O_4. The measurements were conducted in different operating conditions, including oxygen partial pressure, temperature, and current load. Surface exchange process involves very complicated elementary reaction steps. The characteristics of these reaction steps determine the polarization resistance of symmetric cells. The oxygen partial pressure applied on symmetric cell directly affects every single reaction step and therefore the polarization resistance. Theoretically, the relationship between oxygen partial pressure and polarization resistance can be described as[140]:

$$\frac{1}{R} \propto P_{O_2}^{m} \qquad (4-4)$$

where R is the polarization resistance, P_{O_2} the applied oxygen partial pressure, and m the reaction order. The value of reaction order m is an indicator linking surface reaction steps in ORRs. In particular, the m values of 1, 0.5, 0.25 are associated with dissociative

adsorption of oxygen molecule ($O_{2,g} \leftrightarrow 2O_{ad}$), surface diffusion ($O_{ad} \leftrightarrow O_{TPB}$) and charge transfer reaction ($O_{ad} + 2e' + V_O^{\cdot\cdot} \longrightarrow O_O^{\times}$ or $O_{ad} + V_O^{\cdot\cdot} \longrightarrow O_O^{\times} + 2h^{\cdot}$), respectively.

Figure 4.6 shows the typical EIS of symmetric cells measured at 800 °C under different oxygen partial pressures. An equivalent circuit with the configuration in Figure 4.6a (the inset figure) is used to fit the measured EIS data. Here, the L1 is the inductance of the measurement circuit, R1 is the resistance induced primarily by the electrolyte and lead wires. R2 and R3 are polarization resistance, while Q1 and Q2 are constant phase elements of the corresponding process. The overall polarization resistance is then obtained by adding R2 and R3 together, and the polarization resistance (R_p) of one electrode is obtained by dividing the overall polarization resistance by two. As shown in Figure 4.6, a good agreement is obtained between the fitting curve (solid line) and the experimental data (scattered dots). The EIS measurements of the symmetric cells were also conducted at 850 and 900 °C under different oxygen partial pressures (the results are not shown here). The experimental EIS data was curve-fitted using the same equivalent circuit as mentioned above and the polarization resistances of the electrode were then obtained under these operating conditions. The results indicate that the polarization resistance decreased with increasing temperature, indicating the thermally activated electrode process. The polarization resistance also decreased with increasing the applied oxygen partial pressure, further confirming the strong correlation between the electrode process and the applied oxygen partial pressure. It is clearly shown that the polarization resistance of the symmetric cell modified with Co_3O_4 nanostructured surface is much smaller than the blank symmetric cell under the same operating conditions. For example, the R_p of the blank symmetric cell is 0.16 Ω·cm^2 under 1.0 atm at 900 °C while that of the symmetric cell with surface

modification is only 0.008 $\Omega \cdot cm^2$ under the same operating condition. These results further verify that the Co_3O_4 nanostructured surface may significantly improve surface exchange properties.

To further identify the surface exchange processes, the correlation between electrode polarization resistance and the applied oxygen partial pressure was obtained at different temperatures and shown in Figure 4.7. The reaction order m values as the slopes of the correlation curves were also obtained and shown in the same Figure. For the blank symmetric cell, the reaction order of 0.35 was obtained at 800 °C, suggesting that the surface exchange process could be limited by the combinational steps of both surface diffusion and charge transfer. With increasing the temperature to 850 and 900 °C, the reaction order was changed to 0.44 and 0.53 respectively, implying that the surface diffusion step became increasingly dominating. As mentioned before, the charge transfer process is thermally activated in nature. Accordingly, high temperatures facilitate charge transfer process. This could be the reason that the limiting steps evolved from the combination of surface diffusion and charge transfer to the surface diffusion with increasing temperatures. In comparison, the reaction order of 0.54 was obtained at 800 °C for the surface modified symmetric cell. This is close to the theoretical result of 0.5, indicating that the surface exchange process was dominated by the surface diffusion step. With increasing temperature to 850 and 900 °C, the reaction order was changed to 1.10 and 1.18 respectively, suggesting that the surface exchange process was primarily limited by dissociative adsorption step. It is reasonable to assume that the effective area of Co_3O_4 nanostructured surface is much larger than that of the blank symmetric cell surface. The increased active reaction area promotes the surface diffusion of adsorbed oxygen to the

triple phase boundary (TPB), therefore the diffusion reaction is no longer the limiting step for the device with Co_3O_4 nanostructured surface.

Depending on the specific operating conditions, the surface exchange involved in electrodes could be OER or ORR process. To understand the surface exchange mechanism under the individual mode of OER and ORR, three-electrode configuration was employed. Figure 4.8 shows the schematic illustration of three-electrode configuration. The electrodes of symmetric cells are used as working electrode and counter electrode respectively. The circumference of electrolyte coated with silver paste serves as the reference electrode. When a negative voltage is applied from working electrode to counter electrode (Figure 4.8a), the ORR process takes place at the working electrode. By measuring EIS response between the reference electrode and working electrode, the ORR behavior in the working electrode can be obtained. Similarly, when a positive voltage is applied from working electrode to counter electrode (Figure 4.8b), OER process will occur in the working electrode, and the EIS response between the working and reference electrode can be used to identify the OER behavior.

Figure 4.9 shows the polarization resistance (R_p) of working electrode under different current load conditions. In the ORR mode (Figure 4.9a), the R_p decreases with increasing the magnitude of current load, implying that current load applied on the working electrode facilitates the activation process for ORRs. The R_p also decreases with increasing operating temperature from 800 to 900 °C, indicating the thermally activated nature of ORRs with the electrode. It can be observed that the R_p of the working electrode with Co_3O_4 nanostructured surface is much lower than that without the nanostructured surface, further confirming that the nanostructured surface can significantly improve ORRs. In the

OER mode (Figure 4.9b), the R_p decreases with increasing the operating temperature from 800 to 900 °C. The R_p also decreases with increasing the applied current load. The R_p of the working electrode with Co_3O_4 nanostructured surface is much lower than that without the nanostructured surface. The comparison of ORR and OER mode indicates that the R_p of the working electrode shows similar variation trends under the same operating conditions. It can also be observed that the R_p of working electrode decreases more pronouncedly in ORR mode than OER mode when the current load is increased, implying that the activation process with load current is more effective in ORR than in OER.

A short-term stability of the symmetric cell with nanostructured Co_3O_4 surfaces was also conducted in air at 900 °C for about 100 h. The EIS of the cell was collected during the testing course, where the EIS data was collected every 1 h in daytime and no data collection was performed in the nighttime. The time history of EIS is shown in Figure 4.10. During the first 80 hrs., the polarization resistance demonstrated asymptotic increase from 0.0875 to 0.1 $\Omega \cdot cm^2$. Beyond 80 hrs., the polarization resistance was stabilized at 0.1 $\Omega \cdot cm^2$. The post-test characterization of the symmetric cell shows that the nanostructured Co_3O_4 layer was attached to the LSCF-GDC electrode very well (Figure 4.11a), however, surface Co_3O_4 nanorods formed at the fabrication stage (Figure 4.3) were obviously agglomerated (Figure 4.11b). The agglomerated Co_3O_4 layer decreases the effective area for surface exchange reactions. This could be the reason that the polarization resistance was increased in the first 80 hrs. The stable polarization resistance after the 80 hours verified that the microstructure of the surface Co_3O_4 layer was stabilized after the short-term stability test.

4.4 Conclusion

The dual phase GDC-LSCF membrane and GDC electrolyte-supported symmetric cell GDC-LSCF/GDC/GDC-LSCF were prepared, built upon which Co_3O_4 nanorod-structured surface layers were successfully synthesized and fabricated by hydrothermal process. The electrochemical performance and stability were comprehensively evaluated using the prepared devices. The nanostructured Co_3O_4 surfaces may enhance oxygen permeation performance at different degrees due to the excellent catalytic property and increased effective surface area of Co_3O_4 nanorod cluster. The performance improvement with nanostructured surface at the feeding side is more prominent than the permeate side, indicating the ORRs at the feeding side is a major limiting step for oxygen permeation. The electrochemical performance tests with symmetric cell and EIS technique indicate that the nanostructured Co_3O_4 surfaces may also significantly reduce the polarization resistance. The reaction order analysis shows that the limiting step of surface exchange process is the combination of surface diffusion and charge transfer at relatively low temperature condition for the symmetric cell without nanostructured surface but changes to the surface diffusion step at relatively high temperatures due to the thermal activation nature of charge transport process. With the nanostructured surface, the surface exchange process is limited by surface diffusion and increasingly dominated by dissociative adsorption step at relatively high temperatures. The three-electrode configuration test results indicate that the surface exchange processes of both ORRs and OERs are thermally activated nature and facilitated by the applied current loads. Under the same operating conditions, e.g., the temperature, the magnitude of current load, the electrode polarization resistance in ORR mode is larger than that in OER mode. In both ORR and OER mode, the polarization

resistance of working electrode with nanostructured surface is lower than that without nanostructured surface. The short-term stability test shows that the degradation of electrode performance occurs due to the agglomerations of the surface nanorod clusters in the first period of testing time. Beyond this time, the electrode performance becomes stable and the surface nanorod clusters are stabilized to microscale clusters.

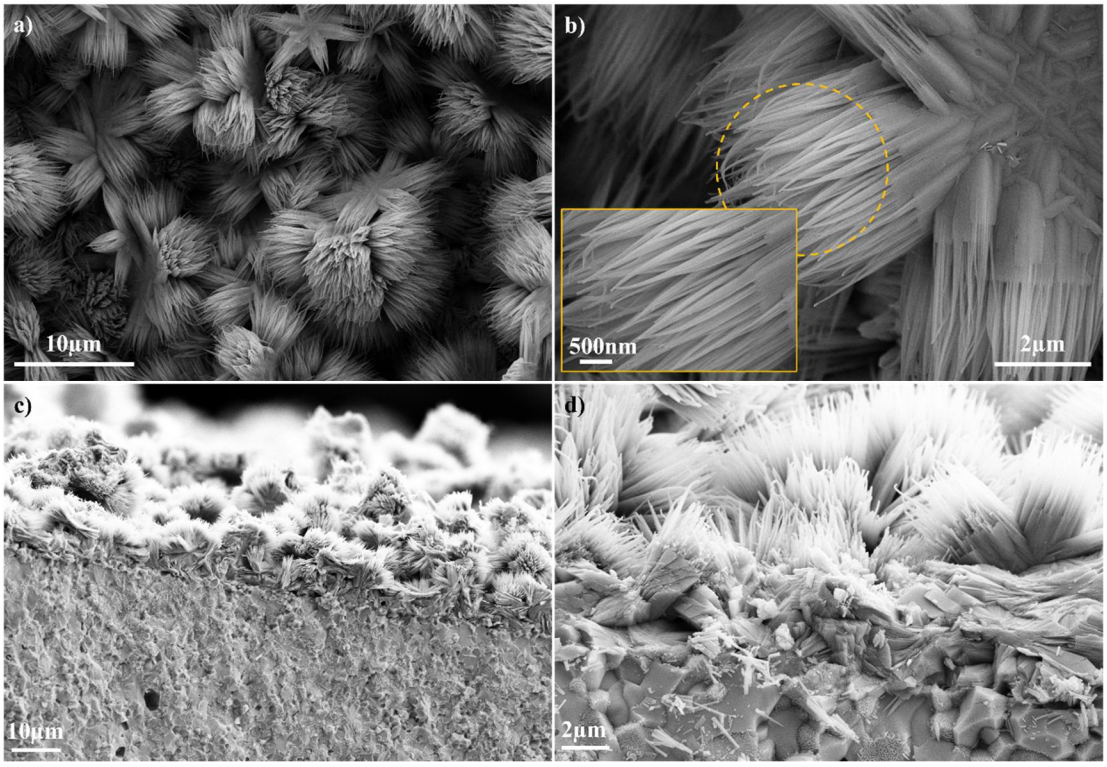

Figure 4.1 SEM image of the precursors of Co_3O_4 nanorod catalysts grown on the GDC-LSCF membrane. **a)** surface morphology; **b)** enlarged picture of surface morphology; **c)** cross sectional view; **d)** enlarged picture of cross section.

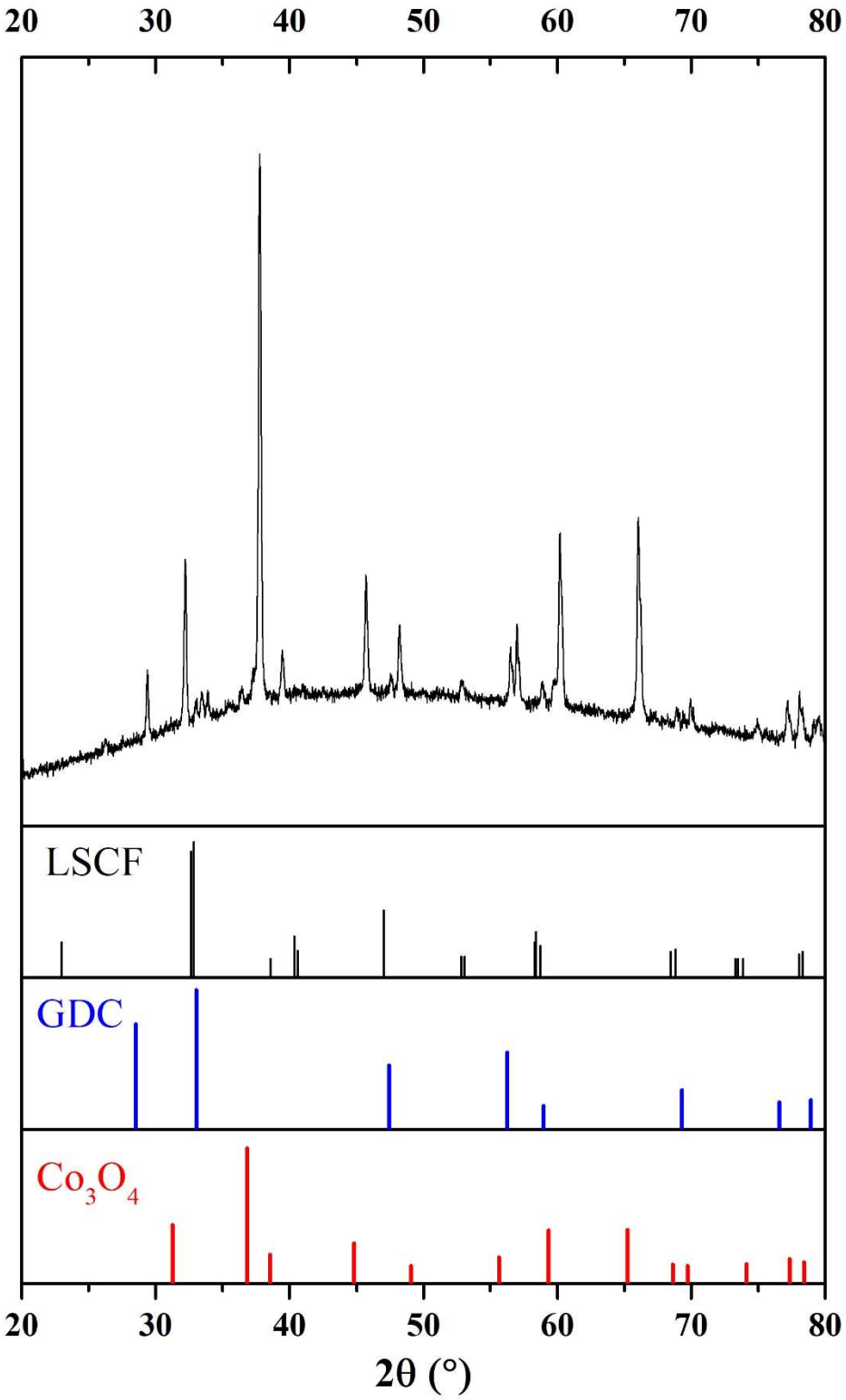

Figure 4.2 XRD patterns of the GDC-LSCF membrane modified with Co_3O_4 nanorod catalysts

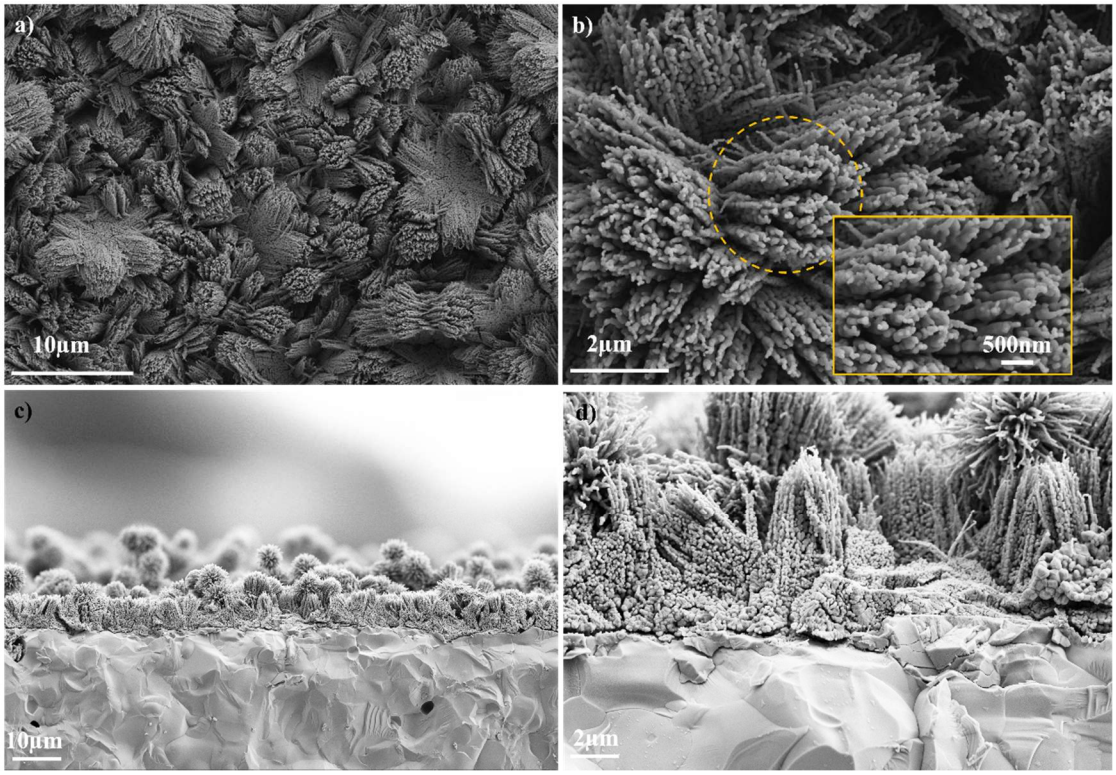

Figure 4.3 SEM image of the Co_3O_4 nanorod catalysts grown on the GDC-LSCF membrane after calcination at 900 °C in air for 3h. **(a)** surface morphology; **(b)** enlarged picture of surface morphology; **(c)** cross sectional view; **(d)** enlarged picture of cross section.

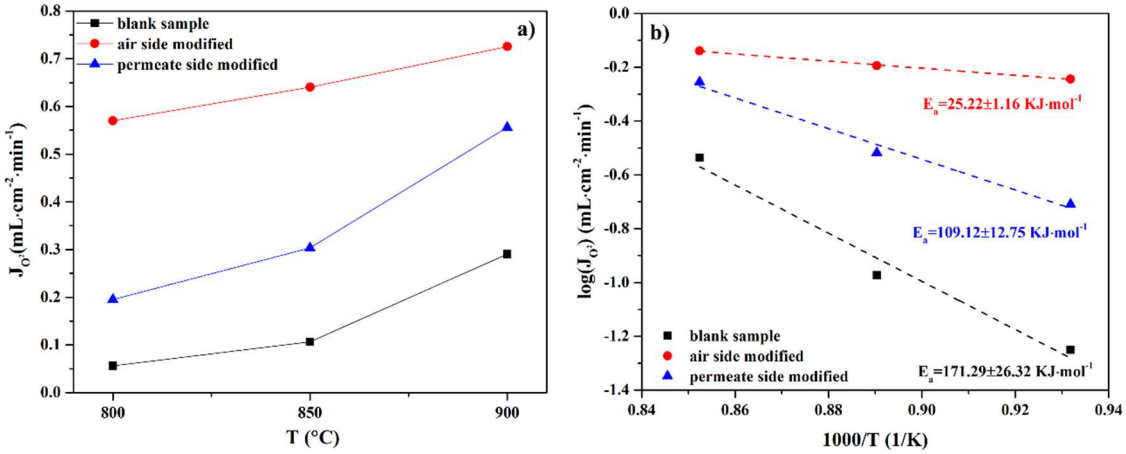

Figure 4.4 **(a)** Oxygen flux of three types of membrane tested at different temperatures and **(b)** corresponding Arrhenius plots.

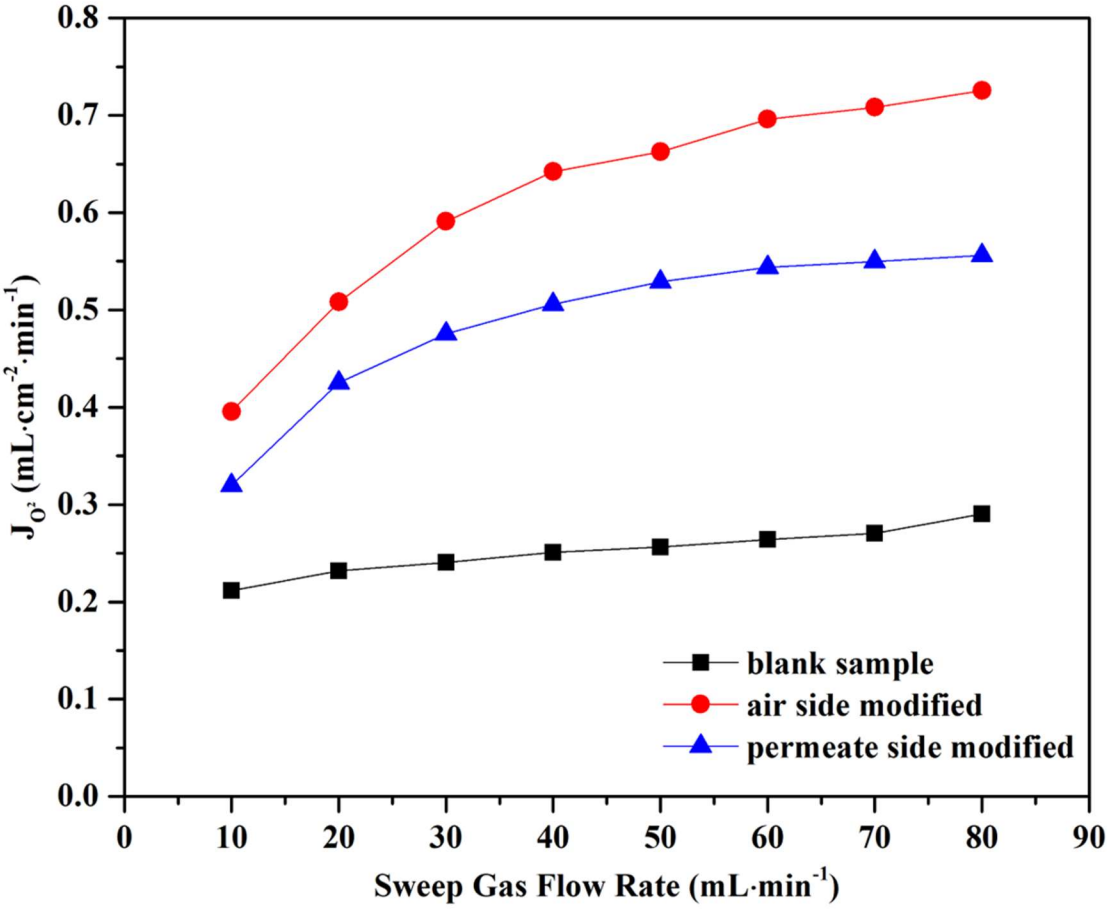

Figure 4.5 Effects of sweep gas flow rates on oxygen permeation flux at 900 °C through all types of membrane.

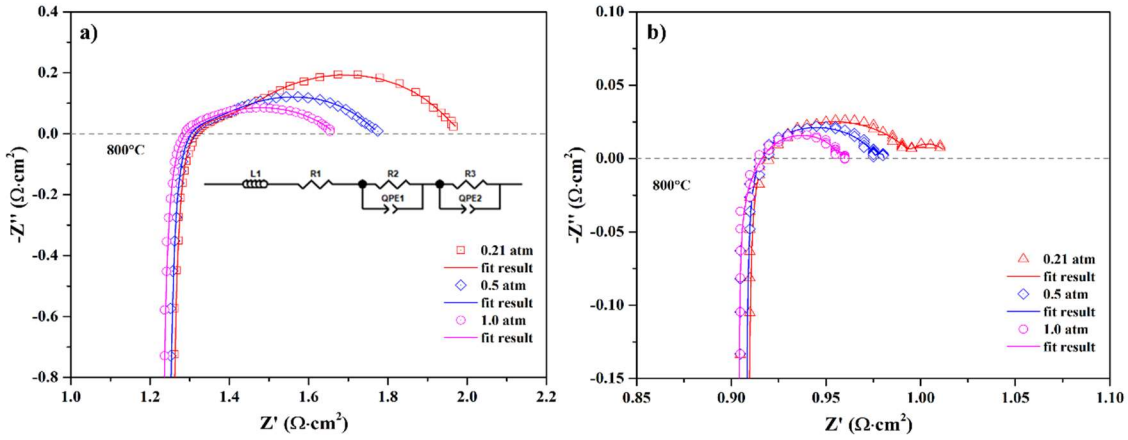

Figure 4.6 EIS spectra of symmetric cells tested at 800 °C under different oxygen partial pressure. **a)** blank symmetric cell; **b)** surface modified symmetric cell.

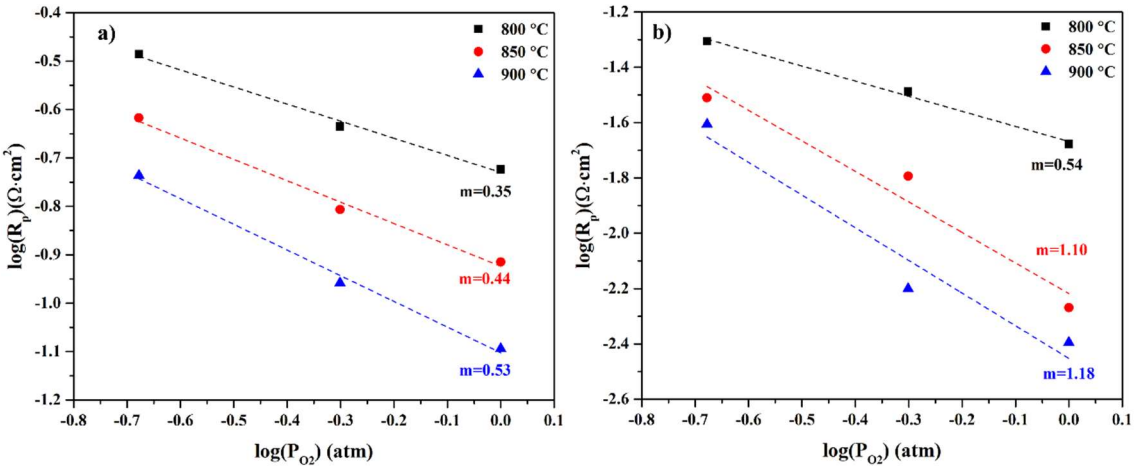

Figure 4.7 Correlation between polarization resistance and oxygen partial pressure at different temperatures and corresponding reaction orders. **a)** blank symmetric cell; **b)** surface modified symmetric cell.

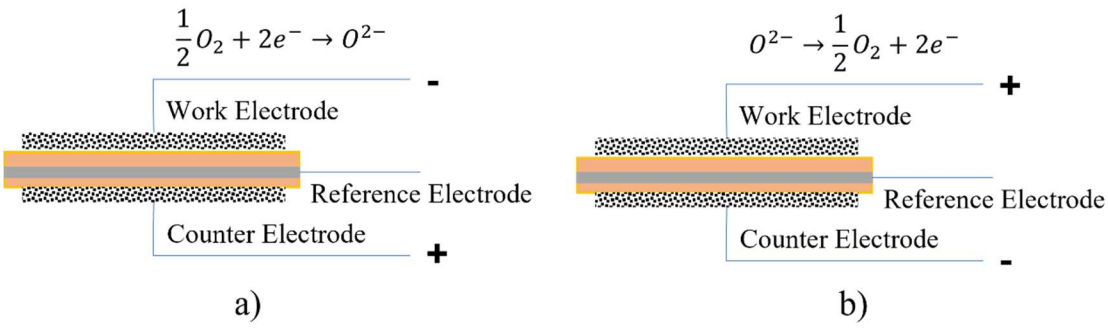

Figure 4.8 Electrochemical Impedance Spectrum tests on symmetric cells with three electrodes for **a)** ORR and **b)** OER process.

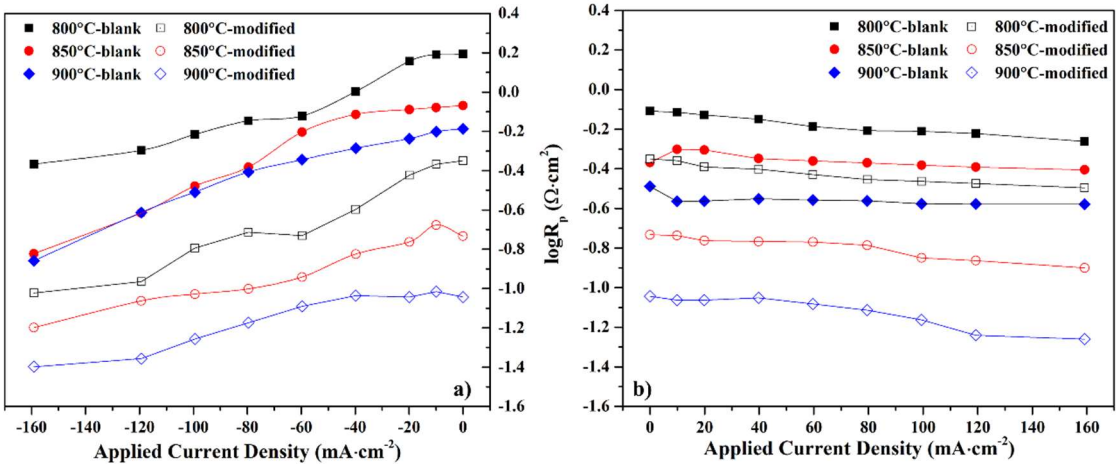

Figure 4.9 Effect of current density on **a)** ORR-Rp and **b)** OER-Rp measured from symmetric cells with three electrode configurations.

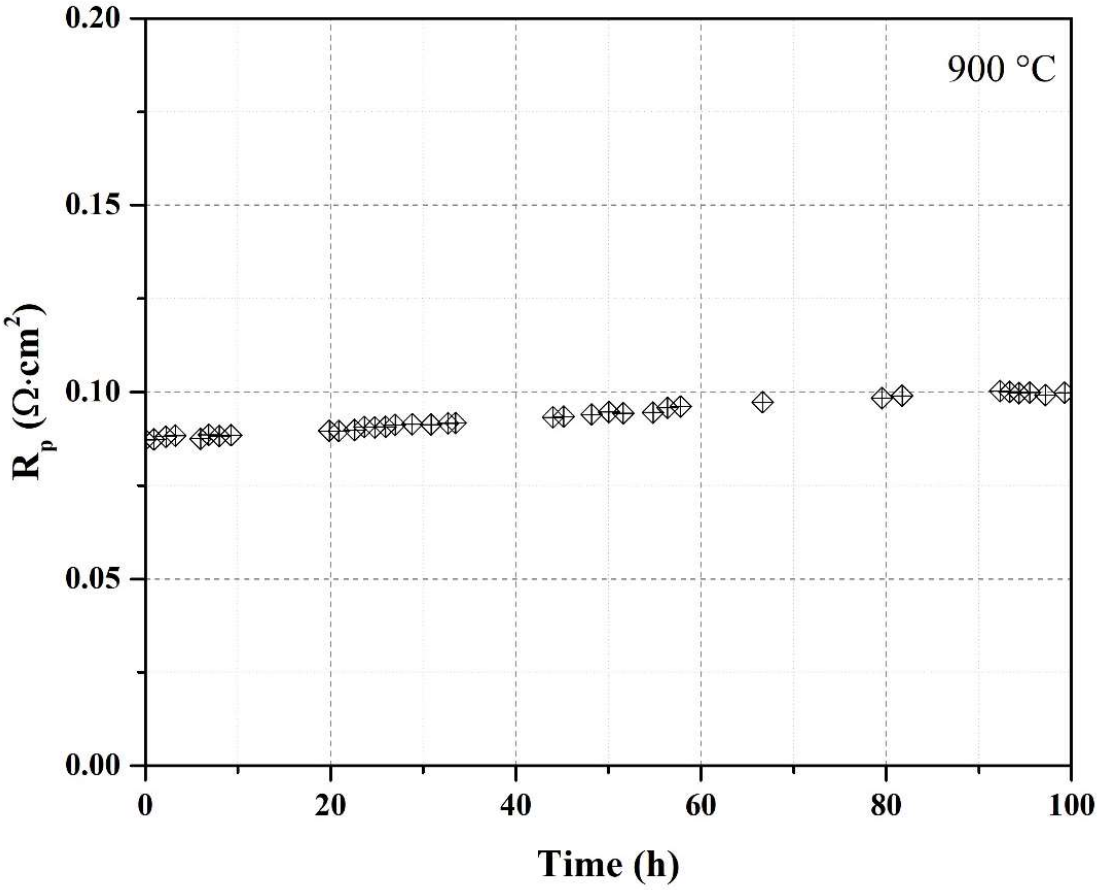

Figure 4.10 Time history of polarization resistances of the symmetric cell with nanostructured surface Co_3O_4/GDC-LSCF/GDC/GDC-LSCF/Co_3O_4 tested in air at 900 °C.

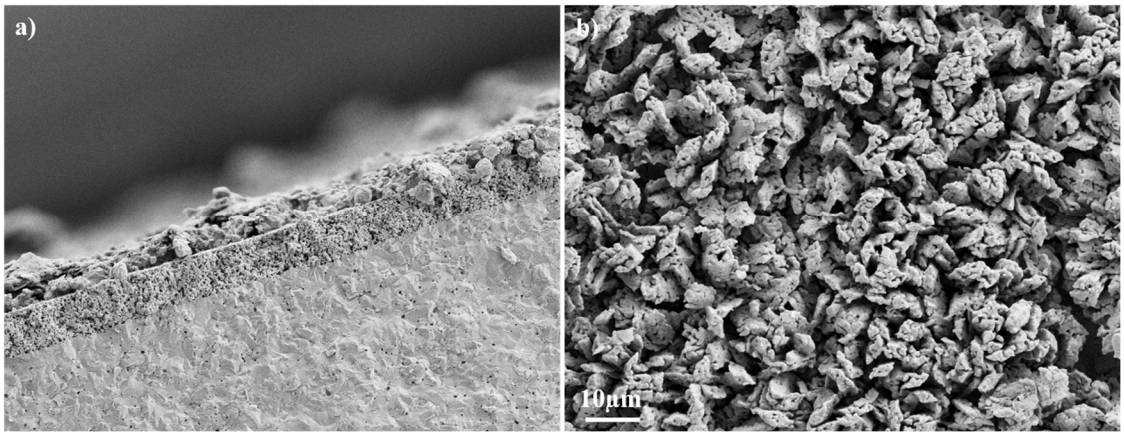

Figure 4.11 SEM of the symmetric cell with nanostructured surfaces after testing in air at 900 ºC for 100h. **a)** cross-section; **b)** top view.

CHAPTER 5

SUMMARY

The research in cutting down greenhouse gas emission and promote its capture is of practical significance in addressing the deteriorating environmental issue. Ceramic oxygen permeation membrane (OPM) which employs MIEC materials to directly separate oxygen from air has attracted considerable attention for its simple, cost-effective operation mode, and has become one of the key technologies within clean combustion based energy generation when utilized in integrated gasification combined cycle (IGCC), decarbonized fuel, oxygen enrichment, oxyfuel, gas to liquid etc. However, the current membrane materials are either with high permeabilities yet poor stabilities or with robust durability while low oxygen permeation flux. The tradeoff effect of materials greatly hinders the wide application of oxygen permeation membrane. Solid oxide cell (SOC), a type of energy device integrates two reverse operation modes, i.e., solid oxide fuel cell (SOFC) and solid oxide electrolyzer (SOEC), within one setup. The SOFC operation mode is able to convert chemical energy in fuels into electrical energy directly in a highly efficient and environmental manner. While hydrogen- and/or carbon monoxide-rich syngas could be generate using electricity, water , and/or carbon dioxide through SOEC operation. The combination of SOFC and SOEC would create a carbon neutral technology for clean energy conversions. However, the problems related to materials become more complicated for SOC due to more complex components, for example the high resistance of electrolyte, carbon accumulation over nickel fuel electrode, performance rapid degradation in air

electrode etc. It is known that the performance of a device not only depends on the materials it used, but the microstructure or design also plays an prominent role. A prime design with superior microstructure could exploit the potential of current material system and seems to be more practical strategies in upscaling these technologies at present.

Planar and tubular designs are widely used configurations in OPM and SOC. The planar design is easy at manufacturing but bring up sealing problems due to relatively long sealing length. The tubular design demonstrates advantages of short sealing length and good thermal shock resistance, especially micro-tubular hollow fibers may effectively increase volumetric density of oxygen permeation flux, power output or current efficiency. However, challenges on manufacturing process of the tubular design remains, particularly the microtubular type where the diameter is relatively small. In the past few years, the slurry spinneret technology in combination with phase inversion method has been successfully developed to fabricate hollow fiber membranes The early-stage hollow fiber membrane usually employs homogeneous material and tap water is used at both inner and outer of spinneret head to form green hollow fibers. After sinter processing, the resultant hollow fiber membrane demonstrates the feature of multiple-layered microstructures: a sponge-like layer in the middle is sandwiched by radially aligned finger-like pore layer on either side, and the shell and lumen sides are covered by relatively dense thin skin layers. One can create only one finger-like pore layer located either close to the shell side or to the lumen side by adjusting the parameters of spinning procedure.

The performance of electrolyte-supported SOC is primarily limited due to large ohmic resistance introduced by thick electrolyte for sufficient supporting strength. While the high sintering temperature required to densify the electrolyte of electrode-supported

SOC could destroy the porous microstructure of electrodes, therefore a great loss of electrode porosity and increased concentration polarization resistance. Therefore, Ni-cermet is still widely used as fuel electrode of SOC although MIEC perovskites have demonstrate advantages over it. Perovskite fuel electrode-supported designs are rarely studied particularly for microtubular SOCs. $(La_{0.3}Sr_{0.7})_{0.9}Ti_{0.9}Ni_{0.1}O_{3-\delta}$-$Sm_{0.2}Ce_{0.8}O_{1.9}$ (LSTN-SDC) electrode-supported microtubular cell LSTN-SDC/YSZ/$(La_{0.8}Sr_{0.2})_{0.95}MnO_{3-\delta}$ is therefore fabricated and characterized. The LSTN-SDC microtubular substrate demonstrates a microstructure with radially well-aligned microchannels open at the inner surface using an in-house built spinneret extrusion system in combination with modified phase inversion method. The finger like microchannel preserved within in the electrode substrate after being sintered at relative high temperature which facilitate the gas diffusion in the fuel electrode. What's more, nickel is exsolved from LSTN grains and uniformly decorated onto grain surface as Ni nanoparticles upon reducing treatment, and therefore on inner surface of microchannels in the substrate. The electrolysis process in combination with surface catalytic particle and nanostructured electrode substrate leads to highly efficient CO production from CO_2 with conversion efficiencies of well above 100%. The electrolysis also facilitates to regenerate surface catalytic functionality of nanostructured electrode substrate. The redox stability advantages of the cell are demonstrated in both alternative reduction (CO)/oxidation (air) atmospheric conditions and reversible operating mode.

Due to high surface area to volume ratio, hollow fiber membranes have been extensively investigated for oxygen separation applications. The widely studied hollow fiber membranes are fabricated using spinneret process in combination with phase

inversion method, followed by one-step high temperature sintering process. The resultant cross-sectional microstructure of the membrane is usually featured by multiple layers, where a relatively thick sponge-like layer is sandwiched by the layers of radially aligned closed finger-liked pores on either side, and the shell and lumen sides are covered by relatively dense thin skin layers. To take advantage of finger-like pores for facile gas diffusion, hollow fibers with open finger-like pores are created using spinneret process with modified phase inversion method, built upon which thin film dense separation layer and porous catalyst layer are fabricated to form an asymmetric membrane. The asymmetric design can reduce sintering temperature for membrane fabrication and enhance conductivity for bulk charge transport. However, the mechanical strength of the hollow fiber membranes is usually not sufficient and high-cost material is used for the substrate. In this paper, LSCF-ZnO composite hollow fiber is developed and optimized so that radially-aligned open microchannels are produced. Built upon the composite hollow fiber, thin film dense LSCF separation layer and porous LSCF catalyst layer are successfully fabricated. The performance and long-term stability of the membrane are systematically measured and characterized. Results indicate that ZnO addition to the hollow fiber substrate can not only decrease the sintering temperature for membrane fabrication but also significantly enhance the mechanical strength, robustness, durability, and stability. By replacing a considerable amount of high cost LSCF with low cost ZnO in the substrate, the capital cost of the membrane can also be significantly reduced.

The oxygen permeation performance of dual phase membrane GDC-LSCF is greatly constrained by its limited catalytic capacity toward surface oxygen reduction and/or oxygen evolution reaction process. Loading highly catalytic Co_3O_4 nanorods onto the

surface of GDC-LSCF membrane by hydrothermal process noticeably promote the oxygen permeation. The oxygen permeation of membrane with surface modification on air side reaches 0.73 $mL \cdot cm^{-2} \cdot min^{-1}$ at 900 °C which is 2.5 times higher than that of membrane without surface modification under the same operating conditions. The influence of modification is also found to have a greater influence on ORR process than OER process as the Co_3O_4 nanoarray coated onto the air side produce higher oxygen permeation flux and smaller polarization resistance compared to membrane coated onto permeation side. The thermal stability of nanoarray modified membrane is acceptable with minor degradation of polarization resistance after 100 h of operation at 900 °C.

The dissertation has successfully fabricated and characterized micro/nano-structured ceramic device for energy conversion. The performance is greatly enhanced and a relative stability is obtained during long term operation. The fabrication method should provide a promising insight along with the development of novel materials.

REFERENCES

1. F. Drake, *Global warming*, Routledge (2014).

2. R. K. Pachauri, M. R. Allen, V. R. Barros, J. Broome, W. Cramer, R. Christ, J. A. Church, L. Clarke, Q. Dahe and P. Dasgupta, *Climate change 2014: synthesis report. Contribution of Working Groups I, II and III to the fifth assessment report of the Intergovernmental Panel on Climate Change*, Ipcc (2014).

3. J. Rogelj, M. Den Elzen, N. Höhne, T. Fransen, H. Fekete, H. Winkler, R. Schaeffer, F. Sha, K. Riahi and M. Meinshausen, *Nature*, **534**, 631 (2016).

4. R. Kneer, D. Toporov, M. Förster, D. Christ, C. Broeckmann, E. Pfaff, M. Zwick, S. Engels and M. Modigell, *Energy & Environmental Science*, **3**, 198 (2010).

5. M. Habib, H. Badr, S. Ahmed, R. Ben-Mansour, K. Mezghani, S. Imashuku, G. la O', Y. Shao-Horn, N. Mancini and A. Mitsos, *International Journal of Energy Research*, **35**, 741 (2011).

6. K. Zhang, J. Sunarso, Z. Shao, W. Zhou, C. Sun, S. Wang and S. Liu, *RSC Advances*, **1**, 1661 (2011).

7. Y. Teraoka, H.-M. Zhang, S. Furukawa and N. Yamazoe, *Chemistry Letters*, **14**, 1743 (1985).

8. A. Leo, S. Liu and J. C. D. da Costa, *International Journal of Greenhouse Gas Control*, **3**, 357 (2009).

9. C. Zhang, J. Sunarso and S. Liu, *Chemical Society Reviews*, **46**, 2941 (2017).

10. J. Sunarso, S. Baumann, J. Serra, W. Meulenberg, S. Liu, Y. Lin and J. D. Da Costa, *Journal of membrane science*, **320**, 13 (2008).

11. C. Wagner, *Progress in Solid State Chemistry*, **10**, 3 (1975).

12. A. J. Burggraaf and L. Cot, *Fundamentals of inorganic membrane science and technology*, Elsevier (1996).

13. N. Q. Minh, *Solid State Ionics*, **174**, 271 (2004).

14. R. M. Ormerod, *Chemical Society Reviews*, **32**, 17 (2003).

15. L. Yang, S. Wang, K. Blinn, M. Liu, Z. Liu, Z. Cheng and M. Liu, *Science*, **326**, 126 (2009).

16. Z. Zhan and S. A. Barnett, *Science*, **308**, 844 (2005).17. M. Torrell, S. García-Rodríguez, A. Morata, G. Penelas and A. Tarancón, *Faraday discussions*, **182**, 241 (2015).

18. K. Xie, Y. Zhang, G. Meng and J. T. Irvine, *Energy & Environmental Science*, **4**, 2218 (2011).

19. G. B. Sanders, A. Paz, L. Oryshchyn, K. Araghi, A. Muscatello, D. L. Linne, J. E. Kleinhenz and T. Peters, in *AIAA SPACE 2015 Conference and Exposition*, p. 4458 (2015).

20. J. E. Kleinhenz and A. Paz, in *10th Symposium on Space Resource Utilization*, p. 0423 (2017).

21. J. A. Hoffman, D. Rapp and M. Hecht, in *AIAA SPACE 2015 Conference and Exposition*, p. 4561 (2015).

22. K. E. Goodliff, P. Troutman, D. A. Craig, J. Caram and N. Herrmann, in *Aiaa Space 2016*, p. 5456 (2016).

23. M. A. Laguna-Bercero, *Journal of Power Sources*, **203**, 4 (2012).

24. A. Lashtabeg and S. J. Skinner, *J. Mater. Chem.*, **16**, 3161 (2006).

25. R. O'hayre, S.-W. Cha, W. Colella and F. B. Prinz, *Fuel cell fundamentals*, John Wiley & Sons (2016).

26. A. J. Bard, L. R. Faulkner, J. Leddy and C. G. Zoski, *Electrochemical methods: fundamentals and applications*, wiley New York (1980).

27. G. Chiodelli and L. Malavasi, *Ionics*, **19**, 1135 (2013).

28. X. Yang and J. T. Irvine, *Journal of Materials Chemistry*, **18**, 2349 (2008).

29. S. Liu, K. Li and R. Hughes, *Ceramics International*, **29**, 875 (2003).

30. H. P. Hsieh, *Catalysis Reviews*, **33**, 1 (1991).

31. L. W. McKeen, *Permeability properties of plastics and elastomers*, William Andrew (2016).

32. L. W. McKeen, in *Permeability Properties of Plastics and Elastomers (Fourth Edition)*, L. W. McKeen Editor, p. 61, William Andrew Publishing (2017).

33. *Encyclopedia of Life Support Systems (Eolss): v.1 : Desalination and Water Resources (Desware): Membrane Processes*, EOLSS Publishers Co Ltd., Oxford (2010).

34. W. contributors, Hollow fiber membrane, in, Wikipedia, The Free Encyclopedia.

35. J. Lewis, (2018).

36. L. K. Wang, J. P. Chen, Y.-T. Hung and N. K. Shammas, *Membrane and desalination technologies*, Springer (2008).

37. S. Benfer, U. Popp, H. Richter, C. Siewert and G. Tomandl, *Separation and Purification Technology*, **22-23**, 231 (2001).

38. Q. Wang, Z. Wang and Z. Wu, *Desalination*, **297**, 79 (2012).

39. C. Feng, K. C. Khulbe, T. Matsuura, R. Gopal, S. Kaur, S. Ramakrishna and M. Khayet, *Journal of Membrane Science*, **311**, 1 (2008).

40. L. Li, M. Chen, Y. Dong, X. Dong, S. Cerneaux, S. Hampshire, J. Cao, L. Zhu, Z. Zhu and J. Liu, *Journal of the European Ceramic Society*, **36**, 2057 (2016).

41. E. Drioli and L. Giorno, *Membrane operations: innovative separations and transformations*, John Wiley & Sons (2009).

42. S. Zare and A. Kargari, in *Emerging Technologies for Sustainable Desalination Handbook*, V. G. Gude Editor, p. 107, Butterworth-Heinemann (2018).

43. J. F. Kim, J. H. Kim, Y. M. Lee and E. Drioli, *AIChE Journal*, **62**, 461 (2016).

44. A. Venault, Y. Chang, D.-M. Wang and D. Bouyer, *Polymer Reviews*, **53**, 568 (2013).

45. M. K. Purkait, M. K. Sinha, P. Mondal and R. Singh, in *Interface Science and Technology*, M. K. Purkait, M. K. Sinha, P. Mondal and R. Singh Editors, p. 1, Elsevier (2018).

46. H. Strathmann, P. Scheible and R. W. Baker, *Journal of Applied Polymer Science*, **15**, 811 (1971).

47. Z. T. Wu, M. H. D. Othman, B. F. K. Kingsbury and K. Li, in *Advanced Membrane Science and Technology for Sustainable Energy and Environmental Applications*, A. Basile and S. P. Nunes Editors, p. 496, Woodhead Publishing (2011).

48. X. Tan and K. Li, in *Handbook of Membrane Reactors*, A. Basile Editor, p. 271, Woodhead Publishing (2013).

49. K. Li, X. Tan and Y. Liu, *Journal of membrane science*, **272**, 1 (2006).

50. W. Yin, B. Meng, X. Meng and X. Tan, *Journal of Alloys and Compounds*, **476**, 566 (2009).

51. T. He, M. Mulder, H. Strathmann and M. Wessling, *Journal of membrane science*, **207**, 143 (2002).

52. D. Wang, K. Li and W. Teo, *Journal of Membrane Science*, **166**, 31 (2000).

53. C. Cao, T.-S. Chung, S. B. Chen and Z. Dong, *Chemical engineering science*, **59**, 1053 (2004).

54. D. F. Li, T.-S. Chung, R. Wang and Y. Liu, *Journal of Membrane Science*, **198**, 211 (2002).

55. N. Widjojo, S. D. Zhang, T. S. Chung and Y. Liu, *Journal of Membrane Science*, **306**, 147 (2007).

56. J. Luyten, A. Buekenhoudt, W. Adriansens, J. Cooymans, H. Weyten, F. Servaes and R. Leysen, *Solid State Ionics*, **135**, 637 (2000).

57. X. Tan, Y. Liu and K. Li, *Industrial & Engineering Chemistry Research*, **44**, 61 (2005).

58. Z. Wang, N. Yang, B. Meng, X. Tan and K. Li, *Industrial & Engineering Chemistry Research*, **48**, 510 (2009).

59. Z. Wang, Y. Kathiraser, T. Soh and S. Kawi, *Journal of membrane science*, **465**, 151 (2014).

60. H. Liu, Z. Pang, X. Tan, Z. Shao, J. Sunarso, R. Ding and S. Liu, *Ceramics international*, **35**, 1435 (2009).

61. H. Liu, X. Tan, Z. Pang, J. D. Da Costa, G. Q. Lu and S. Liu, *Separation and purification technology*, **63**, 243 (2008).

62. D. Han, J. Sunarso, X. Tan, Z. Yan, L. Liu and S. Liu, *Energy & fuels*, **26**, 4728 (2012).

63. T. Schiestel, M. Kilgus, S. Peter, K. J. Caspary, H. Wang and J. Caro, *Journal of Membrane Science*, **258**, 1 (2005).

64. H. Wang, C. Tablet and J. Caro, *Journal of Membrane Science*, **322**, 214 (2008).

65. H. Wang, T. Schiestel, C. Tablet, M. Schroeder and J. Caro, *Solid State Ionics*, **177**, 2255 (2006).

66. A. Leo, S. Liu and J. C. D. da Costa, *Journal of Membrane Science*, **340**, 148 (2009).

67. S. Liu and G. R. Gavalas, *J. Membr. Sci.*, **246**, 103 (2005).

68. A. Leo, S. Liu and J. C. D. da Costa, *Separation and purification technology*, **78**, 220 (2011).

69. S. Liu, X. Tan, Z. Shao and J. Diniz da Costa, *AIChE journal*, **52**, 3452 (2006).

70. S. Liu and G. R. Gavalas, *Industrial & engineering chemistry research*, **44**, 7633 (2005).

71. T.-f. Tian, W. Li, T. Liu and C.-s. Chen, *Solid State Ionics*, **225**, 690 (2012).

72. J.-j. Liu, T. Liu, W.-d. Wang, J.-f. Gao and C.-s. Chen, *Journal of Membrane Science*, **389**, 435 (2012).

73. W. Li, J.-J. Liu and C.-S. Chen, *Journal of Membrane Science*, **340**, 266 (2009).

74. X. Bi, X. Meng, P. Liu, N. Yang, Z. Zhu, R. Ran and S. Liu, *J. Membr. Sci.*, **522**, 91 (2017).

75. W. Li, T.-F. Tian, F.-Y. Shi, Y.-S. Wang and C.-S. Chen, *Industrial & engineering chemistry research*, **48**, 5789 (2009).

76. J. Zhu, Z. Dong, Z. Liu, K. Zhang, G. Zhang and W. Jin, *AIChE Journal*, **60**, 1969 (2014).

77. T. Wang, Z. Liu, X. Xu, J. Zhu, G. Zhang and W. Jin, *Journal of Membrane Science*, **595**, 117600 (2020).

78. J. Song, B. Feng, X. Tan, N. Han, J. Sunarso and S. Liu, *Journal of Membrane Science*, **581**, 393 (2019).

79. M. H. D. Othman, N. Droushiotis, Z. Wu, G. Kelsall and K. Li, *Advanced Materials*, **23**, 2480 (2011).

80. N. Droushiotis, U. Doraswami, D. Ivey, M. H. D. Othman, K. Li and G. Kelsall, *Electrochemistry Communications*, **12**, 792 (2010).

81. T. Li, Z. Wu and K. Li, *Journal of membrane science*, **449**, 1 (2014).

82. X. Meng, W. Yan, N. Yang, X. Tan and S. Liu, *Journal of Power Sources*, **275**, 362 (2015).

83. N. Yang, X. Tan, Z. Ma and A. Thursfield, *Journal of the American Ceramic Society*, **92**, 2544 (2009).

84. C. Chen, M. Liu, L. Yang and M. Liu, *international journal of hydrogen energy*, **36**, 5604 (2011).

85. C. C. Wei and K. Li, *Industrial & engineering chemistry research*, **47**, 1506 (2008).

86. T. Liu, C. Ren, S. Fang, Y. Wang and F. Chen, *ACS applied materials & interfaces*, **6**, 18853 (2014).

87. N. Droushiotis, M. H. D. Othman, U. Doraswami, Z. Wu, G. Kelsall and K. Li, *Electrochemistry Communications*, **11**, 1799 (2009).

88. M. H. D. Othman, N. Droushiotis, Z. Wu, G. Kelsall and K. Li, *Journal of Power Sources*, **196**, 5035 (2011).

89. C. Ren, Y. Gan, M. Lee, C. Yang, F. He, Y. Jiang, G. Dong, R. D. Green and X. Xue, *Journal of The Electrochemical Society*, **163**, F1115 (2016).

90. Y. Xie and X. Xue, *Solid State Ionics*, **224**, 64 (2012).

91. Y. Xie, H. Ding and X. Xue, *Journal of power sources*, **241**, 718 (2013).

92. A. Zekri, K. Herbrig, M. Knipper, J. Parisi and T. Plaggenborg, *Fuel Cells*, **17**, 359 (2017).

93. J. Ma, C. Jiang, P. A. Connor, M. Cassidy and J. T. Irvine, *Journal of Materials Chemistry A*, **3**, 19068 (2015).

94. S. Tao and J. T. Irvine, *Nature materials*, **2**, 320 (2003).

95. Y.-H. Huang, R. I. Dass, Z.-L. Xing and J. B. Goodenough, *Science*, **312**, 254 (2006).

96. S. Sengodan, S. Choi, A. Jun, T. H. Shin, Y.-W. Ju, H. Y. Jeong, J. Shin, J. T. Irvine and G. Kim, *Nature materials*, **14**, 205 (2015).

97. G. Dong, C. Yang, F. He, Y. Jiang, C. Ren, Y. Gan, M. Lee and X. Xue, *RSC advances*, **7**, 22649 (2017).

98. A. Atkinson, S. Barnett, R. J. Gorte, J. T. S. Irvine, A. J. McEvoy, M. Mogensen, S. C. Singhal and J. Vohs, *Nature Materials*, **3**, 17 (2004).

99. Z. Zhan, D. M. Bierschenk, J. S. Cronin and S. A. Barnett, *Energy & Environmental Science*, **4**, 3951 (2011).

100. L.-S. Kang, J. L. Park, S. Lee, Y.-H. Jin, H.-S. Hong, C.-G. Lee and B. S. Kim, *Journal of nanoscience and nanotechnology*, **14**, 8974 (2014).

101. E. C. Miller, Q. Sherman, Z. Gao, P. W. Voorhees and S. A. Barnett, *ECS Transactions*, **68**, 1245 (2015).

102. T.S. Oh, E. K. Rahani, D. Neagu, J. T. Irvine, V. B. Shenoy, R. J. Gorte and J. M. Vohs, *The journal of physical chemistry letters*, **6**, 5106 (2015).

103. G. Tsekouras, D. Neagu and J. T. Irvine, *Energy & Environmental Science*, **6**, 256 (2013).

104. D. M. Bastidas, S. Tao and J. T. Irvine, *Journal of Materials Chemistry*, **16**, 1603 (2006).

105. Y.H. Huang, G. Liang, M. Croft, M. Lehtimaki, M. Karppinen and J. B. Goodenough, *Chemistry of Materials*, **21**, 2319 (2009).

106. D. Ding, X. Li, S. Y. Lai, K. Gerdes and M. Liu, *Energy & Environmental Science*, **7**, 552 (2014).

107.H. Ding, J. Ge and X. Xue, *Electrochemical and Solid-State Letters*, **15**, B86 (2012).

108.C. Ren, Y. Gan, C. Yang, M. Lee, G. Dong and X. Xue, *Journal of The Electrochemical Society*, **164**, F722 (2017).

109.J. Shi and X. Xue, *Journal of Applied Electrochemistry*, **44**, 683 (2014).

110.F. He, X. Jin, T. Tian, H. Ding, R. D. Green and X. Xue, *Journal of the Electrochemical Society*, **162**, F951 (2015).

111.B. J. P. Buhre, L. K. Elliott, C. D. Sheng, R. P. Gupta and T. F. Wall, *Prog. Energy Combust. Sci.*, **31**, 283 (2005).

112.F. Sher, M. A. Pans, C. G. Sun, C. Snape and H. Liu, *Fuel*, **215**, 778 (2018).

113.B. D. Bhide and S. A. Stern, *J. Membr. Sci.*, **62**, 37 (1991).

114.G. Scheffknecht, L. Al-Makhadmeh, U. Schnell and J. Maier, *International Journal of Greenhouse Gas Control*, **5**, S16 (2011).

115.F. Wu, M. D. Argyle, P. A. Dellenback and M. Fan, *Prog. Energy Combust. Sci.*, **67**, 188 (2018).

116.J. Sunarso, S. Baumann, J. M. Serra, W. A. Meulenberg, S. Liu, Y. S. Lin and J. C. Diniz da Costa, *J. Membr. Sci.*, **320**, 13 (2008).

117.P. Bernardo, E. Drioli and G. Golemme, *Industrial & Engineering Chemistry Research*, **48**, 4638 (2009).

118.B. Zydorczak, Z. Wu and K. Li, *Chemical Engineering Science*, **64**, 4383 (2009).

119.K. Li, X. Tan and Y. Liu, *J. Membr. Sci.*, **272**, 1 (2006).

120.Z. Wang, N. Yang, B. Meng, X. Tan and K. Li, *Industrial & Engineering Chemistry Research*, **48**, 510 (2009).

121.X. Tan, N. Liu, B. Meng and S. Liu, *J. Membr. Sci.*, **378**, 308 (2011).

122.A. Leo, S. Smart, S. Liu and J. C. Diniz da Costa, *J. Membr. Sci.*, **368**, 64 (2011).

123.W. Yin, B. Meng, X. Meng and X. Tan, *Journal of Alloys and Compounds*, **476**, 566 (2009).

124.C. Ren, Y. Gan, C. Yang, M. Lee and X. Xue, *International Journal of Applied Ceramic Technology*, **16**, 791 (2019).

125.Y. Gan, C. Ren, M. Lee, C. Yang and X. Xue, *Journal of Solid State Electrochemistry*, **22**, 2929 (2018).

126.X. Tan, S. Liu and K. Li, *J. Membr. Sci.*, **188**, 87 (2001).

127.C.-s. Chen, Z.-p. Zhang, G.-s. Jiang, C.-g. Fan, W. Liu and H. J. M. Bouwmeester, *Chemistry of Materials*, **13**, 2797 (2001).

128.H. Wang and S. A. Barnett, *Journal of The Electrochemical Society*, **165**, F564 (2018).

129.M. A. Habib, H. M. Badr, S. F. Ahmed, R. Ben-Mansour, K. Mezghani, S. Imashuku, G. J. la O', Y. Shao-Horn, N. D. Mancini, A. Mitsos, P. Kirchen and A. F. Ghoneim, *International Journal of Energy Research*, **35**, 741 (2011).

130.C. Li, J. Song, S. Zhang, X. Tan, X. Meng, J. Sunarso and S. Liu, *Journal of the American Ceramic Society*, **104**, 2268 (2021).

131.S. M. Hashim, A. R. Mohamed and S. Bhatia, *Advances in Colloid and Interface Science*, **160**, 88 (2010).

132.H. J. M. Bouwmeester, H. Kruidhof and A. J. Burggraaf, *Solid State Ionics*, **72**, 185 (1994).

133.J. Xue, G. Weng, L. Chen, Y. Suo, Y. Wei, A. Feldhoff and H. Wang, *J. Membr. Sci.*, **573**, 588 (2019).

134.Y. Wei, Q. Liao, Z. Li and H. Wang, *Separation and Purification Technology*, **110**, 74 (2013).

135.T. Kida, S. Ninomiya, K. Watanabe, N. Yamazoe and K. Shimanoe, *ACS Applied Materials & Interfaces*, **2**, 2849 (2010).

136.A. Leo, S. Liu, D. d. Costa and Z. Shao, *Science and Technology of Advanced Materials*, **7**, 819 (2006).

137.Z. Wang, H. Liu, X. Tan, Y. Jin and S. Liu, *J. Membr. Sci.*, **345**, 65 (2009).

138.S. Li, J. Cheng, Y. Gan, P. Li, X. Zhang and Y. Wang, *Surface and Coatings Technology*, **276**, 47 (2015).

139.J. Jiang, J. P. Liu, X. T. Huang, Y. Y. Li, R. M. Ding, X. X. Ji, Y. Y. Hu, Q. B. Chi and Z. H. Zhu, *Crystal Growth & Design*, **10**, 70 (2010).

140.C. Yang, Y. Gan, M. Lee, C. Ren and X. Xue, *Journal of The Electrochemical Society*, **165**, F1032 (2018).